TOWARDS A BETTER UNDERSTANDING OF THE GLOBAL ELECTRIC CIRCUIT AND THUNDERSTORM TRENDS UTILIZING SATELLITE AND GROUND-BASED MEASUREMENTS

A Dissertation

by

THOMAS LAVIGNE

BS, Texas A&M University-Corpus Christi, 2015 MS, Texas A&M University-Corpus Christi, 2017

Submitted in Partial Fulfillment of the Requirements for the Degree of

DOCTOR OF PHILOSOPHY

in

COASTAL AND MARINE SYSTEMS SCIENCE

Texas A&M University-Corpus Christi Corpus Christi, Texas

December 2022

© Thomas Lavigne

All Rights Reserved

December 2022

TOWARDS A BETTER UNDERSTANDING OF THE GLOBAL ELECTRIC CIRCUIT AND THUNDERSTORM TRENDS UTILIZING SATELLITE AND GROUND-BASED MEASUREMENTS

A Dissertation

by

THOMAS LAVIGNE

This dissertation meets the standards for scope and quality of Texas A&M University-Corpus Christi and is hereby approved.

Chuntao Liu, PhD Chair Toshiaki Shinoda, PhD Committee Member

Barbara Szczerbinska, PhD Committee Member Feiqin Xie, PhD Committee Member

December 2022

ABSTRACT

The Global Electric Circuit (GEC) of the atmosphere is a naturally occurring phenomenon in which the Earth's atmosphere acts as a leaky capacitor between the Ionosphere and the Earth's surface. Primarily due to the constant presence of thunderstorms and electrified clouds around the globe, the leaky capacitor is continually recharged by the upward storm current produced above thunderstorms and electrified clouds. The balance between the fair-weather return current which drains the circuit, and the input from the upward storm current creates the stable Earth's electrical system known as the GEC. Under the changing climate, it is anticipated the GEC would vary accordingly. To understand the changes of global thunderstorms, a novel approach at observing thunderstorm trends is conducted by combining a 43-year ground station thunder day dataset with shorter-term satellite optical flash data from the Tropical Rainfall Measuring Mission-Lightning Imaging Sensor (TRMM-LIS). A regional relationship between the thunder day occurrence and the lightning flash density as well as thunderstorm population is conducted in each global 5°x°5 grid. In many regions of the globe such as Argentina, China, and the Maritime Continent, a statistically significant agreement (r-value >0.8) is present between the simultaneous 16-year trends of all three explored variables. This indicates that in these regions, the thunder day recordings statistically represent the flash density and number of thunderstorm events. However, in other regions of the globe, the long-term changes of thunder day occurrence and flash density are not well correlated, or even negatively correlated, indicating the regional nature of the relationship between the two variables.

With the understanding that thunderstorm activity is indeed changing over the course of the past several decades, it emphasizes the importance of monitoring the GEC, which is directly tied to the variations of global electrified clouds. Here, a novel method is introduced to determine fair-weather time periods and monitor this global component of the vertical electric field (Ez) at two sites separated by over 6,000 km (Barrow, AK, and Corpus Christi TX). With the use of a Micro-Pulse Lidar (MPL) backscattering coefficient, as well as other meteorological information, a definition of 5-minute averaged -50 V/m to -300 V/m electric fields, with 5minute averaged standard deviations of less than 25 V/m is selected as criteria to define fairweather periods. Using this method, agreement is found between the composited diurnal variation of fair-weather E_z between the two sites on the hourly, monthly, and yearly timescales. Recent studies also suggest that it is possible that the GEC may also have notable influences on the local cloud properties in the polar region. To validate these findings, the variations of the fair-weather E_z measured in Barrow, AK are compared to numerous local cloud, precipitation, and radiation properties during the polar night. Comparisons between the averaged diurnal variations of fair-weather Ez, and cloud thickness, maximum column backscatter, and precipitation particle counts show correlated diurnal variability. During the time periods with a stronger fair weather E_z, clouds bases tend to be higher, clouds are thicker, have a larger column backscatter, and produce more precipitating particles at the surface. Furthermore, a slight diurnal variability in the polar night surface temperature was found to be highly correlated (r=0.87) to the longwave downwelling irradiance, indicating that the characteristics of these persistent layered clouds act as the primary driver of diurnal surface temperature variability during the polar night in Barrow, AK.

The feedback nature of the GEC system illustrates the global connectivity of the system, with the aggregate of localized electrified clouds around the globe driving the magnitude of the fair-weather return current, which in turn may influence the properties of localized clouds, such as the persistent layered clouds during the polar night in Barrow, AK.

ACKNOWLEDGEMENTS

I would first and foremost like to thank my graduate advisor and mentor Dr. Chuntao Liu. Without his guidance and expertise, I would be nowhere near the researcher or person that I am today. I would also like to thank my committee members, Dr. Toshiaki Shinoda, Dr. Barbara Szczerbinska, and Dr. Feiqin Xie, as well as my Graduate Faculty Representative Dr. Charles Etheridge, for their valuable input and guidance throughout my graduate studies.

None of this would have been possible without the support of my wonderful family. I would like to give a special shout out to my wife Amy, son Levi, parents Don and Eva, brothers Don and Joe, and my grandparents Dudley and Virginia Thompson. They have provided love, support, motivation, and so much more, for which I am very grateful.

I would also like to thank my current lab mates: Florian Morvais, Raven Vasquez, Hailey Santa Anna, Maddie Lilljedahl, Trent McShane, Quincy Walker, as well as my past lab mates and colleagues: Joseph Hill, Lindsey Hayden, Nana Liu, Abishek Adhikari, Sreekanth T.S., John Gonzales, Vinay Kumar, Xiang Ni, Richard Balogun, Farha Pulukool, Suxing Zhu, Leah Swinney, among many others. I have learned so much over the years from our daily conversations.

Thanks to Walter, Jimmy, Josh, Ross, and others for the maintenance of the instrumentation in Barrow Alaska. This work was funded by the National Science Foundation NSF-1519006 and NSF-2219639 grants.

TABLE OF CONTENTS

Page
ABSTRACT iv
ACKNOWLEDGEMENTS vi
TABLE Of CONTENTSvii
LIST OF FIGURES xi
LIST OF TABLES xviii
CHAPTER I: INTRODUCTION
CHAPTER II: HOW DOES THE TREND IN THUNDER-DAYS RELATE TO THE
VARIATION OF LIGHTNING FLASH DENSITY? 5
2.1 Introduction
2.2 Data and Methodology
2.2.1 Global Surface Summary of the Day (GSOD)
2.2.2 Tropical Rainfall Measuring Mission (TRMM) Precipitation Features (PFs) 13
2.2.3 Correlation Between the Ground Stations and the TRMM Lightning Parameters 15
2.3 Results
2.3.1 Long-Term Inter-Annual Variability of Global Thunder-Day Occurrence
2.3.2 Long-Term Seasonal Variability of Global Thunder-Day Occurrence
2.3.3 Comparison of Ground-Station Thunder-Days to TRMM-LIS Flash Density 24
2.3.4 Comparison of Thunder-Day and TRMM-LIS Flash Trends
2.4 Discussion
2.4.1 Annual and Seasonal Trends in Thunder-day Occurrence Around the Globe 28
2.4.2 Trends Observed by the TRMM-LIS Instrument

2.4.3 Comparison of Ground Station Trends to TRMM-LIS Trends	31
2.5 Summary	33
CHAPTER III: OBSERVATIONS FROM THE ONE YEAR ELECTRIC FIELD STUDY-	
NORTH SLOPE OF ALASKA (OYES-NSA) FIELD CAMPAIGN, AND THEIR	
IMPLICATIONS FOR OBSERVING THE DISTRIBUTION OF GLOBAL ELECTRIFIED	
CLOUD ACTIVITY	48
3.1 Introduction	48
3.2 Data and Instrumentation	54
3.2.1 Study Location	54
3.2.2 Instrumentation	55
3.2.3 Calibration	56
3.2.4 Supplementary Data	57
3.3 Results	58
3.3.1 Examples of Influences on the Electric Field by Various Factors	58
3.3.2 Significantly Charged Precipitation Event	58
3.3.3 Aerosol/Lidar Dominant Event	59
3.3.4 Blowing Snow Event	60
3.3.5 Aerosol Influence Event	61
3.3.6 Wind Influence of the Vertical Electric Field	63
3.3.7 Determination of Fair-Weather	65
3.3.8 Case Study Composite of Absolute Value and Standard Deviation Determination	n
of Fair Weather	66

3.3.9 Variability of Fair-Weather at Several Timescales at Multiple Sites: Diurnal	
Variability	67
3.3.10 Minute-to-Hour Fair-Weather Variability	69
3.3.11 Joint Diurnal Seasonal Variability	70
3.4 Discussion/Summary	70
3.4.1 Importance of Supplementary Data	70
3.4.2 Fair-Weather Analysis	71
3.4.3 Implications for Global Electrified Cloud Monitoring	72
CHAPTER IV: RELATIONSHIPS AMONG DIURNAL VARIATIONS OF POLAR NIGHT	
CLOUD, PRECIPITATION, SURFACE TEMPERATURES, AND THE FAIR-WEATHER	
RETURN CURRENT OF THE GLOBAL ELECTRIC CIRCUIT (GEC)	86
4.1 Introduction	86
4.1.1 The Global Electric Circuit (GEC) of the Atmosphere	86
4.1.2 Possible Impacts of the GEC Fair-Weather Return Current	87
4.1.3 Multi-Year Electric Field Study-North Slope of Alaska (MYES-NSA) Field	
Campaign	89
4.2 Data and Methodology	90
4.2.1 Ka-Zenith Radar	90
4.2.2 Micro Pulse Lidar (MPL)	90
4.2.3 Cloud Ceilometer	90
4.2.4 Laser Precipitation Monitor (LPM)	91
4.2.5 Sky Radiometers on Stand for Downwelling Radiation (SKYRAD)	91
4.2.6 Campbell Scientific Electric Field Meter	91

4.2.7 Polar Night Time Period, Diurnal Averaging and Binning	92
4.3 Results	93
4.3.1 Cloud Base Height, Cloud Top Height, and Cloud Thickness Verses the Fair-	
Weather Vertical Electric Field at the NSA Site	93
4.3.2 Cloud Precipitation and Optical Properties Verses Vertical Fair-Weather Electric	
Field at the NSA Site	96
4.3.3 Relationship Between the Longwave Downwelling, Fair Weather Ez and Cloud	
Base Height	97
4.4 Summary and Discussion	99
CHAPTER V: SUMMARY AND FUTURE WORK	12
REFERENCES	16

LIST OF FIGURES

P	a	ø	ϵ
	u	∽	•

Figure 2.1. Difference in thunder-day occurrence at ground stations between 1975-1994 and
1998-2017. Data is excluded after 2013 in China due to the lack of thunder-day records.
Thunder-day occurrence is calculated using the summation of all the thunder-days divided
by the summation of all the total observation days is each region, and is represented as a
percent38
Figure 2.2. Nine selected convectively active regions. Each star represents a ground station39
Figure 2.3. Trends in yearly thunder-day occurrence in the nine selected global regions. Thunder-
day occurrence is calculated using the summation of all the thunder-days divided by the
summation of all the total observation days per year in each region and presented as
percentage
Figure 2.4. Seasonal trends in global thunder-day occurrence observed by the ground stations.
Thunder-day occurrence is calculated using the summation of all the thunder-days divided
by the summation of all the total observation days is each region and presented as
percentage. Five-year averages were selected to reduce the impact of interannual variability
such as a strong MCS event
Figure 2.5. Seasonal trends in thunder-day occurrence in the nine-selected regions
Figure 2.6. a) mean TRMM LIS flash density in 1998-2013 presented as flashes/km2/year over
50x50 grids. b) Mean thunder-day reports per year from ground stations during the TRMM
era, c) The mean population of lightning PFs (#/km2/year), and d) The average flash rate
per lightning PF (flash/min/pf). All variables are averaged in 5x5 degree bins43

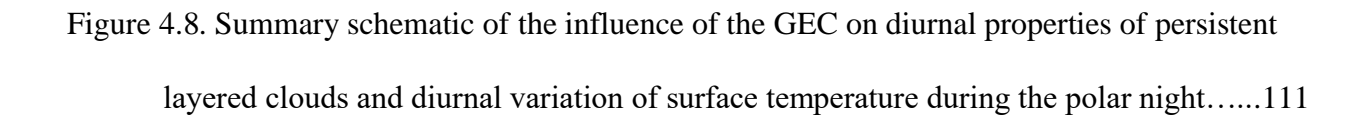
Figure 2.7. a) The trend in lightning flash density (flash/km2) as observed by the TRMM
satellite. b) The interpolated ground station thunder-day trend between 1998-2013, c) The
trend in number of LPFs observed by the TRMM satellite. d) The correlation between
panel a and b for each 50x50 bin. e) The correlation between panels b and c for each 50x50
bin44
Figure 2.8. Time series of the number of annual thunder-days (solid), lightning flash density
(dashed), number of lightning PFs (dotted), and number of flashes/minute/LPF (blue),
observed in the TRMM domain (1998-2013) for four regions showing good agreement
between thunder-days and lightning flash density. Flash density, thunder-days and LPF are
expressed as a percent deviation from their 16-year mean (%) The number in parentheses
indicates the number of ground stations in the region
Figure 2.9. Time series of the number of annual thunder-days (solid), lightning flash density
(dashed), number of lightning PFs (dotted), and number of flashes/minute/LPF (blue),
observed in the TRMM domain (1998-2013) for four regions showing poor agreement
between thunder-days and lightning flash density. Flash density, thunder-days and LPF are
expressed as a percent deviation from their 16-year mean (%). The number in parentheses
indicates the number of ground stations in the region46
Figure 2.10. Time series of thunder-days (solid), lightning flash density (dashed), and number of
lightning PFs (dotted) for three regions. The tan region shows the time period of the TRMM
satellite era. No thunder-day data are available for the China region after 2013 represented
in light red47

Figure 3.1. a) the instrumentation setup in Barrow, Alaska, including two CS-110 electric field
meters, and one RM-Young Alpine anemometer. b) The geographical locations of the two
electric field measurement sites. The distance 6,015 km apart
Figure 3.2. a) Schematic diagram of the vertical electric field calibration process, accounting for
the influence of the metal setup and elevation. b) the simultaneous uncalibrated scatter
between the CS1105m and CS1102m against the ground truth electric field instrument. c)
displays the site corrected scatter of the 2 CS110's versus the simultaneous ground truth.
The dashed line shows the perfect one-one correlation. The calibration factor for the CS110-
2 is a slope of 0.823 and intercept of 54.9, while the factor for the CS110-3 is a slope of
3.121 and an intercept of 16.69. Calibration took place over the course of approximately a
10-day period from June 13th, 2017 until June 23rd, 2017.
Figure 3.3. A case of an intense storm electric field event in Barrow, Alaska on July 3, 2017.
Panel a) displays the vertically pointing Ka-band radar reflectivity, b) the calibrated vertical
electric field measurement at ground surface at a sampling rate of 1 Hz, c) the vertically
pointing Micro pulse Lidar backscattering signature (km-1sr-1), and d) the wind speed (m/s)
for the day measured at 1 Hz76
Figure 3.4. Same as figure 3, except for a Lidar dominated electric field signature case study
recorded on August 12, 201777
Figure 3.5. Case study of an electric field event versus wind in Barrow, Alaska on November 9,
2018. Panel a) displays the vertically pointing Ka-band radar reflectivity, b) the vertical
electric field measurement at a sampling rate of 1 Hz (red = bottom CS110 and blue = top
CS110), c) the U-vector wind speed (m/s), and d) the total wind speed (m/s) for the day
measured at 1 Hz

Figure 3.6. Same as figure 3, except for a fair-weather period case study recorded on July 1,
2017
Figure 3.7. Histogram of the a) difference between the top and bottom CS110 electric field
meters versus the wind speed during January blowing snow days (color filled), and January
non-blowing snow days with haze (contour). B) Difference between the top and bottom
CS110 electric field meters versus the wind speed during January blowing snow days (color
filled), and January non-blowing snow days without haze (contour). C) Difference between
the top and bottom CS110 electric field meters versus the wind speed during August all
sampled data. Blowing snow and haze days were determined using the National Oceanic
and Atmospheric Administration (NOAA) Global Surface Summary of the Day (GSSOD)
dataset80
Figure 3.8. Example scatterplots of 5-minute mean electric-field (V/m) versus the simultaneous
5-minute maximum backscattering (km-1sr-1) overserved by the Micro pulse Lidar (panel
a), and the standard deviation of the 5-minute averaged electric-field (V/m) versus the
simultaneous 5-minute maximum backscattering (km-1sr-1) observed by the Micro pulse
Lidar (panel b)81
Figure 3.9. a) Scatter of 5-minute averaged vertical electric field (V/m) measurements versus the
5-minute averaged standard deviation of the electric field (V/m). Green colors represent
time periods with a Lidar reflectance of less than 150 km-1sr-1 and red colored stars
indicate time periods with a larger Lidar reflectance than 150 km-1sr-1. B) Same as panel a,
but zoomed into the fair-weather region. Fair weather time periods were selected to have at
least 30 consecutive minutes of less than 25 V/m standard deviation of the vertical electric

field. These data were taken in April 9th, April 10th, May 3rd, May 10th, May 30th, August
22nd, September 9th, October 14th, October 15th, and December 18th, all in 201882
Figure 3.10. a) Simultaneous diurnal variations of the mathematically selected fair-weather
values at Corpus Christi (blue) and Barrow (red) for the months of May (solid) and October
(dashed). Panel b) shows the absolute value of the yearly averaged diurnal variation using
the mathematically selected fair-weather values at Corpus Christi (blue) and Barrow (red)
for 2018.:83
Figure 3.11. Comparison of simultaneous mathematically selected fair-weather from Corpus
Christi (dashed) and Barrow (solid). All panels use a 5-minute averaged electric field. All
data from Barrow is displayed using the top instrument (CS110-2)84
Figure 3.12. Joint diurnal and seasonal histograms of the mathematically selected fair-weather
electric field in a) Barrow and b) Vostok Station Antarctica. All data is collected at a
sampling rate of 1 Hz and binned into 1-hourly and 1-monthly bins85
Figure 4.1. Diurnal variations of the a) polar-night and b) yearly averaged fair weather electric
field (red), cloud-base height (solid), cloud top height (dashed), and cloud thickness (dotted
measured with the Micro-Pulse Lidar (MPL) in Barrow AK during the years of 2017-2022.
Figure 4.2. a) Two-Dimensional histogram of polar night cloud occurrence (%) in Barrow,
Alaska measured by the Ka-Band Zenith Radar (KAZR). A threshold of -30 dBZ was used
to determine the presence/absence of a cloud. B) Two-Dimensional histogram of polar night
cloud counts in Barrow, Alaska measured by the ceilometer. The dashed black line is the
mean cloud base height during the same time-period binned to 1-hour averages

Figure 4.3. Two-Dimensional histogram of polar night aerosol occurrence (%) in Barrow, Alaska
measured by the Micro Pulse Lidar (MPL). A threshold of 100 km-1*sr-1 was used to
determine the presence/absence of an aerosol event
Figure 4.4. a) Diurnal variation of the polar-night averaged fair weather electric field (solid), and
polar night cloud precipitation particle counts (dashed) measured with the impact
distrometer. b) Diurnal variability of the polar-night averaged fair weather electric field
(solid), and polar night cloud sum of vertical column backscatter (dashed) measured with
the micro-pulse Lidar. c) Diurnal variability of the polar-night averaged fair weather electric
field (solid), and polar night cloud precipitation intensity (dashed) measured with the impact
distrometer. All values are normalized as a percent deviation from the mean value during
polar night in Barrow AK for the years of 2017-2021
Figure 4.5. a) Scatter plot of hourly average of the polar night fair weather electric field (V/m),
verses downwelling longwave irradiance (W/m2). b) Scatter plot of hourly average of the
Cloud Base Height (km), verses downwelling longwave irradiance (W/m2). Measurements
were made in Barrow AK during the polar night in 2017-2022
Figure 4.6.: Diurnal variation of the polar night (a) and non-polar night (b) surface air
temperature (solid) and downwelling longwave irradiance (dashed) measured by the
SKYRAD during the years of 2017-2022
Figure 4.7. Correlation matrix of the diurnal variability of 9-explored polar night properties:
cloud thickness (c. thickness), downwelling longwave irradiance (DLWI), fair-weather Ez,
cloud base height (CBH), sum of vertical backscatter (sum backscatter), number of
precipitation particles (particles (#), precipitation intensity, temperature, and visibility110



LIST OF TABLES

Page
Table 2.1. 1975-2017 annual and seasonal mean, and annual and seasonal trends in thunder-days
over nine selected regions
Table 2.2. Correlation of regional lightning variables (r-values): Thunder-day (TD), Flash
Density (FD), Flash Rate (FR), and Lightning Precipitation Features (LPFs) 1998-201337

CHAPTER I: INTRODUCTION

More than 250 years ago, in 1752, Benjamin Franklin deduced that lightning was in fact electrical in nature with his famous kite experiments. Since then, extensive knowledge of the field of atmospheric electricity has been gained, from proposed charging theories [*Takahashi*, 1978], to lightning discharge characteristics [*Bruce & Golde*, 1941; *Uman*, 2001], to the climatology of lightning and thunderstorms around the globe [*Zipser et al.*, 2006; *Albrecht et al.*, 2016], to the Global Electric Circuit (GEC) system [Wilson, 1921, Williams 2009], amongst many other key findings. However, it wasn't until relatively very recently, in 2016, that lightning was included as a World Meteorological Organization (WMO) Essential Climate Variable (ECV) [*Aich et al.*, 2018]. In recent years, the value of atmospheric electricity in monitoring the changing climate has become increasingly clear. The difficulty, however, is the relatively short-term time series of quasi-global lightning data which became possible with the advent of the optical imager from space in the late twentieth century [*Christian et al.*, 1999].

To extend the historical lightning observation record, lightning proxy data sources, such as the thunder day variable, have been identified as an important dataset for examining the changing climate, due to its relative long-term record, as well as near-global land coverage [Aich et al., 2018]. According to the historical works by Brooks [1925], as well as the World Meteorological Organization, a thunder day is defined as a local calendar day on which thunder is heard [World Meteorological Organization, 1953]. Over the past several decades, regional studies have shown significant trends in the occurrence of thunder days, such as decreases in China [Lin-Lin et al., 2010; Zhang et al., 2017], and the Baltic Region [Enno et al., 2014], and increases in thunder day occurrence along the Japanese coastal region [Kitagawa, 1989], Sri Lanka [Sonnadara, 2016]], and Brazil [Pinto et al., 2013]. Results from these regional long-term

thunder day trend studies, show the highly variable nature of thunder days around the globe, with no true global consensus of trend activity in thunder days since the industrial revolution.

This dissertation first aims to utilize the 16-year overlap during 1998-2013 of the Tropical Rainfall Measuring Mission (TRMM) Lightning Imaging Sensor (LIS) flash density data, and the Global Surface Summary of the Day (GSOD) ground station thunder day data to better quantify the physical representation of the thunder day variable. The study aims to answer the question of whether there is any agreement in the ground station thunder day occurrence trends and the actual lightning flash density observed by the LIS during the TRMM era of 1998–2013. This combination of long-term crude thunder day data, and relatively short term but much more detailed lightning climatology from space, can potentially shed light on past trends in thunderstorm activity over the globe from a new perspective.

The Global Electric Circuit (GEC) of the atmosphere is a vast Earth system of electrical currents that are present between the Earth's surface and Ionosphere [Rycroft et al., 2008]. Even during fair weather conditions, in the absence of significant clouds, aerosols, etc., a small current density of approximately 2 pA/m² is always present running from the Ionosphere in the upper atmosphere, down to the Earth's surface [Rycroft et al., 2000]. This downward current has been hypothetically explained by a balancing upward current generated by global electrified clouds [Wilson 1921], also named as the "battery" of the GEC [Williams 2009]. Whipple [1929] was the first to tie the diurnal variation of this electrical potential gradient measured at the surface, to the summation of thunder area around the globe. This diurnal cycle of the fair-weather vertical electric field has come to be known as the "Carnegie Curve", named after the all-wooden ship, that made 20-years of geomagnetic and electrical measurements around the globe in the early 20th century [Harrison, 2013]. Nearly 100-years later, this global thunderstorm and electrified

cloud "battery" theory of maintaining the GEC is still the predominate belief. However, fair weather electric field can be easily influenced by anthropogenic activities, including the changing the local air conductivity by pollutant aerosol, and electric facilities. In 2017, the Multi-Year Electric Field Study-North Slope of Alaska (MYES-NSA) field campaign was established in Barrow, Alaska, providing unique vertical electric field measurements in a relative pristine environment in the high-latitude western hemisphere (71.3°N, 156.6°W). This study utilizes the vertical electric field, measured alongside simultaneous cloud, aerosol, and meteorological properties collected in Barrow to develop a robust mathematical definition of fair-weather vertical electric field measurements, representing the global signal of the GEC. The inclusion of concurrent cloud, aerosol, and blowing snow measurements, allows for the potential to isolate the most stringent periods of clear air in the Arctic. This study then aims to apply this mathematical definition of the fair-weather GEC periods to a station in Corpus Christi, Texas as well, and compare the yearly, monthly, and hourly variability in the GEC at two sites simultaneously which are both calibrated in the same manner.

The GEC fair-weather current, which has been shown to be maintained by the constant presence of thunderstorms and electrified clouds around the globe, also potentially can influence the local clouds that form in its presence through a feed-back mechanism. A recent study conducted by *Harrison and Ambaum* [2013], observed that in both the high latitude regions of the northern and southern hemisphere, a consistent diurnal variability of the cloud base height was present during the polar night time-period at each site in the absence of incoming shortwave solar radiation from the sun. These persistent layered clouds that form in the polar regions, were also shown to have positive space charge density at the cloud top, and negative space charge density at the cloud base, caused by the presence of the potential gradient present in the

atmosphere [Nicoll et al., 2016]. Barrow, Alaska observes 66-days of polar night each year. This study aspires to replicate the diurnal variability of the cloud base height during the polar night observed by Harrison & Ambaum, [2013], measured by a suit of cloud and aerosol instrumentation at the site, and compare the variability to the magnitude of the surface fairweather electric field. With the inclusion of the unprecedented collection of supplementary cloud and radiation monitoring present at the Department of Energy Atmospheric Radiation

Measurement (DOE ARM) site, this study also aims to determine if any other properties of these polar night Arctic persistent layered clouds show consistent diurnal variability to the polar night GEC. This would provide further evidence to the connection between the global thunderstorm and electrified activity and properties of clouds in the Arctic, thousands of kilometers away.

Lastly, the study attempts to quantify the role of the persistent layered clouds on the diurnal surface temperature variability in the polar night Arctic.

CHAPTER II: HOW DOES THE TREND IN THUNDER-DAYS RELATE TO THE VARIATION OF LIGHTNING FLASH DENSITY?

2.1 Introduction

For decades, a longstanding question for scientists has been if any observable trends or shifts in global lightning activity have occurred since the Industrial Revolution and beyond [Changon Jr., 1985]. It has been hypothesized that for every increase in air temperature of 1°C, global lightning activity would increase by approximately 5-6% [Price and Rind, 1994], or 11% [Williams, 2012], which indicates that the warming of the planet should lead to an increase in global lightning.

A team of scientists has recently been established to make lightning data available for use in understanding the changing climate [Aich et al., 2018]. The lightning variable has been shown to have a close relationship with thunderstorm activity, as well as precipitation patterns [Williams, 2005; Price, 2013]. Recently the electrical properties of clouds and precipitation systems, have become increasingly useful for understanding the changes and shifts in global climate, and have been added to the Global Climate Observing System's (GCOS) list of Essential Climate Variables (EOCs). The major shortcoming of the use of past lightning activity to monitor climate is the relatively short time span of measurement, as well as limited global observations. For these reasons, lightning proxy data sources, such as the thunder-day variable have been identified as an important dataset for examining the changing climate, due to its relative long-term record, as well as near-global land coverage [Aich et al., 2018]. One goal of this study is to better understand what the thunder-day variable represents in the context of number of thunderstorms and flash density, and to possibly use this information to quantify the trends in lightning around the globe.

According to the historical works by *Brooks* [1925], as well as the World Meteorological Organization (WMO), a thunder-day is defined as a local calendar day on which thunder is heard [WMO, 1953]. A thunder-day is recorded as such regardless of the actual number of thunderstorms occurring on that day. When a storm begins before midnight and ends after midnight, two thunderstorm days are recorded [WMO, 1953]. This is possible during long-lived nocturnal Mesoscale Convective Systems (MCS), which can span across midnight, into a second day. Various localized studies have been conducted on the frequency of thunder-days, and other severe weather phenomena, using ground-station data on the annual and seasonal time scales. These regional studies have revealed that the tendency of thunder-days in the past century has been highly variable and regionally specific. In Asia, Lin et al., [2010] and Zhang et al. [2017] presented that the occurrence of weather events such as thunderstorms and hail have been decreasing in China in the past 50-years. Zhang et al. [2017] showed that based on over 500 ground stations covering China, there has been a decrease in thunder and hail days by approximately 50% since 1960. This decrease in thunder-day incidence was linked to the simultaneous downturn in intensity of the Asian Summer Monsoon, and has been accompanied by the presence of smaller hail size, which also indicates weakening convection in the region [Ni et al., 2017]. Kitagawa [1989] exhibited that over the past 100 years, the frequency of winter thunder-days has increased along the coastal ground stations of Japan. During the same period of time, the inland-plains ground stations showed a decrease in thunder-day frequency during the summer. In Southern Asia, the Island of Sri Lanka has shown a predominantly increasing longterm trend in thunder-days annually [Sonnadara, 2016]. This study which made use of nine ground-based stations across the country during the years of 1961-2010, showed that five stations had a significant increase in annual thunder-days, while four showed no significant

trends. This rules out the presence of a large-scale thunder-day trend across Sri Lanka, but could emphasize the importance of smaller-scale topography and monsoonal direction.

In Europe, *Enno et al.* [2014], showed a significant decrease in thunder-day occurrence of approximately 24% in the Baltic Region, including the countries of Estonia, Latvia, and Lithuania, at 40 stations between the years of 1950 and 2004. The study linked the decrease in annual thunder-days to an increasing number of northerly circulation type weather events, which are thought to have decreased the likelihood of severe weather in the region. Another study conducted in Northern Eurasia, concluded that days observing convective precipitation have increased in all seasons during the time period of 1966-2000 [*Ye et al.*, 2017]. The study showed that the increasing trends were highly correlated with surface warming and moistening that might have contributed to an increase in Convective Available Potential Energy (CAPE), and a subsequent decrease in stability in the region. Another study in Finland exhibits the ability to compare the annual number of thunder-days, to the cloud-to-ground (CG) lightning flash density [*Toumi & Makela*, 2008]. The estimated flash density using lightning flash counters, exhibit a very similar interannual variability to that of annual thunder-days, indicating the possibility of using the number of thunder-days as a proxy for flash density in some regions.

In the Americas, *Pinto et al.* [2013] revealed an increasing trend in annual thunder-days in Southeast Brazil. Since the 19th Century, the cities of Compinas and Sao Paulo have demonstrated significant increases in number of annual thunder-days (68% and 40% increases respectively). This increase was linked to the industrialization and growing urbanization in these cities in the 20th century [*Pinto et al.* 2013]. *Changnon and Changnon* [2001a] reported on the 100-year trends in lightning activity in the United States. Their results showed that the region is highly variable in annual thunder-day occurrence from 86 stations, with 31 stations showing no

trend, 26 showing decreasing trends, and 31 stations observing increasing trends. However, it is still not clear how to interpret these thunder-day changes in the perspective of the variation of thunderstorm and lightning activity. This study did not emphasize the occurrence of the "Big Hiatus" during 1940-1975, in which the trend in global temperatures flattened out substantially, with the associated thunder-day trends decreasing in occurrence. This time period could influence the trend analysis, and partially explain the lack of substantial trends in the United States during this study.

Results from these regional ground station studies of long-term thunder-day trends, show that unique regional mechanisms can influence the trends in localized thunder-day frequency. Each individual region has its specific convectively active time period, which contributes to the global summation of lightning activity. Understanding how these time periods are changing globally, can allow us to study the changes in global lightning at different time scales. Long-term global shifts in thunderstorm activity could subsequently shift the diurnal and seasonal distribution of global lightning. It is important to monitor these shifts in thunder-days and flash density at the global scale, in order to observe the impacts on Earth's electrical processes [Williams, 2009]. These processes such as the Global Electric Circuit (GEC) of the atmosphere are driven by electrified cloud parameters at the diurnal and seasonal timescales [Williams and Heckman, 1993; Williams, 1994, Adlerman and Williams, 1996; Liu et al., 2010; Blakeslee et al., 2014; Lavigne et al., 2017]. Changnon, [1985] attempted to observe global shifts in thunder-day frequencies using 227 ground-based stations. This study builds upon the regional and global works that have been conducted in the past, and gives a more comprehensive look at the changes observed in global lightning, that could possibly help to understand the global variability of the Earth's electrical systems in the past and into the future. One important global study was

conducted utilizing lightning flash counters to approximate the lightning flash rate across a significant portion of the globe [Mackerras et al., 1998]. The study shows how total lightning flash density varies across different latitudes, seasonally and diurnally, and serves as an important baseline for the global lightning flash density climatology prior to satellite technology.

The Tropical Rainfall Measuring Mission-Lightning Imaging Sensor (TRMM-LIS) has been used in the past in numerous studies to help understand the spatial and temporal distribution of lightning and thunderstorms [Christian et al., 1999; Toricinta et al. 2001; Cecil et al., 2005; Zipser et al., 2006; Liu et al. 2012; Albrecht et al., 2016]. Studies such as these have been very successful at determining the most convectively active regions of the world and with the most lightning activity. The TRMM-LIS has also been used to show the diurnal variability of lightning [Cecil et al., 2005]. This study showed that over most land regions, the peak in diurnal activity occurred in the late-afternoon (approximately 1600 Local Time), whereas over the ocean, a much smaller diurnal amplitude was observed, with the peak in the early morning (approximately 0300 Local Time) [Williams et al., 2000]. The TRMM-LIS has also been used to monitor the regional effects of El Niño-Southern Oscillation (ENSO) on lightning activity [Hamid et al., 2001; Yoshida et al., 2007; Chronis et al., 2008; Satori et al., 2009; Williams, 2012]. These findings show that natural climate variability can be observed by the TRMM satellite.

This study compares ground-based station thunder-day data, to the flash density and population of thunderstorm records from the TRMM satellite. The comparison of the global trends observed in the thunder-day occurrence, to the trends observed in lightning flash density (flashes/km²*year), and population of thunderstorms, give us a more complete understanding of the trends and tendencies in global lightning activity. It also provides an opportunity to observe

the capabilities of the TRMM-LIS in observing regional trends in lightning activity compared to ground-based station observations.

Although the 16-year time-series (1998-2013) is not long enough to establish robust climatological trends, it is still worthwhile to investigate whether the trends in thunder-day occurrence and trends in TRMM-LIS flash density are consistent during the 16-year period. The motivation of this study is to answer the following questions:

- Are any regional trends observed in the long-term thunder-day occurrence from the ground stations?
- What are the long-term annual and seasonal trends in thunder-day occurrence in some of the most convectively active regions of the globe?
- Is there any agreement in the ground station thunder-day occurrence trends and the lightning flash density observed by the TRMM satellite during the TRMM timespan of 1998-2013?
- Is there any way that we can explain the similarities and differences in these trend values over different regions by examining the properties of thunderstorms?

To answer these questions, this study builds upon past regional thunder-day studies, with a more robust quantity of global stations, as well as the use of the 16-year TRMM-LIS observations. Section 2 introduces the datasets and methodology that were used. Section 3.1 looks into the long-term annual trends in thunder-days observed by the ground-stations, followed by section 3.2 which looks at the thunder-day trends seasonally. Section 3.3 examines the spatial correlation of the ground station thunder-days and the satellite flash density as well as population of thunderstorms, while section 3.4 compares and contrasts the trends observed by the three variables. Section 4 discusses the results, and section 5 summarizes the important findings.

2.2 Data and Methodology

2.2.1 Global Surface Summary of the Day (GSOD)

The Global Surface Summary of the Day (GSOD) is a dataset of over 9,000 groundbased meteorological stations located worldwide (https://data.nodc.noaa.gov/). This dataset is organized and quality controlled by the National Oceanic and Atmospheric Administration (NOAA). The daily ground station data includes meteorological measures such as: mean temperature, minimum temperature, maximum temperature, dew point, station pressure, wind speed, visibility, precipitation amount, among many others. The dataset also has occurrence flags for each day indicating the binary occurrence of fog, rain, snow/sleet, hail, thunder and tornadoes. For the purpose of this study, only the binary occurrence of thunder-days is used. The term thunder-day refers to the ground station hearing at least one auditory thunder clap in the observed day. This is a binary variable, with either a presence or no-presence of thunder detected for each day. Fleagle, [1949], concluded that the range of auditory thunder could rarely be heard beyond 24 km, while *Brooks*, [1925] stated the range to be only 10-12 miles (approximately 16-19 km) under favorable conditions. Some factors that can influence the distance thunder can travel are thought to be temperature, density, eddies, gradients, humidity, topographical relief, and soil and vegetation type [Brooks, 1925; Changnon, 2001b]. No information is available for the time of detection, or the total number of thunder claps that were heard in each given day. According to NOAA, the station data collected after 1973 is much more reliable. For this study, only data occurring in 1975 and onward are used to ensure that only the most robust station data are incorporated for analysis. The raw data underwent rigorous automated quality assurance by NOAA, to interpret as much of the synoptic data as possible, and to eliminate errors found in the raw data. Then, this data were quality controlled further in the creation of the summary of the

day (https://www1.ncdc.noaa.gov/pub/data/gsod/readme.txt). A very small percentage of error may remain in the processed GSOD dataset. After data processing, a total of 8,396 global stations are used for the analysis. It is known that certain influences such as; altered localized noise, slight movement of stations, urban influences, among others impact the quality of detection of audible thunder [Fleagle 1949; Changnon, 2001b]. These factors become less noticeable with the use of many stations. Studies in the past have discussed the influence of population density on the trends in severe weather such as tornados [Schaefer and Galway, 1982; Grazulis and Abbey 1983; Brooks et al., 2003; Anderson et al., 2007]. These studies concluded that human errors are the primary cause of spatial and temporal variability of tornado reports. While population density trends could possibly have a minimal influence on the auditory observations of thunder, only stations that were operational in 1975 and onward were used in the analysis, so there are no artificial trends in the number of stations present in each region. Tornado reports incorporate civilian accounts of tornado occurrence, which can strongly be biased by the increasing population around the world. However, thunder-days are only reported by meteorological stations, which do not change in number throughout the four decades of analysis.

It is also important to note that the ground stations located in the country of China stopped recording the presence of thunder-days after 2013. All thunder-day calculations conducted in the region end in 2013 instead of 2017. In recent years, there have been transitions from human-observing weather stations to un-manned automatic weather stations, where thunder-days are no longer reported. This transition is not unique to China, and has been a cost-saving measure for an increasing number of regions of the world. A steep increase in the complexity and scope of automated weather sensors has been established in the last several

decades [*Merenti-Välimäki*, 2001]. This is noteworthy for thunder-day observations, for which human observers are essential.

To ensure further that no artificial trends are observed in the dataset, the occurrence of thunder-days (%) is calculated for each station. Not every station observed the same number of days each year due to missing data, leap years, etc. To account for these discrepancies, the percent occurrence (%) is incorporated by using the summation of thunder-days, divided by the summation of the total sampled days multiplied by 100 for each desired station or region in a particular year. The total sampled days were taken to be the total number of days for which any meteorological data were recorded for each station. The trends of the regional occurrence are then compared for the 43-year time period. Nine regions are selected for further thunder-day occurrence analysis. These regions have been identified in previous literature as being convectively and electrically active regions of the world [Zipser et al., 2006; Liu and Zipser, 2015; Albrecht et al., 2016]. The regions selected for thunder-day analysis were: South Central United States (SCUS), the Amazon, Argentina (Argen), Sahel, Congo, Maritime Continent, India/Himalayas (India/Hima), and Australia (Aust) (black boxes in Figure 2). These nine regions are selected due to all showing some organized activity of thunder-day trends, as well as being convectively active regions. The United States is selected due to the robust past literature on the electrical nature of the region. The regions are averaged over a relatively large area, so the annual average number of thunder-days reflect the nature of the larger region as a whole, instead of the smaller scale areas that can produce a very large occurrence of annual thunder-days. The selection of larger regions can reduce the number of expected annual thunder-days in some regions such as India or Australia.

2.2.2 Tropical Rainfall Measuring Mission (TRMM) Precipitation Features (PFs)

This study uses 16-years of data from the TRMM satellite (1998-2013.) This satellite measures precipitation using a passive TRMM Microwave Imager (TMI), and the Ku-band Precipitation Radar (PR) in the latitude interval of approximately 36°N-36°S. For this study, Precipitation Features (PFs) have been grouped together using the observations from the PR instrument. A PF is defined as contiguous raining pixels of greater than 75 km² observed by the TRMM PR that are grouped together to create a raining feature [Seto et al., 2013; Liu and Liu 2016; Adhikari et al., 2018]. The threshold of 75 km² was chosen because the contribution of total rainfall by PFs less than 75 km², based on the TRMM 2A25 algorithm, is less than 5% [Liu et al., 2010]. Furthermore, the contribution to rainfall from PFs with an area of less than 75 km² and an echo top of greater than 4.5 km is less than 0.6%. Therefore, for ease of data processing, only larger PFs are included for the analysis.

For each PF observed during the 16-year period, the TRMM-LIS lightning flash count information is included with the feature. The TRMM-LIS is an optical lightning detection instrument mounted on the TRMM satellite [*Christian et al.*, 1999]. The satellite orbits at an altitude of approximately 360 km above the Earth's surface and 403 km after the orbit boost in August 2001. The field of view of the LIS is approximately 668 km at nadir, with a 4.3 km spatial resolution [*Albrecht et al.*, 2011]. After the boost of the satellite in August of 2001, the average view time of each pixel at nadir was approximately 92 seconds [*Albrecht et al.*, 2011]. Based on the flash locations, regional lightning flash density (flashes/km²*year) can be calculated. First, we calculate the summation of lightning flashes observed in the TRMM PF dataset during the 16-year period in each gridded 5°x5° box. Second, the summation of lightning flashes is divided by the area of the total sampled pixels in each 5°x5° box, giving a value of flashes/km². Third, the flashes per km² are then divided by the average view time in seconds by

the satellite of each 5°x5° box, giving a flashes/km²*second. Then we get the final flash density, with units of flashes/km²/year [Cecil et al. 2014], by multiplying by the number of seconds in a year. The number of Lightning Precipitation Features (LPFs) were also calculated by determining the number of PFs with at least one flash of lightning in each 5°x5° box. It is important to note that the TRMM pixel size and view time changed before and after the orbital boost. This was accounted for by calculating the area of each PF using the corresponding pixel size to the time of sampling, as well as the corresponding view time of each PF. Because the TRMM satellite is not in a sun-synchronous orbit, it provides lightning flash observations in full diurnal cycle, but also suffers from diurnal sampling biases. Negri et al. [2002] discussed the TRMM sample biases in the diurnal variation of precipitation, and suggested that three-years of data were needed to fully resolve the diurnal cycle of precipitation in a 12° grid. Though here we do not focus on the diurnal variation of lightning, the annual flash density on a 5°x5° grid could suffer from a slight diurnal sampling biases. The Geostationary Lightning Mapper (GLM) onboard the Geostationary Operational Environmental Satellite-R-East, does not suffer this diurnal sampling bias [Rudlosky et al., 2019]. This satellite, alongside other geostationary satellite missions in the future, will be valuable resources for monitoring lightning activity in real-time with a more precise diurnal variability.

2.2.3 Correlation Between the Ground Stations and the TRMM Lightning Parameters

To determine the significance of the correlation between the calculated variables

(Thunder-days, Flash Density and LPFs), a standard correlation coefficient (r-value) was calculated for each 5°x5° box. This value is always between -1 and 1, with positive values indicating positive linear correlations, and negative values indicating negative or opposite correlation of the trends. The r-values were calculated by creating a scatter of corresponding 16-

yearly averaged thunder-day occurrences, flash density, and number of LPFs in each box for the overlapping years. The r-value was then calculated for the correlation of the scatter between the 16-points of each variable.

2.3 Results

2.3.1 Long-Term Inter-Annual Variability of Global Thunder-Day Occurrence

Utilizing 8,396 global ground-based meteorological stations, a global trend map of thunder-day occurrence was created. The thunder-day occurrence represents the percentage of total sampled days from each station that noted auditory thunder at least once in the monitored day. Figure 1a shows the 43-year (1975-2017) mean occurrence of thunder-days at each station. Regions that exhibit a large occurrence of thunder-day activity include Central Africa, Southeast United States, Southeast Asia, Argentina, the Amazon, Maritime Continent, among others. 20year mean occurrences were calculated for the first 20-year period (1975-1994), and the last 20year data collection period (1998-2017). Twenty-year total occurrences were selected in order to make a more robust analysis, removing some of the interannual noise, such as uneven sampling or abnormal lightning activity. Figure 1b shows the difference for each ground-station subtracting the final 20-year period from the first 20-year period, with warm colors indicating increasing thunder-day occurrence and cool colors indicating decreasing thunder-day occurrence. Clear regional trends can be observed throughout the globe, with regions such as China, India, Australia, the Amazon, and Western Europe showing clear thunder-day tendencies during the study period.

China, which has a relatively robust ground-station coverage (>500 stations), shows a decreasing trend in thunder-day occurrence. This is consistent with the previous literature on trends in thunderstorms and hail in the region [*Zhang et al.*, 2017]. The most intense decrease in

thunder-day activity (5-10%) can be seen in the southern portion of the country. The analysis reveals that the central portion of the region also observes significant decreases, and less of a trend is seen towards the northern and northeast regions of the country. Moving farther north into Russia, slight increasing trends in thunder-day incidence is observed at a majority of the stations (<5%).

The sparse station coverage in the Amazon region displays the most intense and significant (10-15%) increasing trend in thunder-day occurrence in the world. A large increase in thunder-days from the first 20-year period to the second, is observed in the majority of the stations between 0° and -30° latitude. The northern extremity of South-America displays mixed trends, with no clear predominate shift in thunder-day activity. The southern extremity of South America also shows systematic trends.

The United States, majority of Europe, and Africa display no clear consensus of trends on a station-by-station scale. In order to better understand the regional changes in thunder-day occurrence, nine intense convective regions of the globe are selected. Figure 2 shows the nine selected regions, with each star representing a ground-based station within the region. The annual regional occurrence is calculated by taking the summation of all the thunder-days heard inside each regional box, and dividing by the total number of sampled days inside the regional box in each year, and is summarized in Table 1. This value allows for a more robust analysis of the large-scale regional trends, and removes the possible influences from regions with sparse station coverage. Table 1 summarizes the average number of thunder-days observed in each convective region annually as well as seasonally. A summary of the rate of annual and seasonal thunder-day trends in each region during the sampled period is also shown in table 1.

Figure 3 displays the yearly-averaged trends in thunder-day occurrence for each of the

nine selected regions. During the 43-year period, six of the nine convectively intense regions display sigificant increasing trends in thunder-day occurrence. As previously shown in Figure 1b, the Amazon region shows the largest increase, increasing from a 5% occurrence in the 1970s, to 20% thunder-day occurrence in the 2010's. This is an increase of approximately 13.3 thunder-days per decade, and is consistent with a previous study of Southeast Brazil, showing statistically significant increases in annual thunder-days in this fast-developing and changing region of the world [*Pinto et al.*, 2013]. Also in South America, Argentina shows significant increases in thunder-days (2.6 thunder-days/decade). The region exhibits an increase from approximately an 8% occurrence in 1975 to 11% in 2017, based on the slope of the trend line. Both large-scale intense lightning regions of South America (Amazonia and Argentina) are shown to have an increasing trend in thunder-day occurrence.

The Congo region, one of the most intense convective regions of the world, exhibits an average of 123 thunder-days per year in the large-scale region (Table 1). The central portion of the Congo region has very few stations available for analysis, and is under-represented.

However, the western portion of the Central Africa has a sufficient number of stations to build significant trends in the region. Figure 3a shows overall increasing trends in the Congo region from approximately a 28% occurrence in the 1970s, to a 35% occurrence in the last several years, equating to an increase of 6.9 thunder-days/decade. Smaller-scale processes appear to be influencing the thunder-day trends in the continent of Africa as evidenced by Figure 3d, which demonstrates that the Sahel region exhibits opposite trends in thunder-day activity in comparison to the Congo. Decreases in this region are observed from an approximate 24% occurrence to 17%, indicating a possible weakening in convective precipitation occurrence in the region with a decrease of 5.4 thunder-days per decade.

Central America, the India/Himalayan, and the Maritime Continent regions all also exhibit significant increases in thunder-day occurrence. Central America (Figure 3f) displays an increase in occurrence of approximately 11% to 15% over the course of the four decades, equating to an increase of 4.7 thunder-days/decade. Figure 3c shows that the India/Himalayan region increases from 5% to 8%, and the Figure 3i (Maritime Continent) shows the least intensification, shifting from 17% to 18%, equivalent to increases of 3 thunder-days per decade.

Australia (Figure 3g) exhibits a decreasing trend in thunder-days during the study period. The figure shows a shift from approximately a 4% to a 2% occurrence (-1.3 thunder-day per decade) in the region. Figure 3e displays that the South-Central United States (SCUS) observes no clear trends (p-value of 0.29) in thunder-day activity, with the average occurrence in the region remaining at approximately 17%. All eight of the other convective regions show p-values to be much less than 0.01, indicating a statistically significant change in thunder-day frequency in the regions, although some of the trends are relatively weak such as Australia.

In order to understand some of the physical processes that possibly contribute to the trends exhibited in thunder-days and flash density, a comparison is made with the results from the past literature on regional long-term thunder-day trends. This comparison allows the results from Figures 1 and 3 to be supported or refuted.

In China, it is well documented that thunder-day and thunderstorm activity has been decreasing since the 1950s [Zhang et al. 2017], which is corroborated with the results shown here. It has been shown that the reduction of thunder-day events is strongly correlated with the weakening of the East Asian summer monsoon, which is the primary source of moisture and dynamic forcing conducive for warm-season weather over China [Zhang et al., 2017]. A weak correlation was also found between the cloud-to-ground flash density and number of lightning

days in Guang-Dong Province, China [*Chen et al.*, 2004]. This weak correlation provides some evidence that the variation of cloud-to-cloud flashes may be more dominant in the relationship between flash density and thunder-days in the region.

In the United States, Figures 3e and 5f show no significant changes in thunder-day activity in the south-central portion of the country annually or seasonally. This region was analyzed by *Changnon* [1985], stating that the variability of thunder-days was correlated to cyclone frequency. A study conducted in the northern latitude of the country in Fairbanks, Alaska, revealed a 2°C increase in summertime surface temperature from 1950 to 2005, accompanied by a simultaneous upward trend in number of annual thunder-days [*Williams* 1999]. This indicates that thunderstorm activity in northern latitudes of the United States could be significantly influenced by the rise in global temperatures in the past 100 years. No significant large-scale trends are exhibited in Alaska as a whole in Figure 1b, however several individual stations show increases in thunder-day occurrence, especially in the northeast.

The increase in thunder-day occurrence in Brazil in Figure 1b, 3h, and 3b can be tied primarily to the increase in urbanization of the region, and not to global warming. Compelling evidence was shown by *Pinto* [2015], stating that of the 14 cities that were studied, 12 had a large population increase since 1910. All of these 12 Brazilian cities that have since grown much larger, also exhibited significant increases in thunder-day occurrence. The other two cities (Rio de Janeiro and Cuiaba), were already large cities in 1910, and showed no significant growth in development or thunder-days around the ground station sites. This provides evidence that the urban heat island effect, along with increased aerosols could be leading to a significant increase in thunder-days in the large cities of this country [*Pinto*, 2013; *Pinto*, 2015].

The number of annual thunder-days in the Siberian region has been detected to be decreasing by approximately 25% between 1966-1995 [Gorbatenko & Dulzon, 2001]. This similar downward trend in thunder-day occurrence is shown in Figure 1b in the far northeast of Siberia, but is not clear throughout the entirety of northern Russia. The downward trend in thunder-days can be possibly attributed to shifting atmospheric circulation [Gorbatenko & Dulzon, 2001]. A simultaneous downturn in cyclonic activity was observed during the study period, indicating that the suppression of these systems are leading to less thunderstorm activity. No trends in thunder-day occurrence were observed in Germany during the years of 1974-2003 [Kunz et al., 2009]. This is consistent with Figure 1b, which shows no significant trends in thunder-days.

In the Northern Caucasus region, an increasing trend in thunderstorm activity was observed between 1936-2006 [Adziev & Adzhieva, 1999. This increase in annual thunder-days is more pronounced over the high elevation and foothill areas of the region in Figure 1b. In this region, thunderstorm occurrence can be highly spatially variable, with just tens of kilometers of separation, and a factor of 1.2-2 in thunder-day occurrence. Figure 1b also shows the Northern Caucasus increasing from approximately a 4% to 6% annual occurrence of thunder-days. However, the region just south of the Black and Caspian Seas, including Iraq and Iran, showed much larger increases in thunder-days. This is consistent with past studies discussing increasing trends in annual thunder-days in Iran [Araghi et al, 2016; Gavidel et al., 2017]. The region exhibits an increasing trend in thunder-day occurrence between 1961-2010 in almost all months of the year, with April and May being the most significant [Araghi et al, 2016]. This spring enhancement of this semi-arid/arid region is hypothesized as being due to

warming during the spring months, which are already the most humid of the year [Araghi et al, 2016]. This could lead to more suitable conditions for thunderstorm activity.

2.3.2 Long-Term Seasonal Variability of Global Thunder-Day Occurrence

In order to observe a more detailed nature of trends in thunderstorms around the globe, a seasonal observation of thunder-day trends has been conducted for each ground-station. Figure 4 shows the global distribution of thunder-day occurrence trend for each season: December-February (DJF), March-May (MAM), June-August (JJA) and September-November (SON). Figure 4a shows the trend of each station in the DJF season. The most noticeable trends in thunder-day occurrence in this season occurs in the Southern Hemisphere. Most notably, Figure 4a shows increases in the majority of the South American region thunder-day occurrence (25-30%) from 1975-1984 to 2013-2017. Five-year periods were selected in order to minimize the interannual influence, and to obtain a more robust picture of the seasonal changes. The majority of stations in Southern Africa are also shown to have observed an increase in thunder-days during the same time period. In contrast, Australia displays a decreasing trend in thunder-days during their summer DJF season. Very little if any trends are noticed in the Northern Hemisphere during the DJF season. It should be noted that February is considered a severe weather month within the United States severe weather season. Very little if any trend is found in the DJF season in the SCUS.

Figure 4b shows the trend in thunder-days for the MAM season. The most notable trends on the station level in this season occurred in the Amazon, which exhibits an increase of approximately 10-20%, and China which displays a decrease of approximately 10-20% on average, which is consistent with the decreasing trends found in previous literature. (Zhang et al., 2017). Figure 4b also shows that the Maritime continent exhibits an increase in thunder-day

occurrence during MAM. No trends are found in the United States during the significant severe weather season of MAM.

Figure 4c displays the occurrence trends during the study period for the JJA season.

Figure 4c shows that China exhibits a relatively large decrease in occurrence in this season (25-30%). Most of eastern Europe and Russia exhibit slight increases in thunder-days during their summer season. The Maritime Continent and India also display significant increases during this season. It is important to note that during JJA, South America shows very little thunder-day trends, while Africa appears mixed. The central portion of Africa exhibits decreasing trends, while the western portion shows primarily increasing trends. The southern portion of the continent exhibits very little trend in thunder-day activity in JJA.

Figure 4d presents the seasonal trends during the SON season. Most notable increases in this season occur in the Amazon, Maritime Continent and India. Noticeable decreases can be observed in the figure in China and Australia during SON as well.

In order to determine the seasonal ground-station trends for the convectively active regions of the globe, the same nine regions were used for the seasonal analysis. Figure 5 shows this results. Figure 5 shows that each region displays a unique pattern of thunder-day trend activity. Several regions such as the Maritime Continent and the Amazon, also exhibit a relatively large occurrence in the local spring and fall months. Figure 5 strengthens the idea that global and regional trends in thunderstorm activity can be monitored seasonally, with certain regions of the globe showing increases or decreases in thunder-day occurrence. This is important to be able to refine the temporal scales in which the trends occur, in order to determine how the changing climate influences regional thunderstorm activity in more detail.

2.3.3 Comparison of Ground-Station Thunder-Days to TRMM-LIS Flash Density

Figure 6 shows the comparison of the three 16-year (1998-2013) averaged TRMM-LIS variables: flash density (6a), population of LPFs (6c), and flash rate (6d), to the mean annual thunder-days per year calculated during the same 16-year period (6b). The thunder-day, flash density and population of LPFs are largely in agreement in spatial distribution. Figure 6a, showing the flash density binned in 5°x5° boxes, reveals relatively high flash density in Central Africa, South America, southern United States, eastern India, and the western Maritime Continent. This is consistent with past satellite-based observations of lightning density [Christian et al., 2003; Cecil et al., 2014; Albrecht et al., 2016; Rudlosky et al., 2018]. The thunder-day frequency shown in figure 6b displays positive qualitative spatial agreement with the flash density observed by TRMM. The regions of the world with the highest frequency of annual thunder-days are shown to be Central Africa, Amazon, Argentina, Southeast United States, eastern India, southeast Asia, and the Maritime Continent. It appears that certain regions such as the Maritime Continent and the Amazon, have a larger number of annual thunder-days to flash density ratio than most of the world. This provides evidence that these regions see a relatively large number of thunderstorms that produce relatively few lightning strikes per event, with is consistent with the literature [Cecil et al., 2015]. This is supported by figure 6a, which shows that the Amazon, Central Africa and the Maritime Continent produce the largest number of flashes/km²/year over large regions. Overall, the 16-year averaged annual thunder-days shows positive spatial correlation to the TRMM flash density.

2.3.4 Comparison of Thunder-Day and TRMM-LIS Flash Trends

In order to take a more comprehensive approach to observing the global shifts and trends in lightning activity, this study applies the use of multiple independent data sources. It is

important to understand the agreement/disagreement between the trends in thunder-days observed by the ground stations, and the trends in flash density and population of LPFs observed by the TRMM satellite. Recognizing these agreements/disagreements can allow us to better verify the shifting in electrical nature of storms around the globe, as well as learn about some of the properties of the precipitation systems that are occurring. Although 16-years of the LIS data is not a long enough time span to deduce robust climatological trends, it is one of the longest and most trusted set of global satellite lightning flash data that is available to date. Figure 7 compares the two data sources, both averaged in 5°x5° boxes. Figure 7a shows the flash density change in each 5°x5° box. Figure 7b shows the interpolated ground station thunder-day change during 1998-2013. Increasing trends in the mean number of days exhibiting auditory thunder occur in the Amazon, Central America, Western Africa, the Middle East, India and the Maritime Continent. Fewer observed thunder-days are shown in Australia, China, North-Central Africa, and Argentina. Figure 7c displays the trend in annual number of LPFs (#/km²/year) in each 5°x5° box. Similar qualitative spatial patterns are observed in this variable as are seen in the thunderday trends (Figure 7b), with increasing number of thunderstorms annually occurring in Western Africa, the Middle East, Southern India, and the Maritime Continent. Regions with a declining number of annual thunderstorms include; Australia, South Africa, China, and western North America.

Figure 7d investigates the correlation between the trend in flash density and the trend in thunder-day frequency in each 5°x5° box. The results show that the correlation between the two variables vary regionally, however most of the TRMM domain shows a positive correlation (r-value). These regions of positive correlation include China, Australia, the Maritime Continent, the Middle East, South Africa, Argentina, Central America, among others. A few regions show

an opposite trend in thunder-day occurrence and flash density. These include Southeast Asia, North-Central Africa, and Western Africa. This result indicates that although there is a positive agreement over much of the tropics and subtropics, the thunder-day and flash density variables are not always directly correlated. To further investigate the relationship between thunder-days and TRMM-LIS parameters, the trend in thunder-day occurrence (Figure 7b) was compared to the trend in number of annual LPFs (Figure 7c) in each 5°x5° box. Figure 7e shows the correlation coefficient for each bin. The results show an even higher correlation between the trend in thunder-days, and the trend in number of LPFs, with the majority of the TRMM domain, showing a positive relationship between the two variables. Many regions such as South Africa, China, the Maritime Continent, Central America, Argentina, the Middle East, among others, show r-values of greater than 0.6. Having such a positively correlated interannual agreement between these two variables, that are measured using two completely different datasets, provides enhanced evidence that the trends observed are indeed trustworthy.

To understand why the trend in thunder-days and the trend in flash density are so highly correlated in some regions, and not at all correlated in others, four highly correlated, and four uncorrelated regions were chosen for further investigation. The regions are shown as the boxes in Figure 7. It is important to note that these regions are not the same as selected in Figure 2, which focuses on regions with more obvious trends. Figure 8 shows the 16-year time series of the thunder-day occurrence (solid black), flash density (dashed), number of LPFs (dotted) and the flashrate/PF (blue) for the four correlated regions. All of these regions show positive correlation coefficients of at least 0.58, with the Maritime Continent, China, and Argentina all showing correlation coefficients of above 0.8 between the flash density and thunder-day variables. For these four regions, the interannual variability of the thunder-day occurrence, flash density and

number of lightning PFs all show positive linear agreement over the 16-years. Interestingly, the flashrate/PF (flashes/min/PF) variable, also exhibit a positive relationship to the other three variables in all four highly-correlated regions. In these regions, the number of thunderstorms and the number of flashes/thunderstorm are at least slightly positively correlated.

In contrast, Figure 9 shows the four uncorrelated regions between the thunder-days and flash density. In these regions the flash density is more correlated to the flashrate/LPF, with all correlation coefficients of at least 0.66, than the total number of LPFs. This indicates that in these regions, the flash density is strongly driven by the amount of flashes in each thunderstorm. In all four uncorrelated regions in Figure 9, the number of LPFs and the flashrate/LPF are negatively or poorly correlated. For example, in these regions, if the number of annual thunderstorms is increasing, the flashrate/thunderstorm is either decreasing or showing no correlation to the number of thunderstorms, and vice versa. Table 2 displays the correlation coefficients of the regional lightning variables for all eight of the selected regions. In all cases, if the flash rate is uncorrelated to the number of LPFs, the thunder-day to flash density correlation is also poor. However, if the correlation between the flashrate/LPF and number of LPFs is at least slightly positive, the correlation between the thunder-day occurrence and the flash density is significant (r-value > 0.58). This indicates that regions that show a positive correlation between the flashrate and number of LPFs, also show a similar trend in flash density and thunder-day occurrence. This is important because of the relatively longer time series of thunder-day data, extending much further than the satellite era (some stations date back to 1930). Understanding how we can utilize the combination of thunder-day and satellite flashcount data to better reveal the global and regional trends in lightning flash density in the past four decades and beyond, is valuable to better distinguish the past tendencies in thunderstorm activity. Although we do not

have satellite measured lightning flash density prior to the late 1900's, the similarities in interannual variability between thunder-day occurrence and flash density in some specific regions, allows us to possibly estimate the past lightning activity over a longer period of time. Figure 10 shows the 43-year time series of thunder-days occurrence (solid), flash density (dashed), and number of lightning PFs (dotted) for three selected regions (S. Maritime Continent, Middle East and China). The interannual agreement between the three variables during the TRMM era, adds confidence in the longer thunder-day dataset in these regions, to observe the trends in lightning activity over the past four decades. In the Southern Maritime Continent (Figure 10a), and the Middle East (10b), slight but significant (p-value < 0.1) increases in lightning activity can be inferred. In China (10c), a significant decrease in lightning activity was observed since 1975 (p-value <0.01), which is corroborated with the literature (Zhang et al., 2017). With this ability to use the combination of the ground-station thunder-day data, and the new age lightning observations from space to infer regional lightning activity trends over a much longer timespan, gives us a unique opportunity to possibly study the impact of climate change on the electrical nature of storms around the globe.

2.4 Discussion

2.4.1 Annual and Seasonal Trends in Thunder-day Occurrence Around the Globe

The global map of the 8,360 ground-based stations shown in Figure 1a, provides evidence as to how the electrical nature of thunderstorms has changed over the past four decades. Figure 1b indicates that regional forcing is influential in determining the pattern of thunder-day activity, as no true global consensus is observed. However, it is should be noted that six of the nine selected convectively active regions show significant increases in thunder-day occurrence, providing evidence that thunderstorm activity is possibly increasing in the tropics with a

warming climate. This differs from analysis from Finney et al, [2018], stating that a decrease in global lightning may be observed over the course of the next century, using a new ice flux parameterization. These regional shifts, shown in Figure 3, are largely corroborated by the past literature conducted around the world, providing further evidence to the validity of the trends. For example, deep convection in China is possibly being suppressed by the weakening Summer Asian Monsoon, with the anomaly in the summer monsoon index decreasing sharply from 1965 to 2005 (Zhang et al, 2017). This result is verified by the GSOD ground station decrease in thunder-day occurrence. The past four decades of ground station results also verify the past literature observed in Europe. A European divide is displayed in thunder-day trends, with the western portion of Europe, including the Baltic observing primarily decreasing trends in thunderdays. The Eastern portion of Europe, incorporating Eurasia, exhibits predominately increasing trends in thunder-day activity. This is possibly caused by the increasing CAPE and moisture in the east, which enhances thunderstorm activity, and the increase in number of northerly circulation type weather events in the west, which suppresses thunderstorm activity (Enno et al., 2014; Ye et al., 2017). In the Amazon, the long term behavior of GSOD ground stations support previous studies of upward trending lightning activity in the region *Pinto et al.*, [2013].

Understanding how these regions are shifting in thunder-day occurrence seasonally, is important to understand the temporal scales in which the global aggregate of lightning activity is also changing. For example, with the intense increase in thunder-day occurrence in South America, it is reasonable to expect a relatively larger proportion of lightning activity occurring during the convectively active periods, (i.e. DJF and SON, than occurred 43 years ago. Likewise, evidence suggests that the period of convective activity over the continent of Australia (DJF), could see less contribution to global lightning and electrified cloud activity than it did

previously. Monitoring these shifts to the seasonal and interannual variability of total global lightning and electrified cloud parameters such as area of 30 dBZ in the mixed phase temperature region, which has been shown with a high correlation with GEC [Lavigne et al., 2017], could be a useful technique in monitoring the trends in regional lightning activity in a changing climate.

2.4.2 Trends Observed by the TRMM-LIS Instrument

Figure 7a shows the 16-year average trend in lightning flash density for each 5°x5° box. Many tropical and subtropical regions observe at least slight increases in lightning flash density over from 1998-2013, including Southern India, Southeast Asia, the Maritime Continent, the Middle East, Central America, among others. This is consistent with the theory that in a warming climate, increased lightning in the tropics and subtropics should be observed [*Price and Rind*, 1994; Reeve and Toumi, 1999; Williams, 1992; Williams, 1994; Williams, 1999]. However, some regions such as Australia, China, and South Africa appear to have decreasing trends in flash density in the past 16 years. This indicates that other localized effects may play a role in some regions of the world. It is important to note the role of Mesoscale Convective Systems (MCS) on the observed trends in interannual variability of thunderstorm activity in certain regions. Goodman and MacGorman, [1986], described that in the United States, a single intense MCS event can contribute 25% of the total annual lightning flashes. It is possible that only a few of these intense MCS events could bias the interannual variability and lead to significant climatological trends. The thunder-day record of intense MCS events, does not reflect the many thousands of flashes in the given day. However, these large systems are typically reported by numerous ground stations, accounting for some of the bias. ENSO events have also been shown to influence regional lightning patterns [Goodman et al., 2000]. For example, the warm ENSO phase has been associated with an increase in lightning activity over the western Maritime

Continent [Hamid et al., 2001; Chronis et al., 2008]. This also indicates that ENSO related phases can influence the interannual climatology of lightning, and must be accounted for when discussing trends in regional lightning frequency. More work is needed in the future to determine the large-scale versus localized influences to lightning activity trends around the globe. As more flash count data becomes available in the future, a clearer picture of regional lightning trends via satellite can possibly be drawn [Goodman et al., 2013; Blakeslee et al., 2014].

2.4.3 Comparison of Ground Station Trends to TRMM-LIS Trends

Figure 6 shows that the spatial distribution of annual thunder-days and annual flash density are largely consistent with each other over a 16-year period. Several regions such as the Amazon and Maritime Continent exhibit disproportional ratios of thunder-days to flash density relative to other regional observations. These unique regions exhibit a large number of LPFs, with a relatively lower number of flashes per LPF. The flash density is dominated by the large number of LPFs, rather than the intensity of the thunderstorms. However, the majority of the rest of the tropics and subtropics are in agreement on the spatial distribution of annual thunder-days and annual flash density. This allows for the next logical step to discern whether or not the relatively longer-term trends in these variables are also consistent with each other. It is important to note that 16-years of observations is not ideal for understanding long-term trends in lightning activity. It is however, reasonable and advantageous to look at the agreement/disagreement between the thunder-day trends and flash density trends during the same period of time to understand if any new information can be drawn. Figure 7d shows that many regions in the tropics and subtropics are in agreement (positive linear relationship), such as; Australia, the Maritime Continent, Argentina, China, Central America, the Middle East, and South Africa, among others. This provides some evidence that the satellite trends are verified by ground-based

observations of thunder-days, and vice versa. Figure 7e provides more evidence for this, showing that the correlation between thunder-day occurrence and number of TRMM LPFs is even more highly correlated than the flash density. Almost all regions of the tropics and subtropics are in positive linear agreement between the trends in thunder-days and trends in number of LPFs. This indicates that the interannual variability of thunder-days is more correlated to the number of thunderstorms than the number of total flashes.

There are some regional cases however, in which the satellite trends are not verified by the ground-station measurements. Most notable of these areas are western Africa, north-central Africa, southeast Asia, and northern India. This disagreement led to an interesting finding in that in all of the poorly correlated regions (Figure 9), opposite or no correlation of the trends in number of thunderstorms and flashes/thunderstorm are observed. For example, Northern India observes an increase in annual thunder-days during the TRMM domain, but a subsequent decrease in lightning flash density. This disagreement can be explained by the fact that the region observes an increasing trend in number of annual thunderstorms, but a decreasing trend in flashes/thunderstorm, which indicates that the thunderstorms are becoming weaker. This led to the observation of more numerous thunder-days, but fewer total lightning strikes.

This finding is important because it illustrates the idea that trends in thunder-days and trends in flash density are not always correlated. An increase in occurrence of thunder-days over some regions cannot lead to the direct assumption that the total number of lightning flashes will also increase. More work is needed in the future to verify these claims, but it is important to point out the regions of agreement/disagreement in thunder-day/flash density trends over the past 16-years.

2.5 Summary

This study aimed to utilize over 8,000 ground-based stations over the course of 43-years, in order to determine global trends in thunder-day occurrence for the purpose of understanding how the global aggregate lightning activity has been shifting since the Industrial Revolution.

These thunder-day trends were also compared to the simultaneous trends in flash density, and number of thunderstorms observed by the TRMM satellite, in order to verify or counter the regional trends observed by the ground stations. The major findings include the following:

- Clear regional trends are observed by the ground station during the past four-decades in yearly thunder-day occurrence. Regions such as the Amazon, Maritime Continent, India, the Himalayas, Central America, Argentina, and the Congo all observe increases in thunder-day occurrence. In contrast, regions such as China, Australia, the Sahel, and parts of western Europe all display decreases in thunder-day occurrence. It is important to emphasize the significance that the majority of the selected regions exhibited significant increases in thunder-day activity in the past four decades, which corroborates the theory of an increase in lightning activity in a warming climate.
- Seasonal trends are also observed globally in thunder-day activity, with each season resulting in unique tendencies in regional thunder-day occurrence. Primarily the largest occurrence and steepest trends in annual thunder-days occur in the local summer season. The Maritime Continent and Amazon region exhibit a unique three-season active thunder-day period, with only the local winter season exhibiting a low occurrence. Of the nine sampled regions, only the SCUS does not show any statistically significant trends in thunder-days in any season. All the other eight regions display significant (p-value <0.05) for at least certain seasons, resulting in a changing seasonal as well as annual local

- climatology in thunderstorm activity.
- Regional spatial agreement is present between the trends observed in the ground station thunder-days and the satellite flash density, as well as annual number of LPFs. This provides evidence that the two independent data collection methods are corroborating each other. Regions such as the Maritime Continent, China, South Africa, and Argentina show strong positive correlation (r-value >0.58) between the trends in the thunder-day and flash density variables. These regions show an even larger correlation (>0.68) between the trends in thunder-days, and number of annual LPFs. All of these regions have at least a slight positive correlation between the trend in number of annual thunderstorms and the trend in the flashrate/thunderstorm. Other regions, for which there is disagreement on the relationship between trends in thunder-days and the flash density, all have negative or no correlation between the number of thunderstorms and the number of flashes/LPF.

The regional agreement between the ground stations and the satellite trends of several global regions that favor lightning activity, provides supporting evidence that satellites can be helpful in the future in monitoring global lightning shifts. As more data becomes available from the International Space Station-Lightning Imaging Sensor (ISS-LIS), as well as geostationary satellites, such as the Geostationary Operational Environmental Satellite-R Series Global Lightning Mapper (GOES-R GLM), we can continue to improve on determining the impact of climate change on lightning activity. The regions of disagreement, such as northern India, allow for interesting case studies into the region, showing that possible shifts in system type are occurring. For the case of northern India, the disagreement in flash density and thunder-day occurrence, indicates significant evidence that the area is receiving more thunderstorms that are

relatively weaker and produce less lightning.

Ultimately an insufficiently long satellite dataset is available to make any definite claims as to the trends in lightning flash density as it pertains to the changing climate. However, the combination of the satellite data, alongside longer-term ground station data, provides evidence that many regions are observing shifts in lightning activity at the interannual, annual and seasonal timescales. Monitoring this global aggregated joint seasonal-diurnal shift in lightning and other electrified parameters, can possibly be useful in the future in monitoring the changing climate. It is becoming clear that the relatively longer temporal span of lightning data from space is allowing for satellite technology to become more useful to determine the long-term variability of atmospheric electricity. By utilizing the past satellite record, alongside the newer satellite instruments such as ISS-LIS and GLM, we can understand with more confidence the variability of lightning and thunderstorms at various temporal time scales.

Table 2.1: 1975-2017 annual and seasonal mean, and annual and seasonal trends in thunder-days over nine selected regions.

		Congo	Argen	India	Sahel	SCUS	CAmer	AUST	Amazon	Maritime Continent
Annual	T-day (day/year)	122.62	43.35	28.41	65.53	58.52	58.01	4.73	66.67	74.55
	Variation (day/decade	6.9	2.6	2.0	-5.4	-0.9	4.7	-1.3	13.3	3.0
DJF	T-day (day/year)	30.92	19.97	1.05	0.11	5.75	0.62	5.75	21.37	9.66
	Variation (day/decade)	1.7	1.2	0.1	-0.1	0.2	-0.1	-0.8	4.0	0.7
MAM	T-day (day/year)	40.35	10.46	7.76	17.28	13.43	8.94	13.43	21.58	20.92
	Variation (day/decade)	2.3	0.5	0.7	-1.6	-0.4	0.5	-0.2	4.2	0.8
JJA	T-day (day/year)	14.82	1.83	12.40	34.10	31.71	29.33	31.71	6.09	20.05
	Variation (day/decade)	0.8	0.02	0.6	-2.2	-0.1	2.4	-0.1	1.7	0.6
SON	T-day (day/year)	36.61	11.18	7.20	13.49	6.68	18.85	6.68	17.73	20.89
	Variation (day/decade)	2.0	1.0	0.5	-1.5	-0.6	1.8	-0.4	3.4	0.9

Table 2.2. Correlation of regional lightning variables (r-values): Thunder-day (TD), Flash Density (FD), Flash Rate (FR), and Lightning Precipitation Features (LPFs) 1998-2013.

Region	TD-FR	FD-FR	TD-LPF	FD-LPF	LPF-FR	TD-FD
M.C.	0.23	0.56	0.93	0.94	0.25	0.88
China	0.76	0.92	0.69	0.81	0.55	0.81
Argentina	0.40	0.47	0.68	0.60	0.26	0.81
S. Africa	0.24	0.75	0.69	0.80	0.22	0.58
W. Africa	-0.41	0.69	0.55	0.23	-0.53	0.03
N. India	0.07	0.66	0.46	0.71	-0.04	0.43
SE. Asia	-0.42	0.81	0.68	0.21	-0.40	-0.04
C. Africa	-0.25	0.83	0.28	0.23	-0.36	-0.05

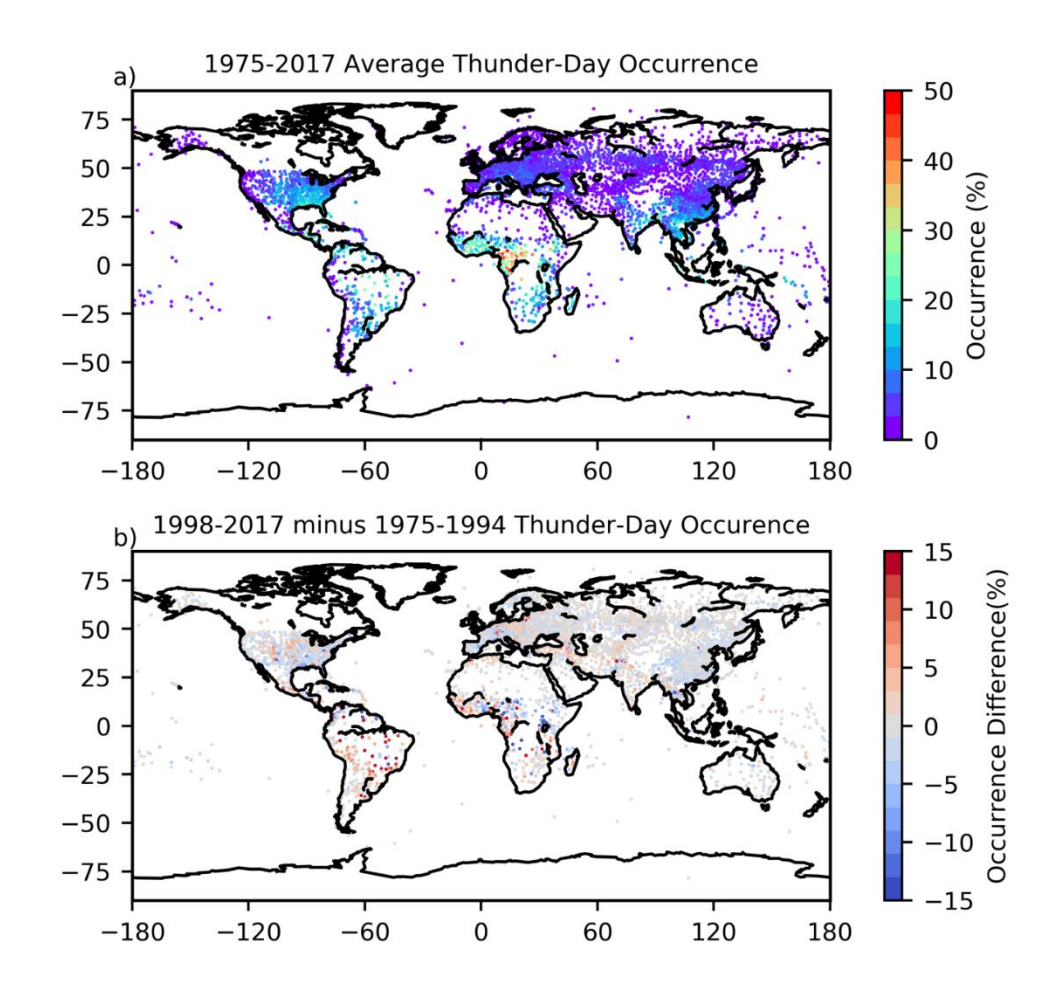


Figure 2.1: Difference in thunder-day occurrence at ground stations between 1975-1994 and 1998-2017. Data is excluded after 2013 in China due to the lack of thunder-day records. Thunder-day occurrence is calculated using the summation of all the thunder-days divided by the summation of all the total observation days is each region, and is represented as a percent.

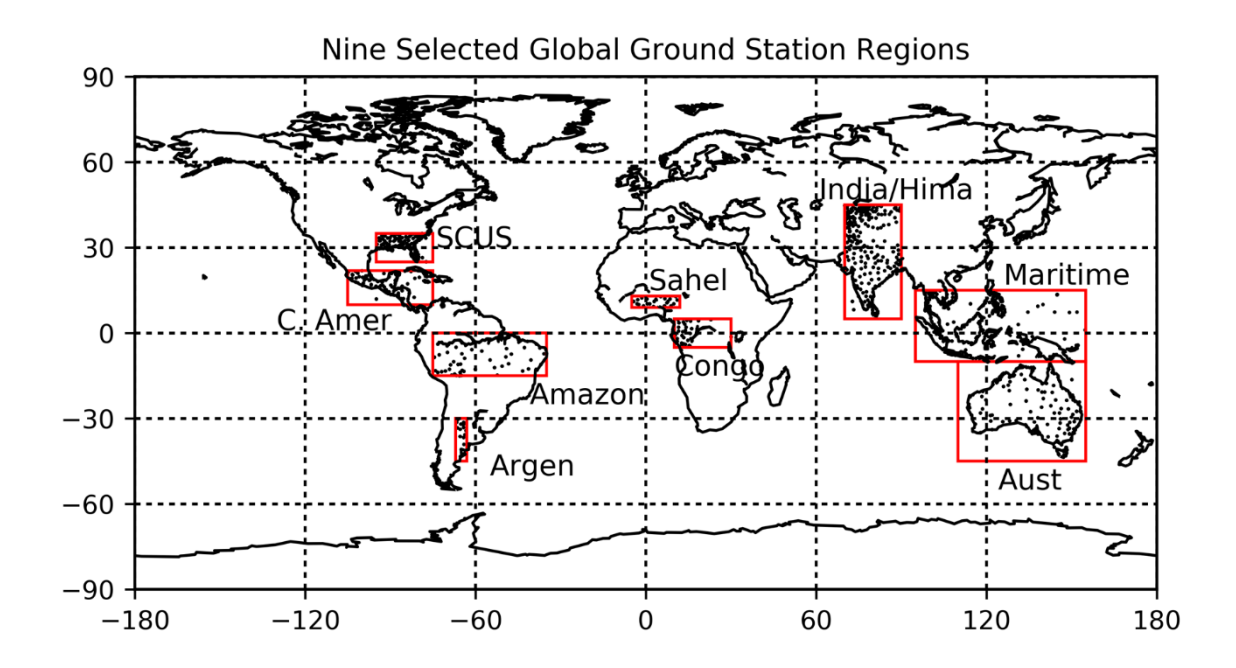


Figure 2.2: Nine selected convectively active regions. Each star represents a ground station.

1975-2017 Regional Thunder-Day Trends

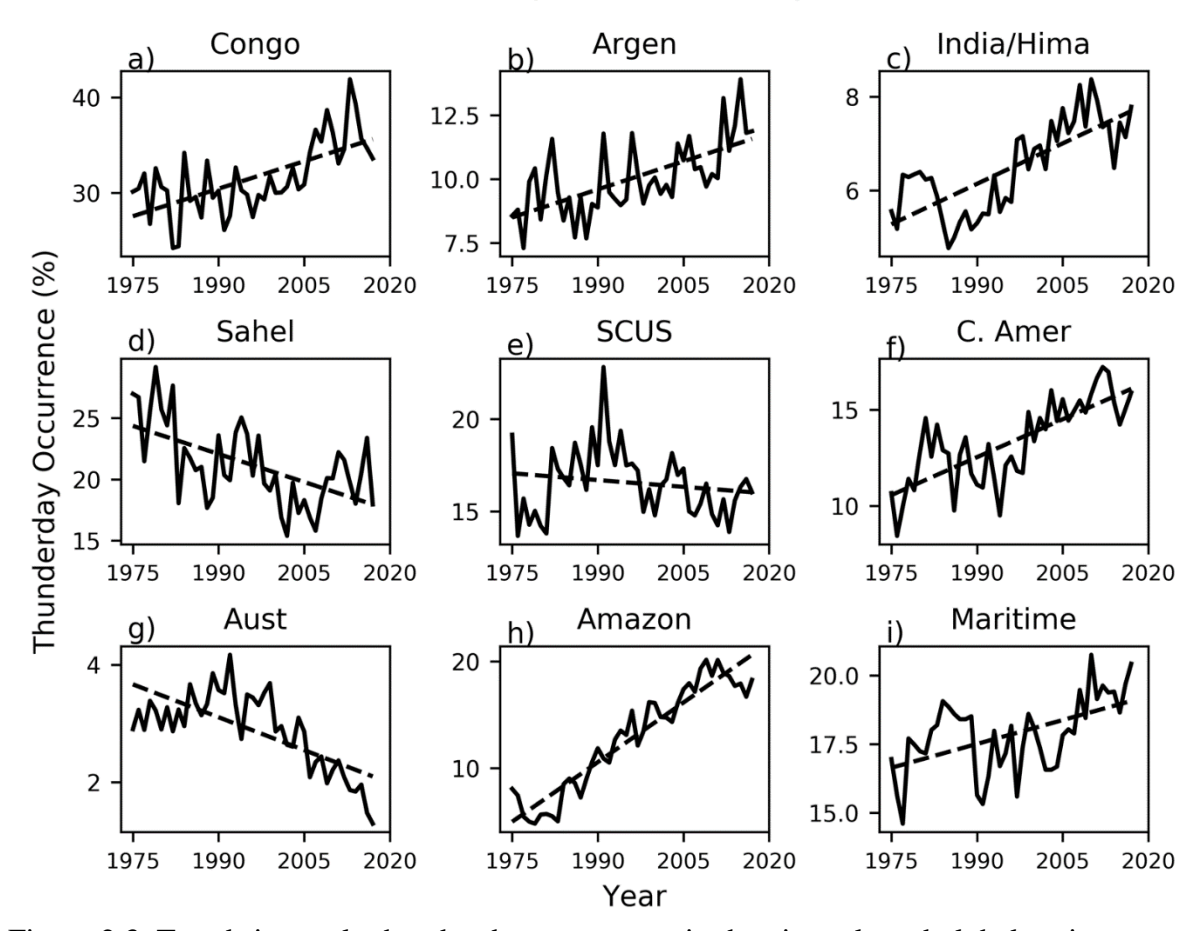


Figure 2.3: Trends in yearly thunder-day occurrence in the nine selected global regions. Thunder-day occurrence is calculated using the summation of all the thunder-days divided by the summation of all the total observation days per year in each region and presented as percentage.

2009-2013 minus 1975-1979 Seasonal Ground Station Trends

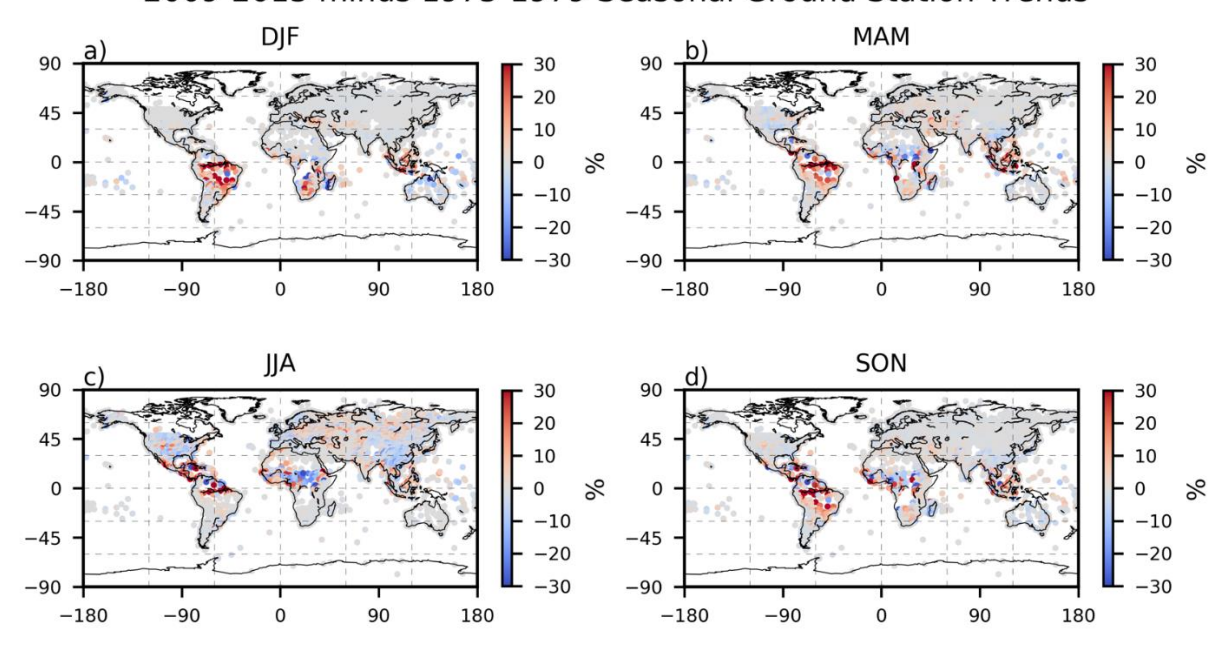


Figure 2.4: Seasonal trends in global thunder-day occurrence observed by the ground stations. Thunder-day occurrence is calculated using the summation of all the thunder-days divided by the summation of all the total observation days is each region and presented as percentage. Five-year averages were selected to reduce the impact of interannual variability such as a strong MCS event.

1975-2017 Seasonal Ground Station Trends

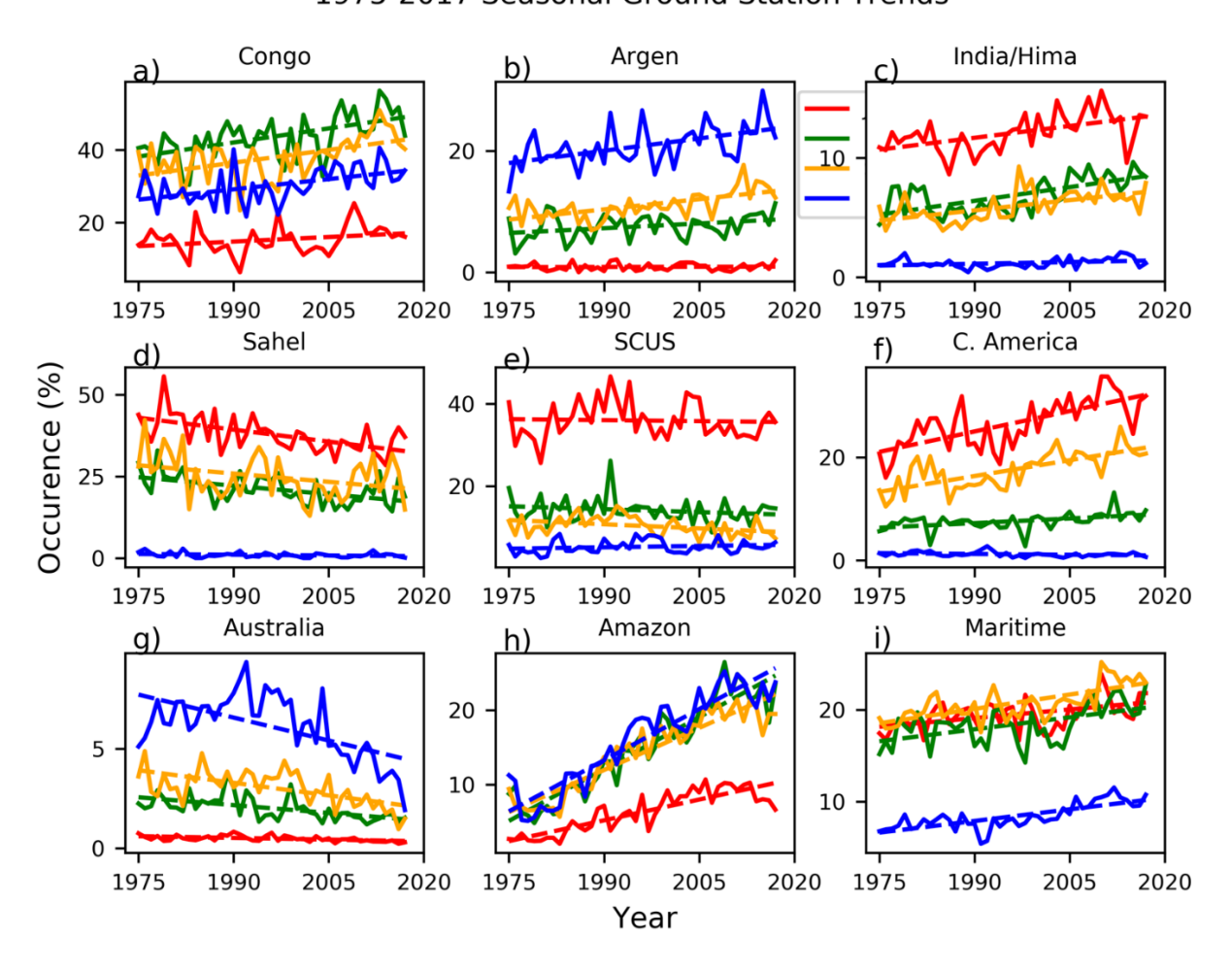


Figure 2.5: Seasonal trends in thunder-day occurrence in the nine-selected regions.

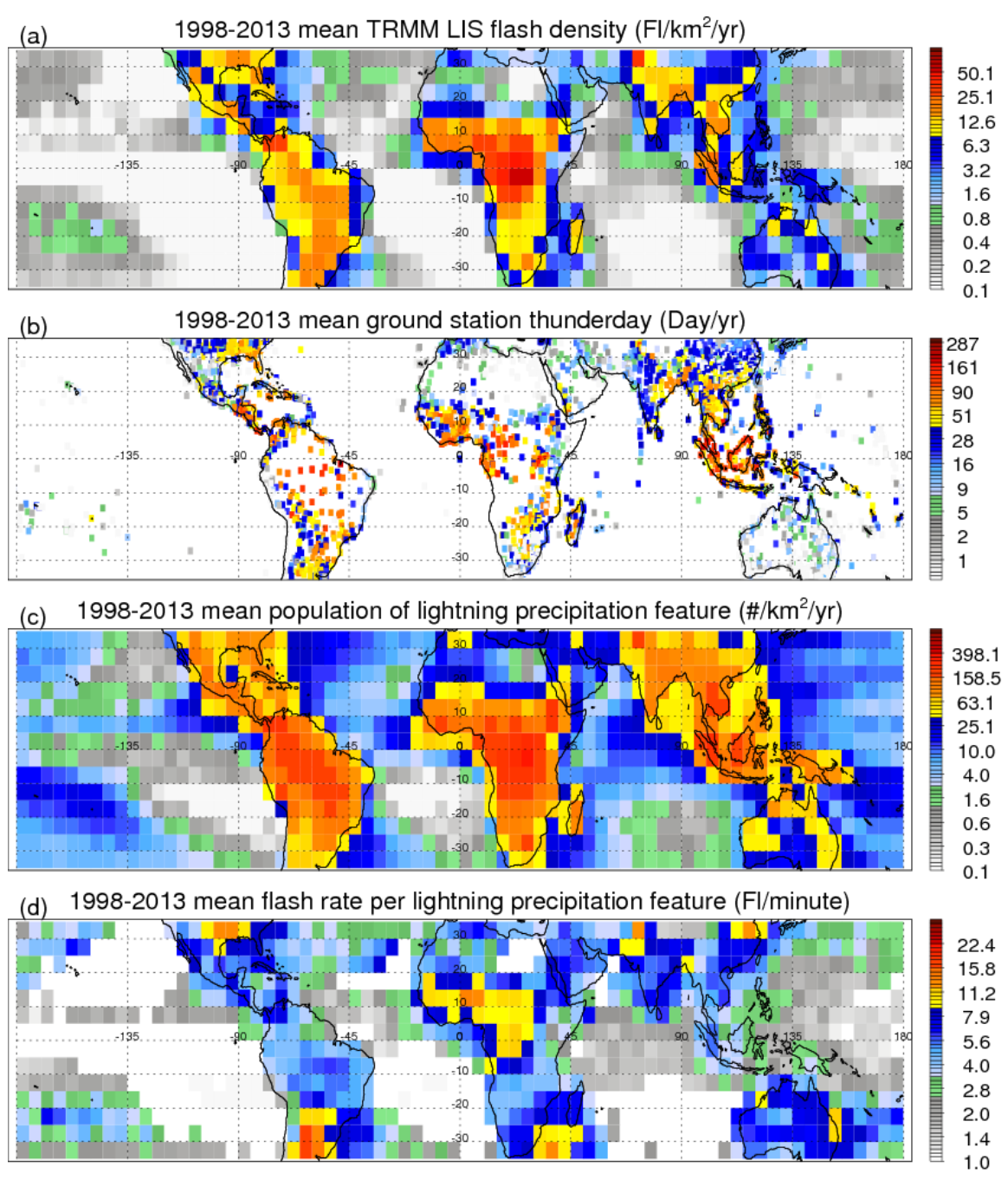


Figure 2.6: a) mean TRMM LIS flash density in 1998-2013 presented as flashes/km 2 /year over $5^{\circ}x5^{\circ}$ grids. b) Mean thunder-day reports per year from ground stations during the TRMM era, c) The mean population of lightning PFs ($\#/km^2/year$), and d) The average flash rate per lightning PF (flash/min/pf). All variables are averaged in 5x5 degree bins.

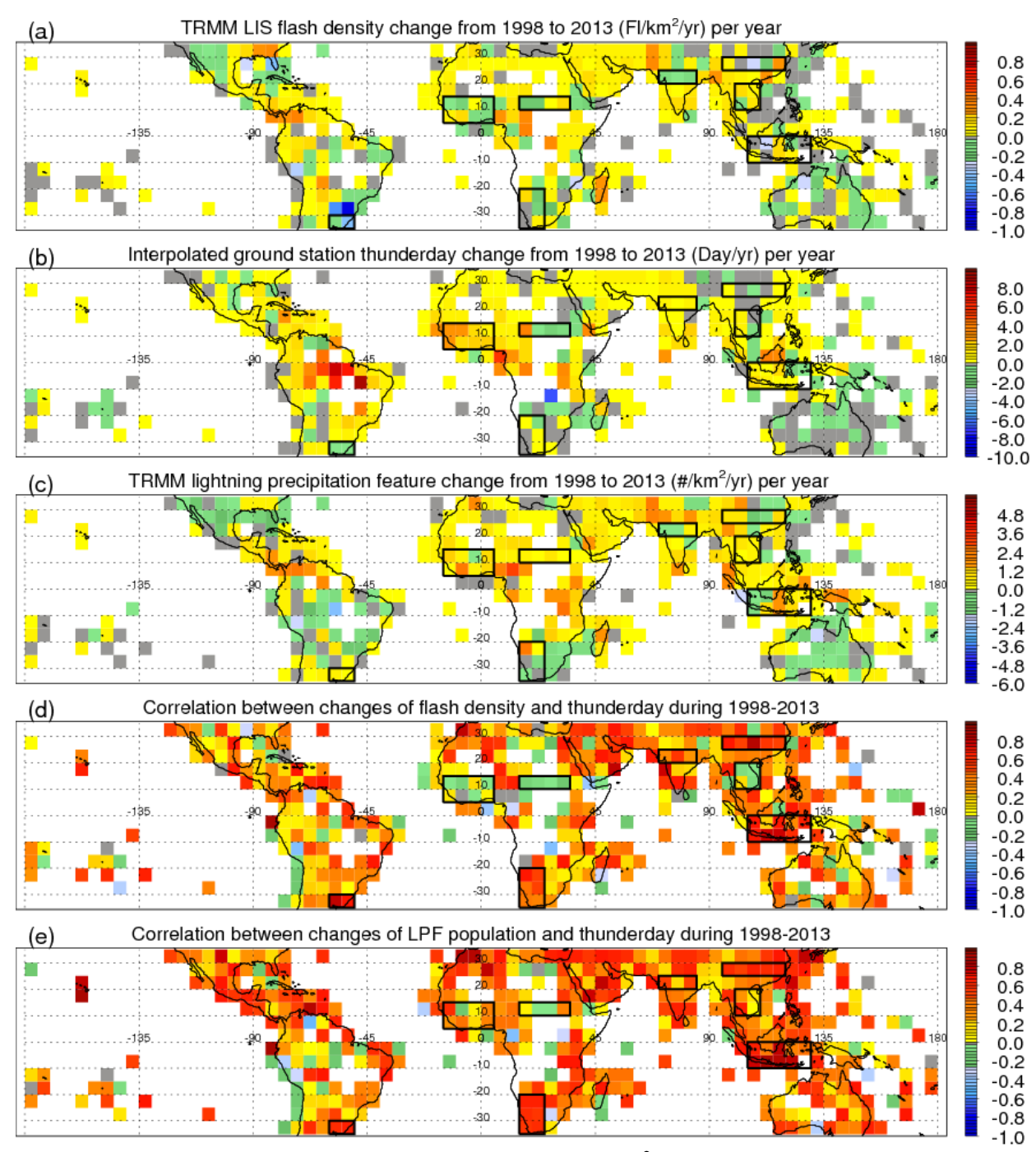


Figure 2.7: a) The trend in lightning flash density (flash/km²) as observed by the TRMM satellite. b) The interpolated ground station thunder-day trend between 1998-2013, c) The trend in number of LPFs observed by the TRMM satellite. d) The correlation between panel a and b for each 5°x5° bin. e) The correlation between panels b and c for each 5°x5° bin.

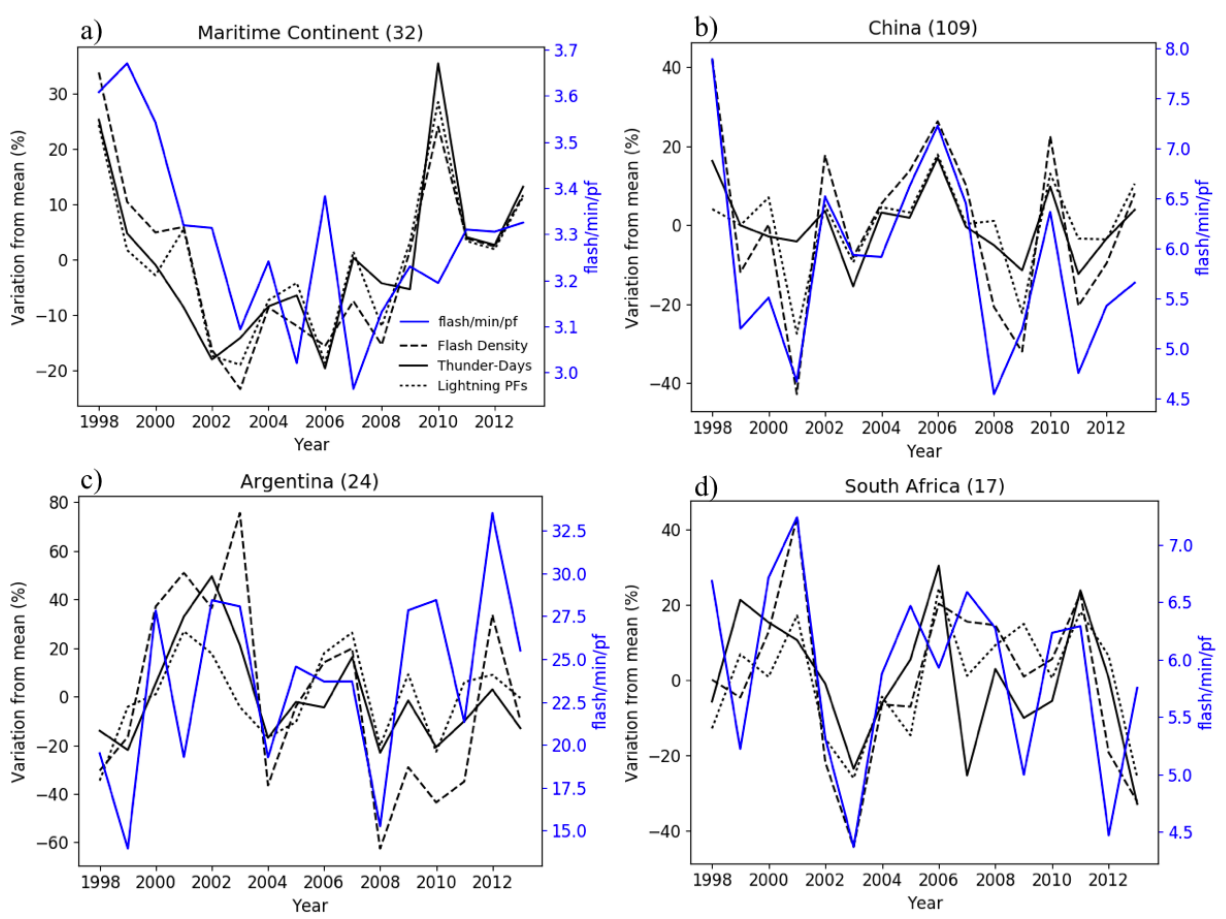


Figure 2.8: Time series of the number of annual thunder-days (solid), lightning flash density (dashed), number of lightning PFs (dotted), and number of flashes/minute/LPF (blue), observed in the TRMM domain (1998-2013) for four regions showing good agreement between thunder-days and lightning flash density. Flash density, thunder-days and LPF are expressed as a percent deviation from their 16-year mean (%) The number in parentheses indicates the number of ground stations in the region.

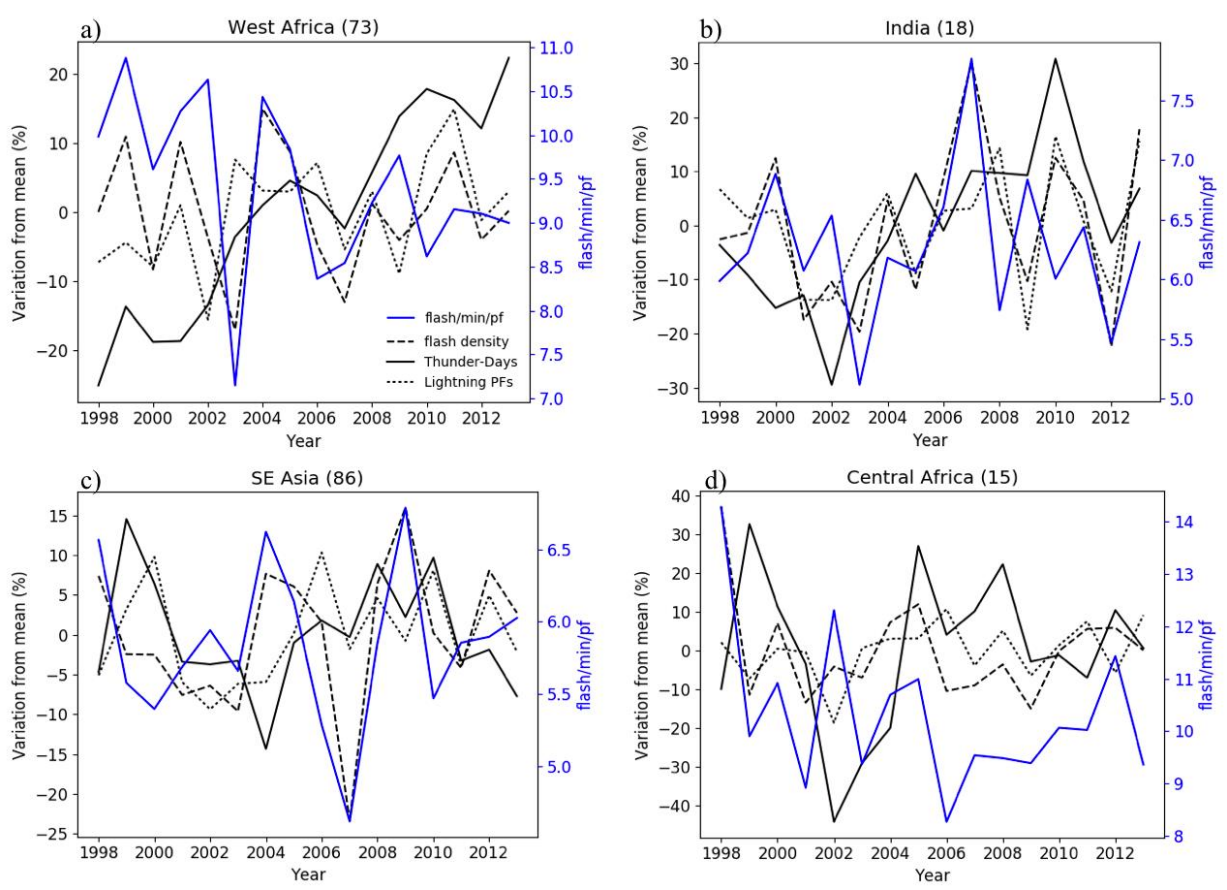


Figure 2.9: Time series of the number of annual thunder-days (solid), lightning flash density (dashed), number of lightning PFs (dotted), and number of flashes/minute/LPF (blue), observed in the TRMM domain (1998-2013) for four regions showing poor agreement between thunder-days and lightning flash density. Flash density, thunder-days and LPF are expressed as a percent deviation from their 16-year mean (%). The number in parentheses indicates the number of ground stations in the region.

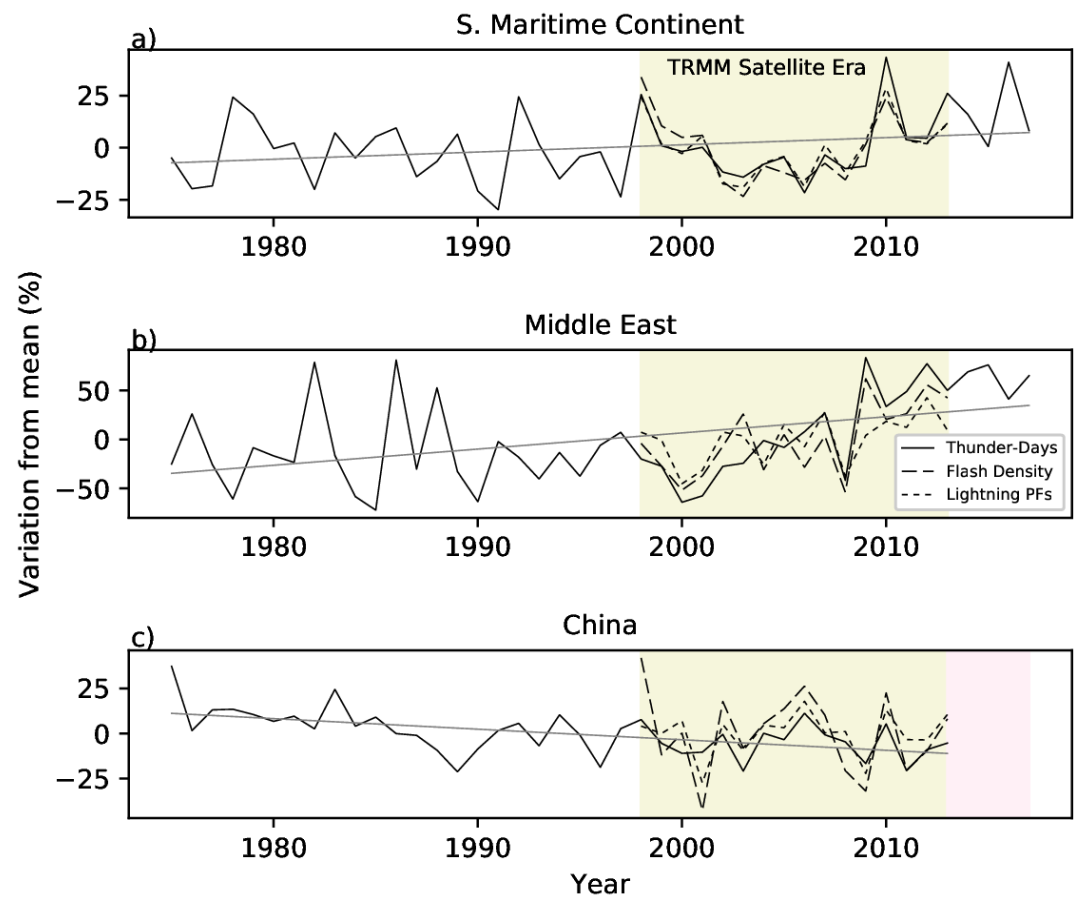


Figure 2.10: Time series of thunder-days (solid), lightning flash density (dashed), and number of lightning PFs (dotted) for three regions. The tan region shows the time period of the TRMM satellite era. No thunder-day data are available for the China region after 2013 represented in light red.

CHAPTER III: OBSERVATIONS FROM THE ONE YEAR ELECTRIC FIELD STUDYNORTH SLOPE OF ALASKA (OYES-NSA) FIELD CAMPAIGN, AND THEIR
IMPLICATIONS FOR OBSERVING THE DISTRIBUTION OF GLOBAL ELECTRIFIED
CLOUD ACTIVITY

3.1 Introduction

Several atmospheric electricity variables such as lightning, thunder days, and the electric field are useful in monitoring the changing climate [Williams, 1992; Reeve & Toumi, 1999; Rycroft et al., 2000; Williams, 2005; Lavigne et al., 2019; among others]. In 2016, lightning was added for the first time to the Global Climate Observing System's (GCOS) list of Essential Climate Variables (ECVs). [Global Climate Observing System, 2016; Aich et al., 2018]. However, the major shortcoming in utilizing the lightning parameter to monitor the changing nature of global storms, is the relatively short time period of global coverage of lightning flash data [Christian et al., 1999; Aich et al., 2018]. Only several decades of optical imagers onboard satellites, as well as ground-based Very Low Frequency (VLF) networks are available on even the quasi-global scale. While these data are very useful for understanding the variability of lightning and thunderstorms at the diurnal, seasonal, and even inter-annual scales, they are not sufficient in understanding the longer-term trends (if any) that are occurring in thunderstorm activity during the past century [Christian et al., 1999; Rodger et al., 2006; Blakeslee et al., 2014a]. An interesting alternative is to instead monitor a global system that is largely driven by global thunderstorm and electrified cloud activity, that has a much longer data record. The Global Electric Circuit (GEC) of the atmosphere is a vast Earth system of electrical currents that are present between the Earth's surface and Ionosphere [Rycroft et al., 2008]. Even during fairweather conditions, in the absence of significant clouds, aerosols, etc., a small current density of approximately 2 pA/m² is always present running from the Ionosphere in the upper atmosphere, down to the Earth's surface [*Rycroft et al.*, 2000]. Dating back to the early 20th century, it was hypothesized that the temporal variability of this fair-weather electric field, was produced by the simultaneous temporal variability of the summation global thunderstorm activity [*Wilson*, 1909; *Wilson* 1921]. Whipple, [1929], provided the first quantitative evidence of the link between thunderstorms and the fair-weather field by utilizing ship-borne vertical electric field data aboard the Carnegie cruise. The results indicated the maxima of both the GEC and thunder day area to occur at approximately 19 UTC, while the minima occurred at roughly 3 UTC. This diurnal cycle of the fair-weather electric field measured during this ground-breaking field work is now known as the classical Carnegie Curve [*Harrison*, 2013]. It remains the present-day view that the totality of thunderstorms around the globe at any given time, act as the main "battery" that continuously drives the GEC [*Williams*, 2009].

Throughout the next 90 years, many more details about the GEC have been revealed. With the addition of far greater amounts of electric field data measured around the globe, further details have been uncovered pertaining to the diurnal [Burns et al., 2005; Liu et al., 2010; Mach et al., 2011; Nicoll et al., 2019; among many others], seasonal [Adlerman & Williams, 1996; Liu et al., 2010; Burns et al. 2012; Blakeslee et al., 2014b; among many others], interannual [Burns et al., 2005; Williams & Mareev, 2014; Lavigne et al., 2017] and even decadal [Markson, 2007] variability of the GEC. In the past several decades, the addition of quasi-global radar measurements from space, as well as optical lightning imagers, have allowed for thunderstorms, and electrified precipitation systems to be analyzed in greater detail [Christian et al., 1999; Goodman et al., 2013]. The combination of the improvements in coverage of electric field

measurements, as well as vast advancements in the global measurement of thunderstorm and cloud activity, has allowed for corroboration and extension of Wilson's and Whipple's findings.

The El Nino Southern Oscillation (ENSO) variability has also been observed in fairweather electric field data [Hamid et al., 2001; Satori & Williams, 2009; Lavigne et al., 2017]. The regional increases and decreases in thunderstorm and electrified cloud occurrence on the ENSO time scales has been noted to also be simultaneously observed in the fair-weather electric field measured in Vostok Station, Antarctica [Lavigne et al., 2017]. For example, during the Southern Hemispheric summer months, an increase in both precipitation from thunderstorm and electrified clouds, as well as flash count was observed by the Tropical Rainfall Measurement Mission (TRMM) satellite during the hours of 16-24 UTC in La Nina periods. South America, which is known to be convectively active during this time, also observes an increase in thunderstorm and electrified clouds during these La Nina periods [Williams and Stanfill, 2002; Liu et al., 2010, Lavigne et al., 2017]. This increase in both electrified precipitation features, as well as the GEC during this time period, indicates that indeed the regional enhancement/suppression of thunderstorms as a result of ENSO can simultaneously be observed in the variation of GEC electric fields as well. This type of finding provides further evidence that the GEC is directly tied to the variability of global/regional thunderstorm and electrified cloud activity on a scale of natural climate variability (approximately 2-7 years). This allows for the next logical question to be asked; whether or not the GEC can monitor the longer-term climate variability over the past 100-years?

For all the progress that has been made on understanding and modelling the GEC of the atmosphere, there are still many unknowns pertaining to the smaller-scale contributing input parameters. *Kalb et al.*, [2016] had some success at parameterizing storm conduction currents in

the TRMM domain, and applying them to a global Earth model. However, the output models had a significantly smaller diurnal amplitude, and peaked approximately 4-6 hours before the Carnegie curve. This could imply that there are several other factors not included in the budget that play an important role in driving the GEC system. As a general rule, thunderstorms and electrified showerclouds (defined as precipitation systems that produce significant charge separation but do not generate lightning) are the main driver of the GEC [Rycroft et al., 2007; Mach et al. 2009; Liu et al., 2010; Peterson et al. 2018]. However, it has been well established that many other physical processes contribute to the system. These include cosmic galactic rays, geomagnetic processes, energetic solar particles as well as many others [Tinsley, 2000; Siingh et al., 2007; Baumgaertner et al., 2013, among others]. In addition to these, many other localized processes are known to influence the local vertical electric field, such as aerosols, non-raining clouds, blowing dust and snow, fog, radon gas release, auroras, etc.

Several past studies have examined the influence of several of the above-mentioned localized influences on the measured vertical electric field. The typical magnitude of the physics convention fair-weather electric fields measured on the surface at sea level varies from approximately -100 to -200 V/m. It should be noted that throughout this manuscript, the physics convention of fair-weather electric fields will be used. Fair-weather electric fields will be represented as negative, and the potential gradient will be represented as positive values. *Lucas et al.*, [2017] concluded using that during fog conditions, the Earth's electric field deviates from the background fair-weather electric field by roughly +150-200 V/m. The same study concluded that during an overcast day, the electric field varied by approximately -40 to -50 V/m from typical fair-weather values. This indicates that non-electrified clouds and fog contribute relatively weakly to the localized electric field. However, several studies have shown that

blowing snow can cause a much larger influence on the electric field. *Schmidt et al.* [1999] concluded that surface electric field measurements during even a moderate blizzard can deviate the electric field on the order of +30,000 V/m. Model outputs conducted by *Gordon and Taylor* [2009] seem to corroborate this result, indicating that electric field magnitudes can exceed 25,000 V/m during surface blowing snow events. *Chmielewski* [2013] studied the influence of blowing dust on the surface vertical electric field in West Texas. The study found that a typical blowing dust event causes a +4000 to +5000 V/m effect on the electric field. However, during intense events, the effect can be as a large as +15,000 V/m based on case studies.

At high latitudes, snow cover may slow the release of radon from the ground which changes the conductivity of the near-surface atmosphere. *Baumgaertner et al.*, [2013], found that direct natural radiation emitted from surface, as well as ground decay of radon gas, lead to approximately 10 ion pairs cm⁻³s⁻¹ over land between the latitudes of 60°N-60°S. In higher latitude regions where ground snow coverage is more prevalent, the rate was found to be reduced to half, creating a variation in the surface conductivity of up to 200% [*Baumgaertner et al.*, 2013].

Furthermore, in high-latitude regions, aurorae are present. These solar wind disturbances can have intense effects on localized electric field measurements in polar regions. A case study, conducted by *Olson* [1971], concluded that during an incident of visual aurora near the measurement site, the surface electric field was disturbed on the order of 1000 V/m for several hours. During this time period, the sky was clear with no visible clouds indicating that the significant jump in the surface electric field was due to the solar event. The study further indicated that there are two main types of aurorae events: 1) events that produce negative E_z for approximately 30 minutes and then return to fair-weather magnitudes, and 2) events that more

significantly shift the E_z towards negative values, and last on the order of several hours [*Olson*, 1971]. More recent studies on aurora influence such as *Lucas et al.*, [2015], concluded that in arctic regions of the globe, the amplitude of magnetospheric perturbation can be as large as 50% of the GEC potentials, and can either constructively or destructively interfere. *Reddell et al.*, [2004], conducted a magnetospheric correction due to the cross-cap potential of the vertical electric field. This diurnal correction was found to have the largest sinusoidal variability of +15 V/m at roughly 7 UTC and -25V/m at approximately 21 UTC during periods of high magnetic activity. This correction factor was found to be in good agreement with several other past studies at high latitudes [*Tinsley et al.*, 1998; *Corney et al.*, 2003].

To address the mystery of the localized inputs to the electric field, as well as to build upon the understanding and possible practical uses of the global aspect of the GEC, a field campaign has been created in the unique location of the North American Arctic. The One-Year Electric Field Study-North Slope of Alaska (OYES-NSA) field campaign was established in June of 2017 at the Department of Energy (DOE) Atmospheric Radiation Measurement (ARM) Northern Slope of Alaska (NSA) site. With the goal of understanding the contribution of the unique localized parameters in the region to the electric field, as well as to utilize the fair-weather electric field to monitor electrified cloud activity around the globe, this student-led field campaign was established in the northernmost town in the USA, Barrow, Alaska.

The North Slope of Alaska (NSA), provides a unique study site to monitor both local influences on the vertical electric field, as well as the fair-weather global component. The region observes unique Arctic cloud formations, which have shown at times to become significantly electrified. The North Slope of Alaska is an ideal location for measuring these electric field values, due to the stably stratified boundary layer that exists in the extremely cold temperatures

[*Burns et al.*, 2005]. In addition to the unique nature of the site (i.e. blowing snow, Arctic clouds), the site is also very well instrumented. The location has a co-located Ka-band radar, a Micro-Pulse Lidar (MPL), as well as much other supplementary meteorological information.

The unique vertical separation of two electric field meters (one at 2 m and the other at 5 m), allows for the investigation of local space charge concentration in the region. *Marshall et al.* [1999], studied the sunrise effect in the fair-weather electric field at Kennedy Space Center in Florida. Results from the study found that enhancement measured near sunrise was due to the upward mixing of the dense electrode layer very near the surface. The presence of two electric field mills separated by several meters can help determine if the conductivity changes above the electric field mills, or if local space charge is introduced such as in the cases that Marshall studied.

The site, which is one of the only electric field records in the Western Hemispheric Arctic, aims to shed light on the contribution of the unique local influences on the electric field budget, as well as to monitor the global component or GEC from the Arctic, in order to better understand the variability of global thunderstorms and electrified clouds at various timescales.

3.2 Data and Instrumentation

3.2.1 Study Location

The OYES-NSA field campaign instrumentation site is located on the grounds of the DOE ARM North Slope of Alaska site. The site is located at approximately 71.3°N and 156.6°W, near Barrow, Alaska, making it the northernmost electric field monitoring site in the United States. In addition to the main study site of the field campaign, a supplementary electric field observation is simultaneously monitored in the sub-tropical region of Corpus Christi, Texas. This site is located at 27.7°N and 97.3°W on the Texas A&M University-Corpus Christi campus.

Figure 1b displays a map of the geographical location of both of the electric field meter sites separated by 6015 km.

3.2.2 Instrumentation

Figure 1a shows the main instrumentation setup at the Barrow, AK site. At this location, two Campbell Scientific (CS110) electric field mills are positioned at two different heights. The lower CS110 is set at approximately 2 m off the ground, while the higher field mill is oriented at approximately 5 m off the ground. This setup allows for a slight vertical profiling of the near-surface electric field, which could help understand the influence of blowing snow and other surface interactions. In addition to the two electric field meters, a RM Young Alpine anemometer is located near the lower electric field meter. The CS110 electric field mills are set up to sample at a rate of 1 Hz. It is important to note that the CS110s measure the vertical electric field in the orientation in which fair-weather fields (downward fields) appear negative.

The white building located in distance of the field meter setup in Figure 1a (approximately 100m away) houses the data retrieval computer, as well as supplementary instrumentation sources. On the top of this building, sits a vertical pointing Ka-band radar (KAZR), as well as a vertical profiling 532 nm Micro-Pulse Lidar (MPL), as well as many other instruments maintained at the DOE ARM site.

The Corpus Christi, TX site includes one CS110 that also samples at a rate of 1 Hz. This field meter is set at approximately a 2 m height. The location includes supplementary temperature, wind, relative humidity, solar irradiance from a weather station 10 m away from the CS110.

3.2.3 Calibration

In order to establish a ground surface measurement of the vertical electric field at the NSA and Corpus Christi sites, rigorous calibration was conducted. To remove the influence of the metal mounting poles, as well as other nearby instrumentation setups, a ground-level upward facing measure of the vertical electric field was taken similtaneouly to the downward facing CS110s on the pole. The upward facing measurement was taken far away (greater than 3-times the distance of the height) from any metal or powerline influences, and provides the "true" undisturbed vertical electric field measure. The two operational CS110 instruments on the pole were then calibrated to match these values using a linear calibration multiplier and intercept [Chmielewski, 2013]. The simple calibration equation is as follows:

$$\mathbf{E}\mathbf{z}_{\mathbf{ground}} = \mathbf{a} \bullet \mathbf{E}\mathbf{z}_{\mathbf{pole}} + \mathbf{b} \tag{1}$$

Where Ez_{ground} is the ground flush electric field meter measurement (V/m), Ez_{pole} is the raw electric field measurement on metal pole (V/m); a and b are slope and intercept constants after the linear regression.

Figure 2 shows the calibration process. As the metal mounting setup causes the vertical electric field lines to bend toward the pole, calibration is needed to correct for this effect. As shown in Figure 2a and Figure 2c, the calibration factor for the 5m CS110 is a multiplier of 0.823 and intercept of -54.9, while the factor for the 2m CS110 was determined to be a multiplier of 3.121 and an intercept of 16.69. With the inclusion of these calibration factors, the metal-mounted CS110s match the undisturbed ground-flush E_z measurements at a near 1-1 relationship, indicating an "absolute" measure of the Ez_{ground} . This ground-flush calibration process was repeated at the Corpus Christi site, resulting in a calibration factor of 1.747 and the intercept of -42.55. It should be noted that in November of 2018, a CS110 instrument swap took place due to

maintenance of the preexisting instrument. Rigorous testing concluded that an instrument swap resulted in an absolute electric field discrepancy of less than 10 V/m, which is well within the margin of error of the CS110 of +/- 5% +8 V/m.

3.2.4 Supplementary Data

One of the advantages of monitoring the electric field at the North Slope of Alaska DOE ARM site, is the availability of supplementary instrumentation on site. The site is home to multiple radars, a Micro Pulse Lidar (MPL), as well as numerous other meteorological measuring equipment.

The Ka-Band radar, also known as the KAZR, is an upward pointing Doppler radar that operates at a frequency of approximately 35 GHz. The three main return measurements are, reflectivity, vertical velocity and spectral width. The sample rate is 30 seconds and measures in a vertical range of approximately 30 m to 20 km. The MPL lidar is an upward pointing optical remote sensing instrument, that is used to detect aerosols as well as cloud altitude. The MPL operates at a wavelength of 532 nm. The MPL samples every 30 seconds with vertical resolution of 15 m, with a maximum height of approximately 20 km. For the purpose of this study, 5-minute maximum column backscattering coefficient are used, which denotes the maximum backscatter signal observed by the MPL anywhere in the vertical column during the 5-minute period of time. Both KAZR and MPL lie approximately 100 m (near the background building in Figure 1a) from the electric field measurement site.

To determine blowing snow, fog, as well as haze days in Barrow, Alaska during the operating period of the field campaign, the National Climatic Data Center (NCDC) Monthly Climate Data F6 product is used. This dataset includes the daily maximum and minimum temperatures, dew point temperature, precipitation, snow depth, wind speed and direction, as

well as a weather flag. The weather flag indicates a binary occurrence of events such as fog, thunder, ice pellets, hail, freezing rain, dust, haze, smoke and blowing snow. The location of the data collection is in the town of Barrow, Alaska (71.17 N, 156.47 W.)

3.3 Results

3.3.1 Examples of Influences on the Electric Field by Various Factors

In order to better understand how the supplementary data can be used to interpret deviations observed in the vertical electric field measurements, four example cases are shown under different and unique environmental conditions. The four following cases all occur in Barrow, Alaska and are shown with the Ez_{ground} from the calibrated 5m CS110 measurements.

3.3.2 Significantly Charged Precipitation Event

Figure 3 shows an event in Barrow, AK in which a significant precipitation event crossed overhead of the instrumentation. The case occurred during the warm season on July 3, 2018. At approximately 23:25 UTC, a leading anvil edge began to pass above the field meter at an altitude of approximately 2.5 km (Figure 3a). This cloud introduced a strong negative field (Figure 3b) on the order of -5000 V/m. During this time period, no precipitation appears to be present on the ground as evidenced by Figure 3a and Figure 3c displaying no significant radar reflectivity below 3km, as well as no lidar backscattering signature near the surface. At approximately 23:30, larger reflectivity appears overhead at the field meter and at lower altitude. This more convective-like signature (>30 dBZ) begins to gradually drive the electric field strongly positive, reaching a maximum of roughly +12,000 V/m. It appears that two separate raining cells are present. In between, a radar bright band and lower reflectivity at the surface suggests a short period of stratiform-like non-raining cloud, associated with a negative dip in the electric field at approximately 23:35 UTC.

This relatively highly-electrified case (for the Arctic) indicates that the Ka-band radar can be very useful in determining large variation and swings in the electric field. Clouds with reflectivity greater than 20 dBZ show strong qualitative correlation to the electric field variability and magnitude. Furthermore, the Ka-Radar shows the ability to distinguish different cloud-regions of the precipitation events such as the leading anvil, convective, raining, stratiform, etc. Strongly electrified cases also show that the MPL is almost instantly fully attenuated upon the presence of the strong precipitation feature (Figure 3c). Other than the possible use of determining precipitation at the near-surface, the MPL can also be useful in determining that the surface air was relatively clean for this case.

3.3.3 Aerosol/Lidar Dominant Event

Figure 4 shows an event that occurred on August 12, 2017. The case exhibits a very stable cloud that occurs from approximately 3 km up to 8 km (Figure 4a) throughout the entire 7-hour case. Despite the relatively stable and unchanging Ka-radar reflectivity, Figure 4b shows that strong short-lived jumps in the vertical electric field are present throughout the case, on the order of +400 to +700V/m. This variability is simultaneously observed very clearly in the MPL backscattering signature in Figure 4c. Very clear backscattering on the order of 250-400 km⁻¹Sr⁻¹ in the lower 200-300m of the atmosphere is observed during the time of the electric field spikes. Figure 4c shows that the particles causing the strongest backscatter occurs very near to the surface. This indicates that the spikes observed in the electric field are caused by aerosols or cloud very near to the surface that are difficult to observe with the Ka-radar. Examples of this type of signature could be dust, salts, fog, etc. very near to the surface. Due to the case taking place in the warm season, this is not consistent with a blowing snow type event.

This type of case is frequent in the NSA region throughout the year, with short lived spikes in the electric field observed nearly every day. The MPL backscatter is shown to be very useful in determining these time periods, with a high visual correlation between the short-term electric field variability and backscattering in the lower 0.5 km of the atmosphere. The variability of the electric field in cases such as these is not clearly observed in the Ka-reflectivity (figure 4a). This indicates that these low reflectivity stratus clouds are not the driving cause of this E_z variability shown in Figure 4. When the near surface aerosol information is also simultaneously observed, it is clear that the E_z variability is well correlated to the short-term variations of high backscattering from the near surface. This illustrates the importance of being able to monitor the cloud as well as surface aerosols when understanding the variability of the E_z .

3.3.4 Blowing Snow Event

Figure 5 shows an event that occurred on November 9, 2018. This event occurred during the cold season in the NSA. Based on the NCDC F6 product, surface observations, the temperature varied from -13.3 to -6.7°C and also indicates a snow pack was present on the ground with a depth of 7 inches. The initial period of the case (8-11 UTC) shows very little if any cloud activity according to the Ka-reflectivity (figure 5a). Likely due to blowing snow covering the instrument, the MPL did not collect any useful information for this case. During this time period, Figure 5b shows that a variability of both the 2m electric field meter (red) and the 5m electric field meter (blue) of approximately 100V/m is present in the vertical electric field, with sharp jumps present. This variability correlates to both the U-vector wind speed with a correlation coefficient of 0.45 (Figure 5c), as well as qualitatively to the total wind speed (Figure 5d). This indicates that during this case, particles are blown aloft in the wind, and simultaneously influence the vertical electric field due to the conductivity change. During periods with wind

speeds above 2 m/s, the electric field becomes less negative (-25 to -50 V/m). Based on the study by *Schmidt* [1982], an approximate 3-5 m/s wind speed is required to start larger-scale blowing snow transport. However, based on figures 5c and 7, it appears that very small ice particles (less than blowing snow requirements) begin to be thrown aloft at 2m/s wind speed and start to influence the conductivity of the air. This is possibly the cause of the relatively larger difference observed between the 2 m CS110 and the 5 m CS110 when the wind speed becomes greater than approximately 2 m/s (Figure 5b). This is observed because the two electric field mills are no longer encountering the same environment, with the lower elevated CS110 theoretically surrounded by a larger number of tiny particles due to the wind. When the winds return to approximately 1 m/s, both the 5 m and 2 m electric field mills sharply recover back to normal fair-weather values for this time of year of approximately -150 to -200 V/m.

Blowing snow events are very common in the NSA, which observes nearly year-round, except a few months in summer, snow coverage as well as high winds throughout the year. This case emphasizes the extremely common very low magnitude blowing snow events (50 to several hundred V/m) that are nearly always present in the winter months. During blizzard conditions, much more obvious deviations on the electric field are present. It is very important especially when considering fair-weather to be able to identify these very weak but significant deviations in the E_z caused by snow particles aloft.

3.3.5 Aerosol Influence Event

Figure 6 shows an event that occurred on July 1, 2017. Figure 6a displays that almost no precipitation activity was present during the entire case, with several small clouds of less than - 10 dBZ occasionally present around 4-5 and 9-10 km. However, the vertical electric field observed significant variability throughout most of the day on the order of magnitude of several

hundred V/m. The variability observed in the electric field (Figure 6b) corresponds to the simultaneous presence of MPL backscattering (Figure 6c). During periods of relatively intense backscattering (>100 km⁻¹Sr⁻¹), the standard deviation of the E_z increases, fluctuating several hundred V/m in the timespan of less than an hour. However, there is a time period where there are no significant clouds (>-10dBZ), as well as virtually no MPL backscattering between the hours of approximately 3-9 UTC. During this time period of no observed electrified clouds or aerosols, a very stable vertical electric field is present at approximately -150 to -200 V/m, which is consistent with the fair-weather range. This period of time can be presumed to be measuring the fair-weather vertical electric field, representing the true global component of the E_z, known as the GEC.

It should be noted that even non-electrified clouds, potentially such as the low reflectivity clouds observed in Figure 6 between 2-8 UTC at an altitude of approximately 9-10 km, can still influence the current density of the fair-weather return current [Baumgaertner et al., 2014]. Clouds such as these in the fair-weather region of the GEC were found to increase global resistance by up to 73% of the cloud free atmospheric resistance [Baumgaertner et al., 2014]. Furthermore, a single cirrus cloud similar to the cloud observed in Figure 6, was found to create a strong reduction of the average current density from approximately 2.5 pAm-2 to 0.6pAm-2 [Baumgaertner et al., 2014]. The influence of these non-electrified clouds to the determination of fair-weather in the NSA region should be addressed further in the future.

This case study result indicates the possibility of quantitatively utilizing radar observed cloud and Lidar indicated aerosol data to be able to determine these fair-weather periods with more precision. This is extremely important for the NSA site where these periods of fair-weather

are not common. Being able to piece together shorter periods (minutes to hours) of fair-weather into a composite is crucial at NSA to understand the variability of the GEC measured at the site.

3.3.6 Wind Influence of the Vertical Electric Field

One objective of the OYES-NSA field campaign is to utilize the unique location of Barrow, Alaska to better understand how wind-blown particles can influence the electric field measurements. The location has the advantage of the presence of snow on the ground for much of the year, as well as proximity to the Arctic Ocean (about 2 km to the coast). This allows for the opportunity to study situations of blowing snow, fog, sea salt, dust, among others. Even under conditions with no clouds present, this region observes days with large E_z deviations from fair-weather values. Figure 7 shows the difference in the Ez measurements between the two CS110s each at a different height versus the wind speed for two months, one in the cold season (Figure 7a-b) and the other in the warm season (Figure 7c). In Figure 7a, the color fill indicates blowing snow days in Barrow, AK as determined by the National Climatic Data Center (NCDC) monthly climate data F6 product for the month of January 2018. The contours indicate hazy days determined by the NCDC F6 product. Figure 7a shows that a threshold of approximately 2 m/s is needed to start to significantly deviate the recordings from the two instruments from one another, which is supporting the blowing snow scenarios. With wind speeds of approximately 2-5 m/s, the 5m electric field meter tends to record a significantly lower E_z reading of up to -2000 V/m. The presence of both the color fill, as well as contours, indicate that this influence from wind could either be due to blowing snow or haze. However, when the wind speed reaches 8 m/s and above, only blowing snow days are present, and the 5 m CS110 tends to record larger E_z values than the 2 m CS110, up to 1000 V/m.

Figure 7b compares blowing snow days vs. clear days in Barrow Alaska as determined by the NCDC F6 data. A clear day is defined as having no significant weather events as defined by the NCDC (i.e. fog, thunder, ice pellets, freezing rain, dust, smoke, haze, blowing snow, etc.)

The contours show that on clear days in the cold season, a much smaller deviation between the 5m and 2m CS110 is present when the wind speed is higher than 2 m/s. The vast majority of the measurements occur within 100 V/m of each other, with most much closer than that. It is also important to note that no clear days were recorded with wind speeds above 6 m/s during the month.

Figure 7c exhibits the difference between the 5-m and 2-m electric field mills in a warm month of August 2018. There is much less deviation between the top and bottom CS110s as a function of wind speed in summer. This is likely due to the fact that no ground snow is present in August in this area. Figure 7c shows that a few cases above 6 m/s, tend to deviate the two CS110s from one another (up to 2000 V/m), These periods of time were determined to be significant raining events as shown in Figure 3, and not related to the surface wind environment.

It should also be pointed out that although this work focuses on the blowing snow effect on the difference between the measured E_z at the 5 m and 2 m electric field mills, some of the difference could be due to surface radon release, which could also influence the conductivity of the air. The difference between the 5 m and 2 m electric field mills in the winter months, corroborates this as radon release can be suppressed by the presence of ground-based snow [Baumgaertner et al., 2014]. This creates an electrode layer near the surface could potentially create a vertical gradient of E_z [Marshall et al., 1999]. Further investigation is needed in the future to quantify the influence of radon release on the vertical electric field at the NSA site.

3.3.7 Determination of Fair-Weather

One great advantage of locating the OYES-NSA field campaign at the DOE ARM site, is the plethora of supplemental instrumentation available. As shown in the above cases (Figures 3-6), the MPL lidar is very useful in determining periods of high amounts of aerosols, rain occurrence, low-level cloud activity, etc. This indicates the possible usefulness of this instrument in helping to select periods of fair-weather electric fields. Figure 8 exhibits averaged E_z values versus the maximum column MPL backscatter coefficient within 5-minute intervals observed on June 6, 2018. A clear separation is found between the samples with a backscattering of less than 250 km⁻¹sr⁻¹ and those above. MPL periods with backscattering greater than 250 km⁻¹sr⁻¹ show a large spread in corresponding E_z values. However, when the maximum MPL backscattering coefficient falls below 250 km⁻¹sr⁻¹, a clear grouping of E_z measurements is present in the range of -50 to -125 V/m. This range of values is within the known fair-weather range for this time of year.

Figure 8b shows the 5-minute binned maximum column MPL backscatter coefficient versus the standard deviation of each 5-minute period of the vertical electric field (E_z). Again, with a backscattering of less than 250 km⁻¹sr⁻¹, a clear separation of standard deviation values is present. When aerosol or clouds are present with a backscattering coefficient greater than 250 km⁻¹sr⁻¹, E_z values tend to have larger variations. With the presence of very little backscattering a grouping of 5-minute averaged standard deviation values of less than 20 V/m is present, indicating a relative stable electric field.

3.3.8 Case Study Composite of Absolute Value and Standard Deviation Determination of Fair-Weather

Figure 9 shows the relationship between the MPL backscattering and the E_Z in a 10-case composite. All cases are selected in 2018, and include: April 9th, April 10th, May 3rd, May 10th, May 30th, August 22nd, September 9th, October 14th, October 15th, and December 18th. All cases have relatively long (>2 hour) periods of low Lidar backscattering (<250 km⁻¹sr⁻¹) which is extremely rare for the NSA region. Figure 9a shows a scatterplot of the 5-minuted averaged electric field (E_z) versus the simultaneous 5-minute standard deviation of the electric field (E_z). Green markers represent 5-minute periods of time determined to be fair-weather by the MPL lidar, with maximum reflectance values of less than 150 km⁻¹sr⁻¹ in the vertical column. Red markers indicate 5-minute periods of time determined to be non-fair-weather by the MPL lidar with maximum reflectance values of greater than 150 km⁻¹sr⁻¹ in the vertical column. Figure 9b zooms in on the lower magnitude electric field values. A clear separation between MPL determined fair-weather and non-fair-weather is present in the composite, with 5- minute averaged fair-weather occurring in the vertical electric field range of -50 to -350 V/m with simultaneous standard deviations of less than approximately 25 V/m.

Utilizing this Lidar assisted composite, a simple definition of fair-weather can be created using only the E_z measurements themselves, requiring no use of supplemental instruments such as radars or lidars. This definition is determined to be a 5-minute averaged absolute measurement of the electric field in the range of -50 V/m to -350 V/m, with a simultaneous standard deviation of less than 25 V/m. This includes only E_z measurements in the known fair-weather range that are very stable. This allows for the simultaneous comparison to other electric field measurement sites without lidar observations. This stringent definition includes only the strictest fair-weather

and most stable values to be included, in order to assure as many local influences are removed as possible.

Nicoll et al., [2019], introduces the Global Coordination of Atmospheric Electricity
Measurements (GloCAEM) dataset, which includes 17 locations worldwide. In the case of this
dataset, meteorological data is only available at some of the measurement sites, making "True"
fair-weather conditions difficult to explicitly identify [Nicoll et al., 2019]. This dataset utilizes
"non-disturbed" electric field values defined as the inner 80% of the electric field distribution.

Both the method outlined above in this study, as well as the GloCAEM method attempt to
remove outliers of the electric field caused by many events such as precipitation, lightning,
aerosols, blowing snow, etc. However, results of this study show that there are indeed instances
of electric field measurements inside the 80% normal distribution that have significantly large
standard deviations that could be still influenced by local disturbances.

3.3.9 Variability of Fair-Weather at Several Timescales at Multiple Sites: Diurnal Variability

Figure 10 applies the fair-weather definition developed in Figures 8 and 9, now represented as the potential gradient, to two separate sites (Barrow, AK and Corpus Christi, TX) for the entire year of 2018. Figure 10a shows the comparison in two separate months, May (red) in the warm season, and October (blue) in the cold season. The solid lines represent the Barrow, AK diurnal variability, and the dashed lines represent the Corpus Christi, TX diurnal cycle. All data is binned hourly. A very similar qualitative agreement is observed between the simultaneous diurnal variability recorded at the two sites. Corpus Christi, which has far more fair-weather samples, appears to be much smoother, but in general both sites follow a very analogous diurnal maxima and minima in the observed fair-weather potential gradient. Both sites recorded absolute electric field measurements in the range reported by the Carnegie cruises. Due to slight

V/m is present between the two sites, with Corpus Christi recording consistently larger potential gradient values. However, this difference falls within the standard measurement error range of the CS110 instrument (+/- 5% +8 V/m).

Several other factors including time periods of snow coverage in Barrow, and nearly never freezing land in Corpus Christi, could lead to differences in the measured E_z, due to conductivity differences caused by the different rate of radon gas release [*Baumgaertner et al.*, 201]. In addition, non-electrified clouds at both measurement locations could have different local effects on the electric fields, which have been shown to significantly influence the current density in the past [*Baumgaertner et al.*, 2014]. Another potential cause of observed deviation in the E_z between the Corpus Christi, TX and Barrow, AK sites is aurora events. Magnetospheric perturbation is known to significantly affect the high latitude region of Barrow (71.3°N), and could cause differences in the measured fair-weather E_z values, when compared to the subtropical Corpus Christi (27.7°N) location. A more detailed analysis of this effect is needed in the future.

It should be pointed out that the typical measurement recorded at the Corpus Christi site during fair-weather is between 0 V/m and -300 V/m, with the majority of measurements recorded between -100 V/m and -200 V/m. Applying the fair-weather definition determined in Figures 8 and 9, includes these values, and insures that only the most stringent fair-weather conditions are included from Corpus Christi, which has more frequent fair-weather time periods than Barrow.

Figure 10b shows the yearly averaged fair-weather diurnal cycle for the entire year of 2018. All three of the typical convective chimney regions are displayed in both of the diurnal

curves; 7-10 UTC from the Maritime Continent, 12-15 from Africa, and 18-22 from the Americas. Both sites, which are separated by over 6,000 km, observe a similar diurnal pattern. This indicates the truly global nature of the system when small periods of fair-weather are composited together. Furthermore, both sites follow a very similar diurnal pattern to the Carnegie Curve, which is the known standard for the diurnal variability of the GEC on UTC time, giving further support to the findings [Whipple, 1929].

3.3.10 Minute-to-Hour Fair-Weather Variability

In order to determine how fine of detail the GEC can be observed in the simultaneous fair-weather signature in Barrow and Corpus Christi, Figure 11 shows examples of fair-weather E_z time series on the order of minutes to several hours at both sites. All panels were again averaged to 5-minute bins. As in Figure 10, in all 4 cases, a similar inter-time-step variability can be observed in the time series at two sites. Differences of up to approximately 60V/m are present between the two sites, which could be due to slight differences in calibration, instrumentation or location. Further studies are required to explain this difference in more detail. However, for the purpose of this study, the pattern is of more importance when observing the variability of the GEC. Observing very similar time series on this fine temporal resolution in the strictly defined fair-weather values, indicates even further the global nature of the system. If this is true, the variability of global storm occurrence that drives the GEC can be monitored real-time on the scale of minutes to hours, instead of longer time scale monthly and yearly composites as first noted by *Markson* [1986]. More data is ultimately needed in order to verify this claim in the future.

3.3.11 Joint Diurnal Seasonal Variability

Much of the past work in comparing the GEC to thunderstorms and global electrified cloud parameters have been conducted utilizing electric field measurements taken in the Southern Ocean [Whipple, 1929] or Antarctica [Burns et al. 2005; Burns et al., 2012; Lavigne et al., 2017]. Another goal of the OYES-NSA field campaign is to establish a long-running time series of electric field measurements in the Arctic. Figure 12 compares the joint diurnal and seasonal comparison of the mathematically selected fair weather from the two poles. The data from Barrow was taken in 2018 and the data in Vostok Station, Antarctica was collected from 1998-2004 as well as 2007-2011. [Burns et al., 2005; Burns et al., 2007; Burns et al., 2012] Although a similar spatial pattern at both sites is observed such as the phase, there are also some significant differences. The variation amplitude is larger at the Barrow site, especially in the UTC hours of 15-22 from February to October. This amplitude difference could possibly be explained by the far fewer fair-weather samples in the Arctic. This points to the increasing need to continue sampling this valuable measurement in the Arctic. A long-term comparison between the poles could help to uncover more detail about what drives the system and how better to model it.

3.4. Discussion/Summary

3.4.1 Importance of supplementary data

The use of the DOE ARM supplementary site instruments such as the Ka-band radar and the MPL lidar, allows for the better understanding of how cloud, aerosols, blowing snow and fairweather conditions appear in the electric field record on a case-by case basis.

• There is a strong response from the electric field to the presence of different types of clouds indicated by the radar reflectivity from the KAZR (Figure 3). Analyses of many other

electrified cloud cases in Barrow, AK as well as Corpus Christi, TX, confirm that leading anvils and stratiform regions can swing the electric field more negative on the order of several thousand V/m, as noted previously in *MacGorman & Rust* [1998]. Convective centers of the strongly electrified precipitation events have the opposite effect, driving the electric field highly positive. This magnitude varies, but is typically larger than the anvils and stratiform regions, with electric fields in the tens of kV/m observed.

- It is clear that the MPL observations help to link the relatively smaller-scale deviations in the measured E_z to small aerosol particles near to the surface (bottom 0.5 km), and not from electrified clouds or falling precipitation (Figure 4).
- The two vertically separated CS110s are able to detect the wind influence on the vertical electric field. The differences between 5-m and 2-m electric field mills is greater in the cold season (October-May) than the warm season (June-September). This is likely due to the presence of snow and ice/snow on the ground, which is easily sent aloft in even relatively low wind conditions (2 m/s). The particles blown in the air under 2-5 m/s wind tend to cause hazy conditions, as also noted by the local ground station. However, when wind increases to above 8 m/s in the cold season, it no longer creates these hazy conditions, and is more likely to cause blowing snow events, and deviates the two instruments from 1000 to +1000 V/m apart from each other.

3.4.2 Fair-Weather Analysis

Utilizing the backscattering signal from the MPL, a clear separation of electric field values and standard deviations is present in Figure 8. During periods of low column reflectance of approximately less than 200-250 km⁻¹sr⁻¹, a grouping of very stable electric field measurements in the known range of fair-weather is clearly observed. This is corroborated by the case study shown

in Figure 5, observing a very stable electric field of approximately -175V/m to -200 V/m during a period of virtually no surface backscattering or cloud activity. Although a 10-case composite is not ideal in determining the standard for a fair-weather definition, it provides a simple way of separating non-stable electric field periods (large standard deviations), as well as values that are known to fall outside the typical fair-weather range. Using this definition, similar patterns are found in the fair-weather fields on the time scales of yearly, monthly, minute to hourly averaged diurnal variability. These results corroborate past research stating the global nature of the system, at more refined timescales than previously explored. The consistent offset between the Corpus Christi, TX and Barrow, AK sites, with Barrow being consistently more negative but following the very similar temporal pattern, gives further support that both sites are encountering a very similar global contribution of electrified clouds and thunderstorms with slightly different calibrations.

3.4.3 Implications for Global Electrified Cloud Monitoring

With the temporal consistency between the fair-weather electric fields at multiple sites, it allows for the next logical step to verify if this variability is indeed driven by instantaneous electrified clouds and thunderstorms around the globe. Past work has verified that using longer term composites (multiple years), electrified precipitation feature parameters such as thunderstorm rainfall, flash rate, and volume 30 dBZ in the mixed phase region correlate very well on the time scales of diurnal, seasonal and interannual to the measured fair-weather electric field [Liu et al., 2010; Lavigne et al., 2017]. With this connection, it seems plausible to start to look at the connection between the ground-based fair-weather electric field variability and the variability of global storms as well as other fine scale measurements at much smaller time scales. With the results shown in Figure 11, it seems plausible that the GEC can be detected

simultaneously at multiple sites both encountering fair-weather without the need for averaging many smaller time periods together, as is the case in most classical diurnal depictions of the GEC. This, alongside improvements in satellite monitoring of precipitation such as the Integrated Multi-satellite Retrievals (IMERG), with near real-time global precipitation, allows for the possibility of understanding to what ability and at which timescales the GEC can monitor global electrified precipitation systems that act as its battery.

In addition to the valuable GEC measurements at the NSA site as well as other sites around the globe to monitor the contribution of electrified clouds and thunderstorms, the local electric field measurements in the Arctic may also allow for the unique opportunity to observe the effects of warming temperatures on the electrification of clouds and precipitation events in the region. A recent study observed that air temperatures in the Arctic have increased 2.7° C (4.9° F) over the past five decades [Box et al., 2019]. This rapid warming has likely influenced the types of clouds and precipitation systems in the region. During the first two full summer seasons (2018 & 2019) of the OYESNSA field campaign, the region has observed more than 10-events each year with at least +2,000 V/m electric fields, which are considered to be from electrically active clouds. A longer-term measurement of the electric field is needed to better understand the regions response to such rapid warming. With electrified shower clouds thought to precede thunderstorm activity, the preliminary results show that the region could observe significantly more electrified clouds if the current trends continue.

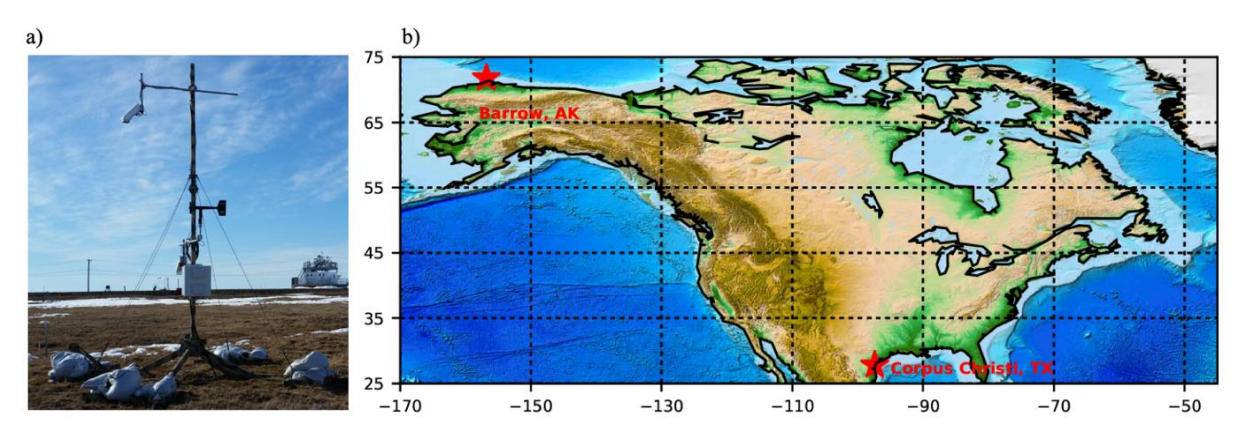


Figure 3.1: a) the instrumentation setup in Barrow, Alaska, including two CS-110 electric field meters, and one RM-Young Alpine anemometer. b) The geographical locations of the two electric field measurement sites. The distance 6,015 km apart.

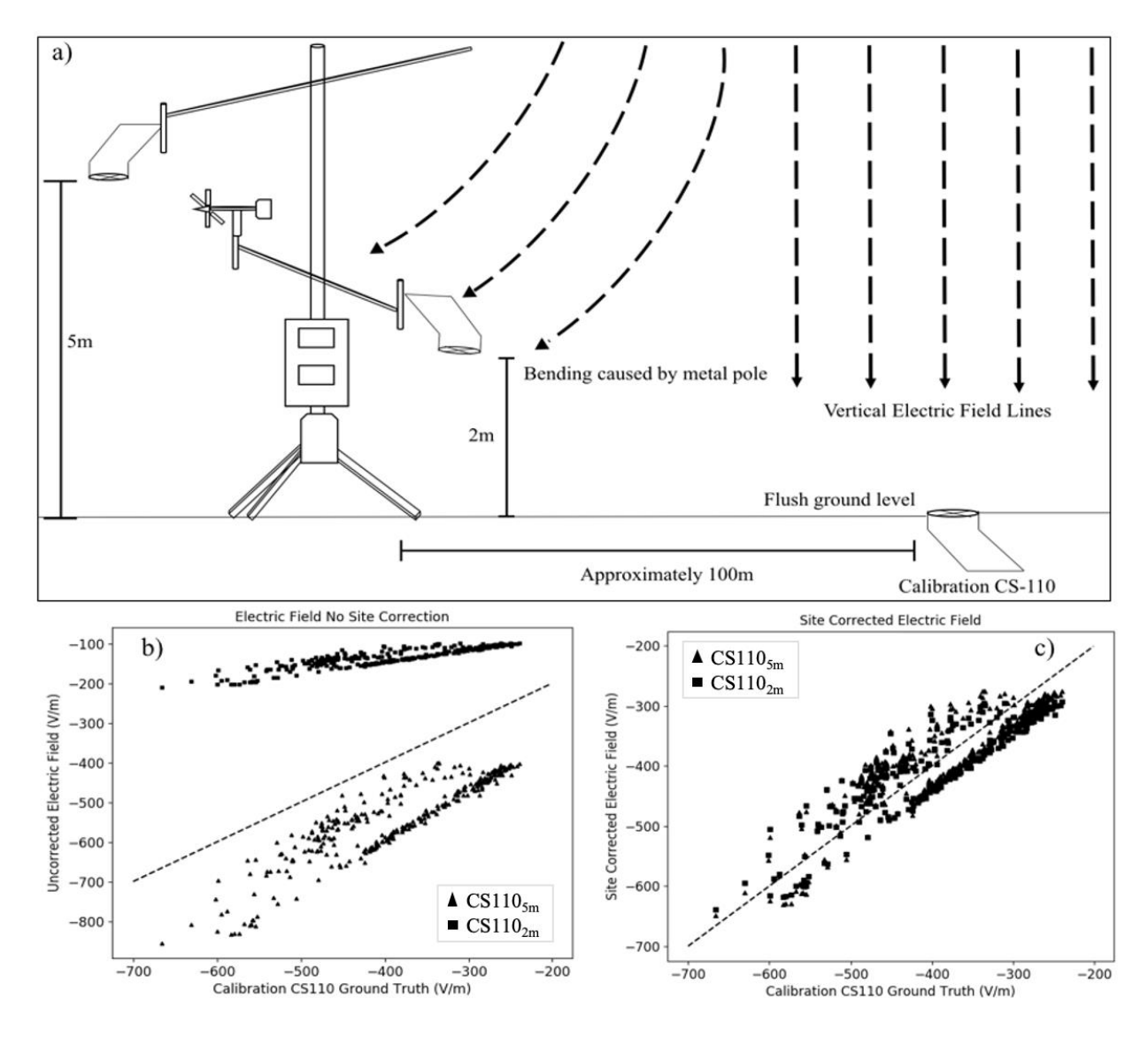


Figure 3.2: a) Schematic diagram of the vertical electric field calibration process, accounting for the influence of the metal setup and elevation. b) the simultaneous uncalibrated scatter between the $CS110_{5m}$ and $CS110_{2m}$ against the ground truth electric field instrument. c) displays the site corrected scatter of the $2\ CS110$'s versus the simultaneous ground truth. The dashed line shows the perfect one-one correlation. The calibration factor for the CS110-2 is a slope of 0.823 and intercept of 54.9, while the factor for the CS110-3 is a slope of 3.121 and an intercept of 16.69. Calibration took place over the course of approximately a 10-day period from June 13^{th} , 2017 until June 23^{rd} , 2017.

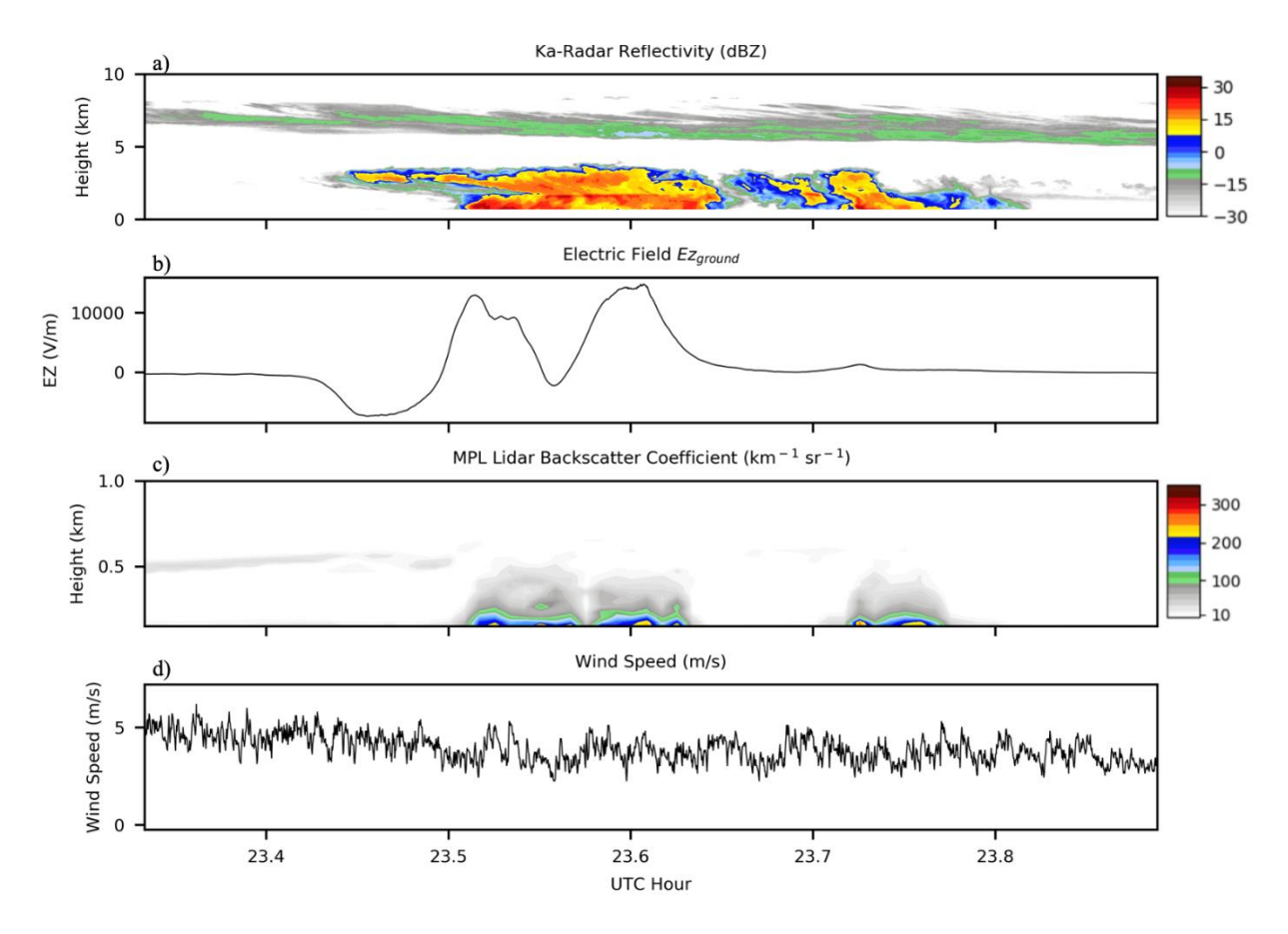


Figure 3.3: A case of an intense storm electric field event in Barrow, Alaska on July 3, 2017. Panel a) displays the vertically pointing Ka-band radar reflectivity, b) the calibrated vertical electric field measurement at ground surface at a sampling rate of 1 Hz, c) the vertically pointing Micro pulse Lidar backscattering signature (km⁻¹sr⁻¹), and d) the wind speed (m/s) for the day measured at 1 Hz.

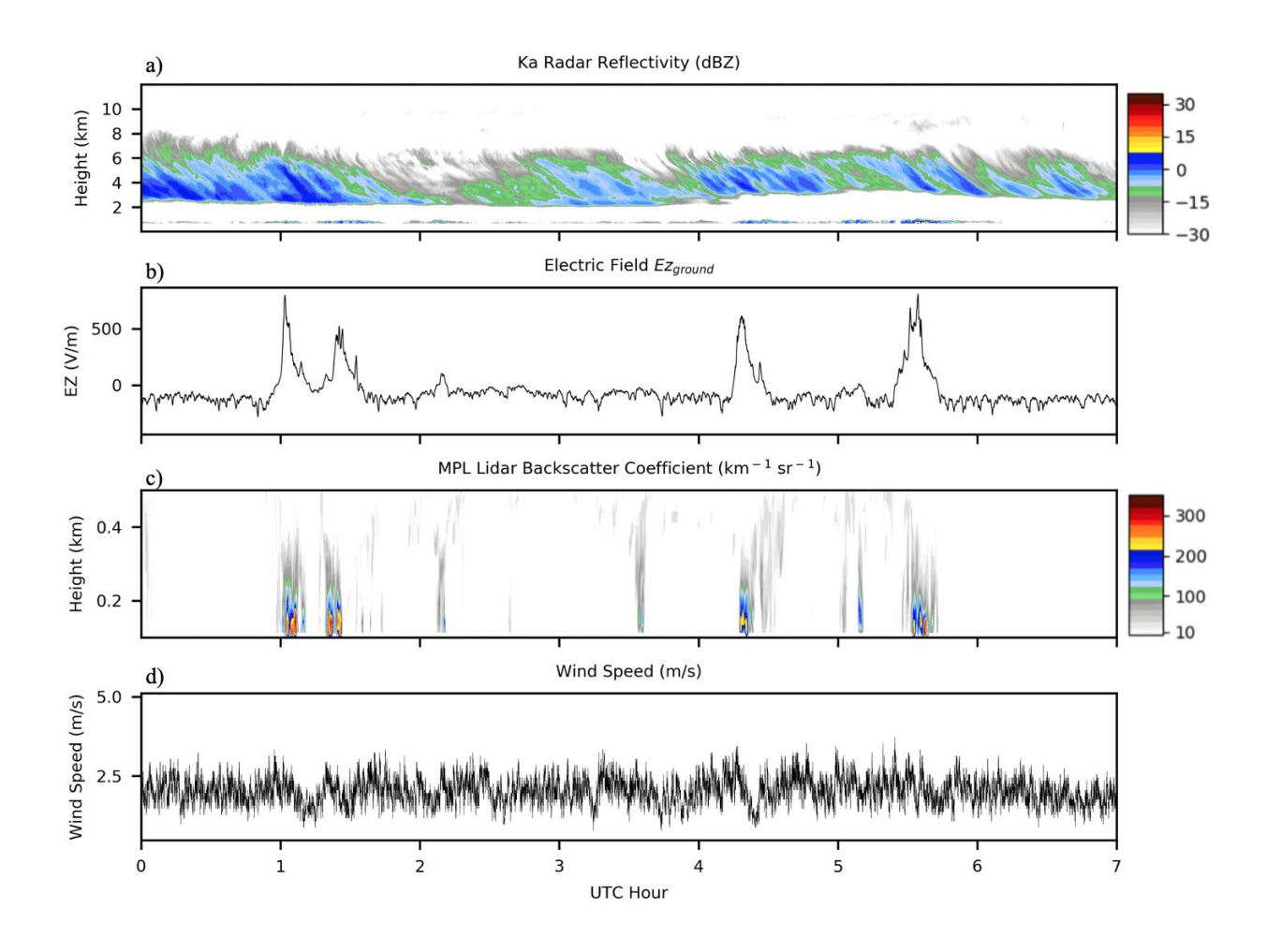


Figure 3.4: Same as figure 3, except for a Lidar dominated electric field signature case study recorded on August 12, 2017.

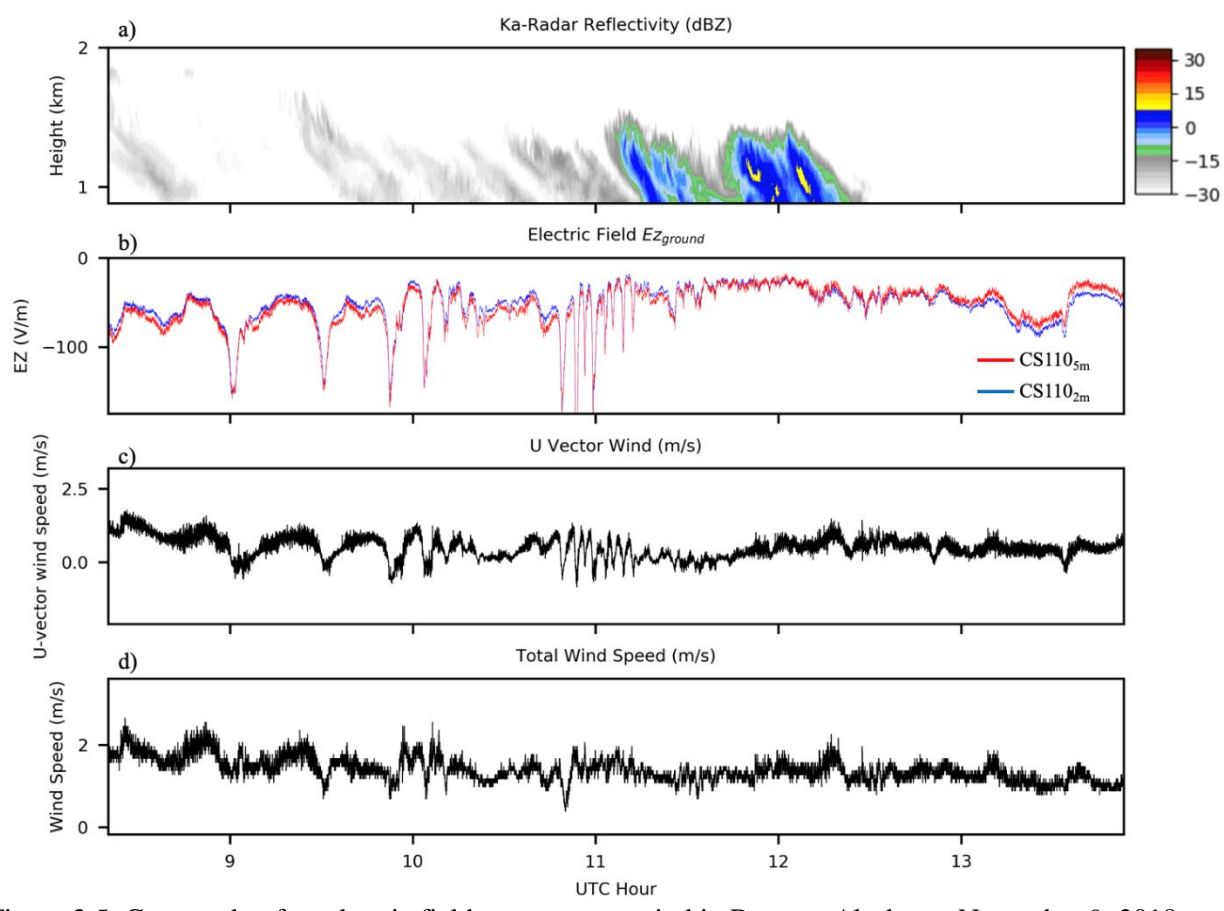
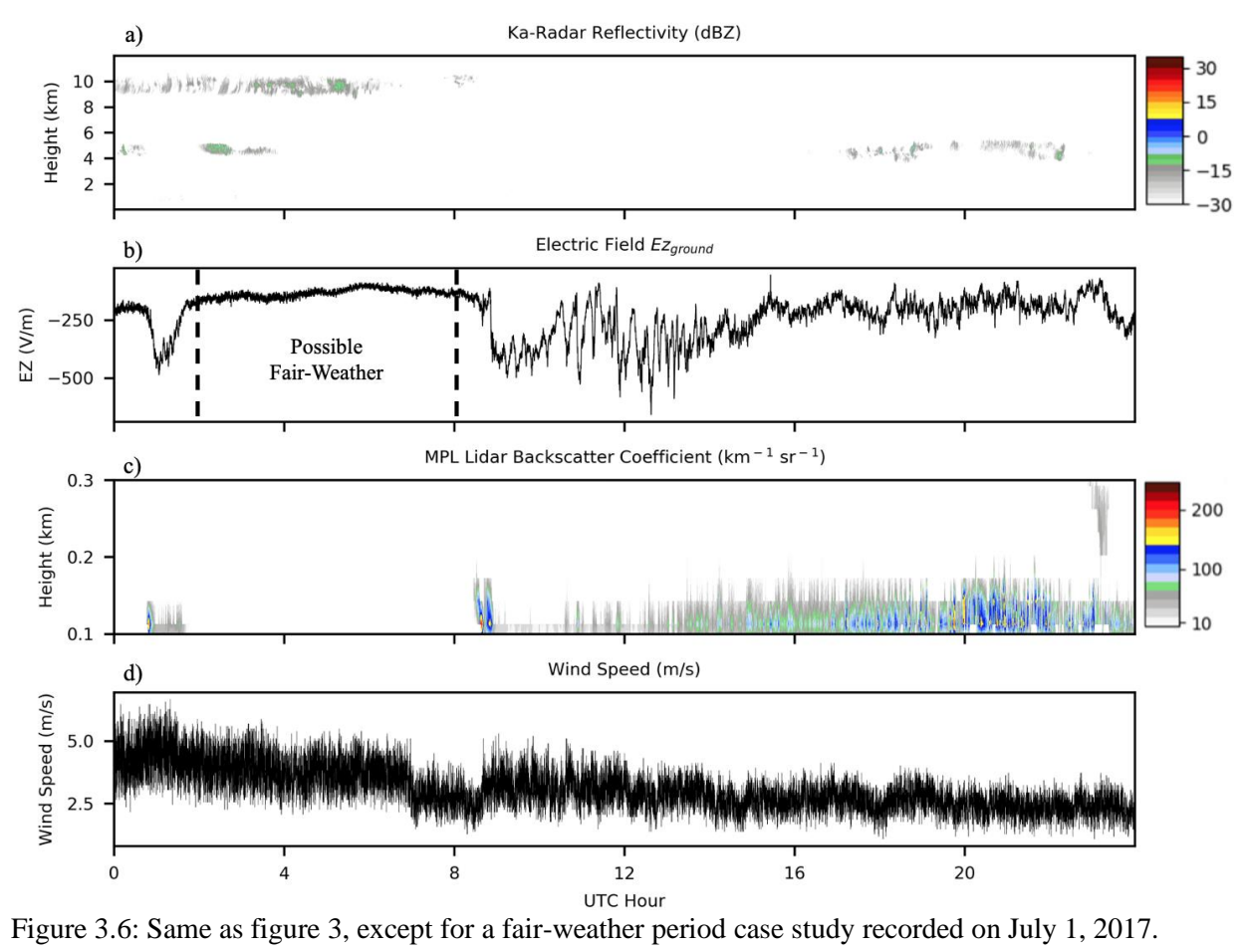


Figure 3.5: Case study of an electric field event versus wind in Barrow, Alaska on November 9, 2018. Panel a) displays the vertically pointing Ka-band radar reflectivity, b) the vertical electric field measurement at a sampling rate of 1 Hz (red = bottom CS110 and blue = top CS110), c) the U-vector wind speed (m/s), and d) the total wind speed (m/s) for the day measured at 1 Hz.



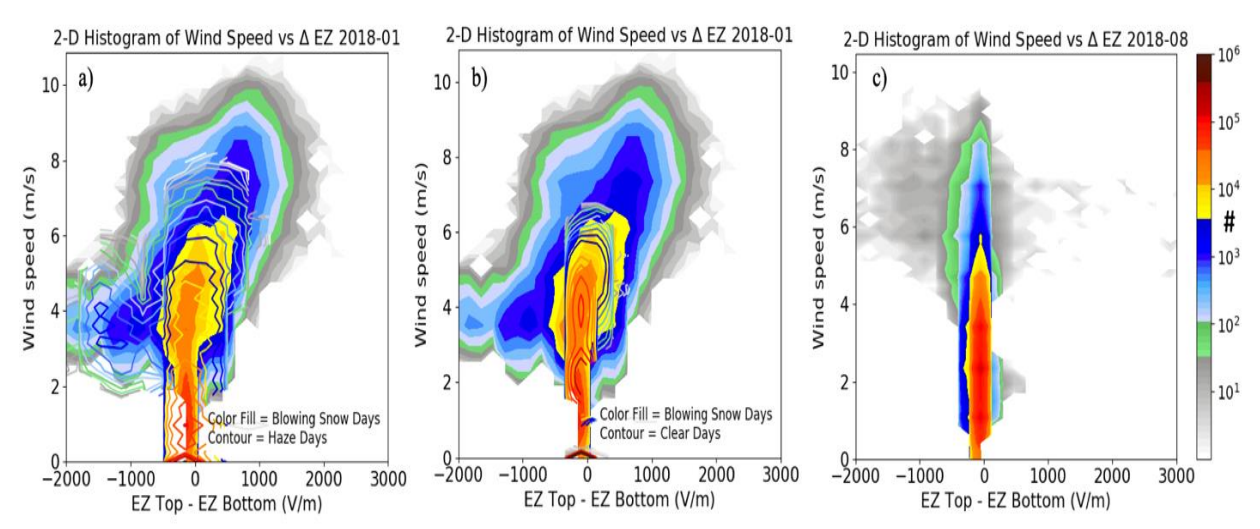


Figure 3.7: Histogram of the a) difference between the top and bottom CS110 electric field meters versus the wind speed during January blowing snow days (color filled), and January non-blowing snow days with haze (contour). B) Difference between the top and bottom CS110 electric field meters versus the wind speed during January blowing snow days (color filled), and January non-blowing snow days without haze (contour). C) Difference between the top and bottom CS110 electric field meters versus the wind speed during August all sampled data. Blowing snow and haze days were determined using the National Oceanic and Atmospheric Administration (NOAA) Global Surface Summary of the Day (GSSOD) dataset

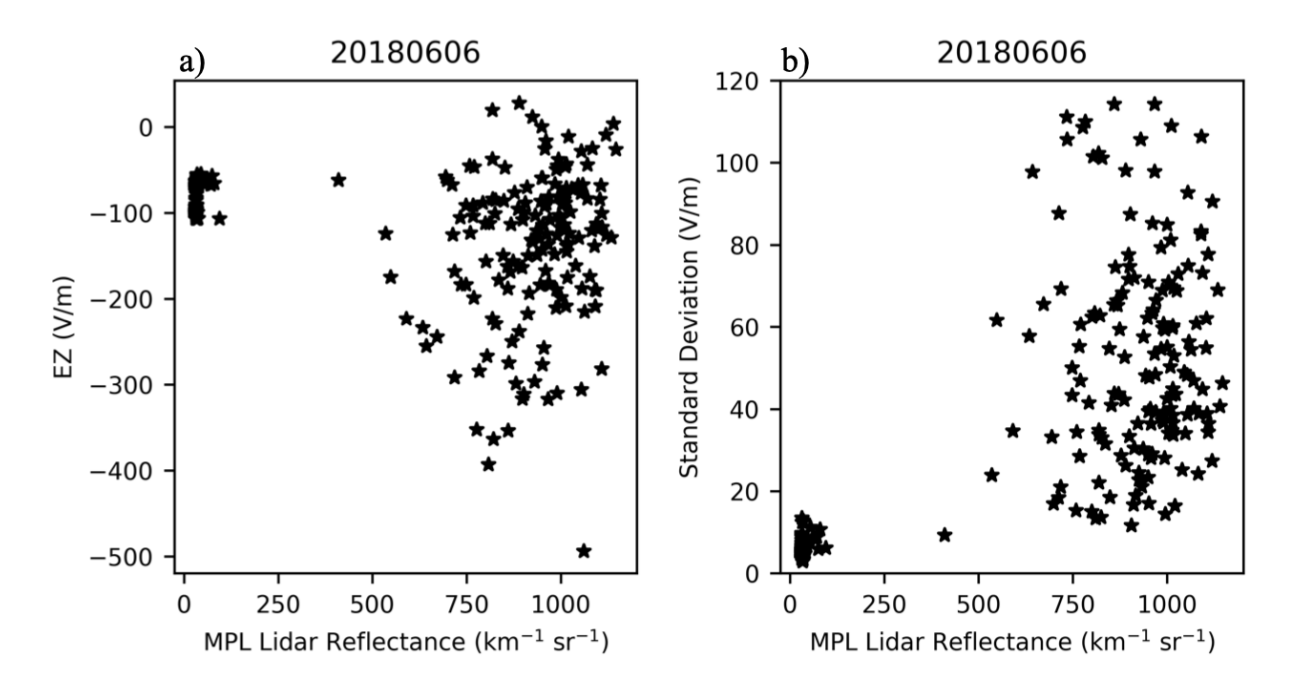


Figure 3.8: Example scatterplots of 5-minute mean electric-field (V/m) versus the simultaneous 5-minute maximum backscattering (km⁻¹sr⁻¹) overserved by the Micro pulse Lidar (panel a), and the standard deviation of the 5-minute averaged electric-field (V/m) versus the simultaneous 5-minute maximum backscattering (km⁻¹sr⁻¹) observed by the Micro pulse Lidar (panel b).

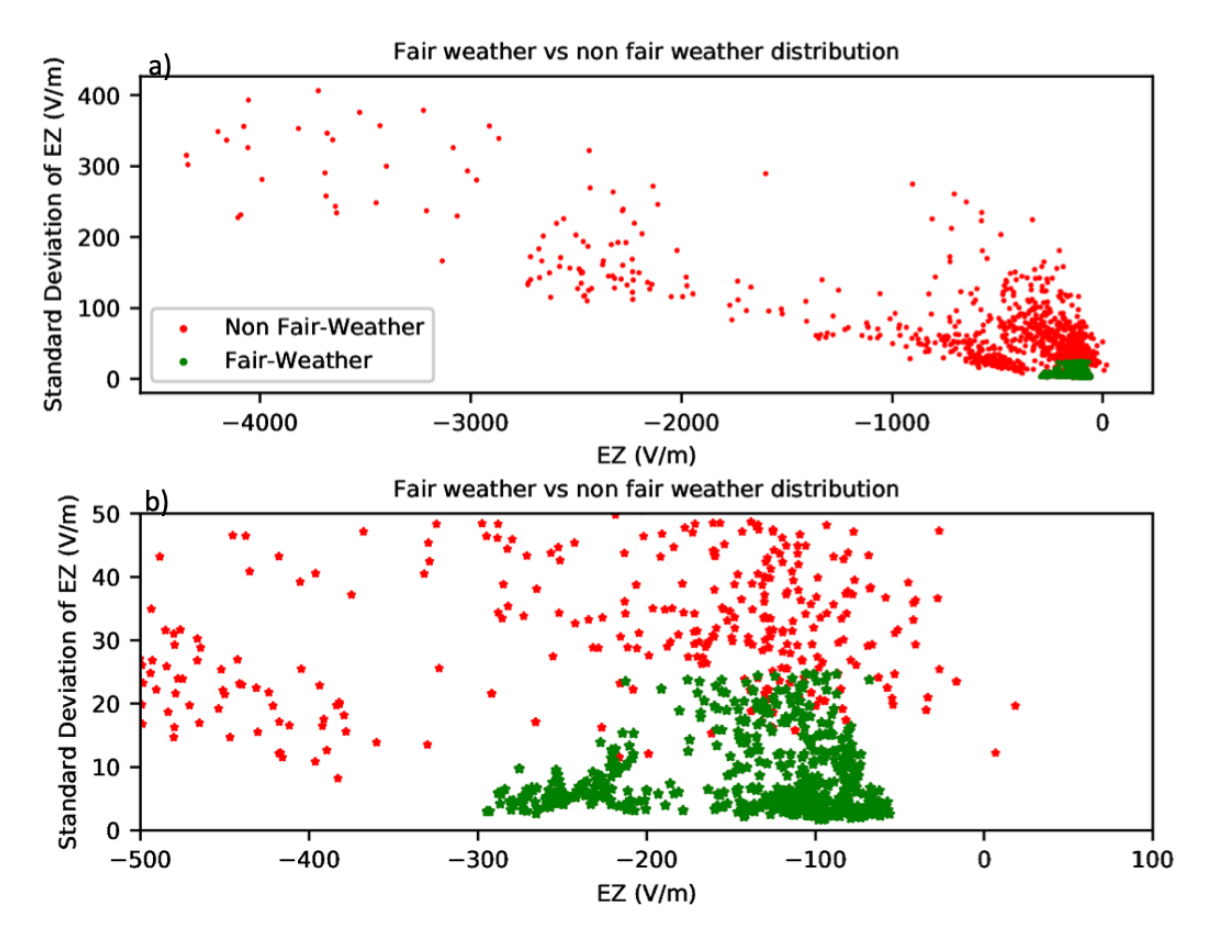


Figure 3.9: a) Scatter of 5-minute averaged vertical electric field (V/m) measurements versus the 5-minute averaged standard deviation of the electric field (V/m). Green colors represent time periods with a Lidar reflectance of less than $150~\rm km^{-1}sr^{-1}$ and red colored stars indicate time periods with a larger Lidar reflectance than $150~\rm km^{-1}sr^{-1}$. B) Same as panel a, but zoomed into the fair-weather region. Fair weather time periods were selected to have at least 30 consecutive minutes of less than 25 V/m standard deviation of the vertical electric field. These data were taken in April 9th, April 10^{th} , May 3^{rd} , May 10^{th} , May 30^{th} , August 22^{nd} , September 9^{th} , October 14^{th} , October 15^{th} , and December 18^{th} , all in 2018.

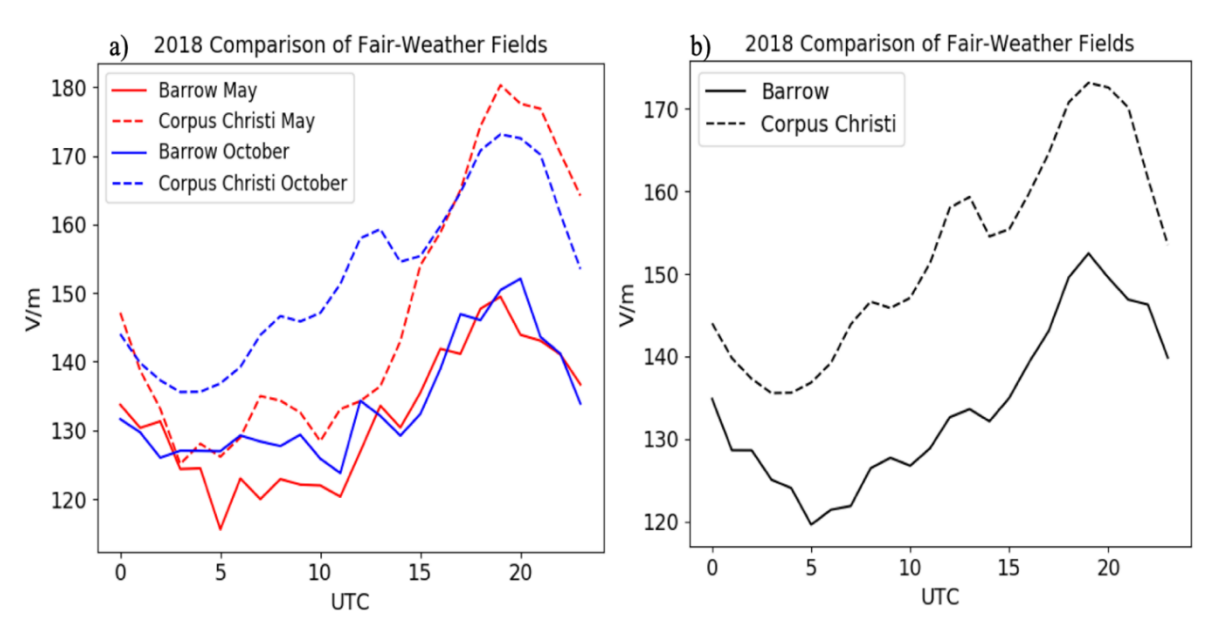


Figure 3.10: a) Simultaneous diurnal variations of the mathematically selected fair-weather values at Corpus Christi (blue) and Barrow (red) for the months of May (solid) and October (dashed). Panel b) shows the absolute value of the yearly averaged diurnal variation using the mathematically selected fair-weather values at Corpus Christi (blue) and Barrow (red) for 2018.

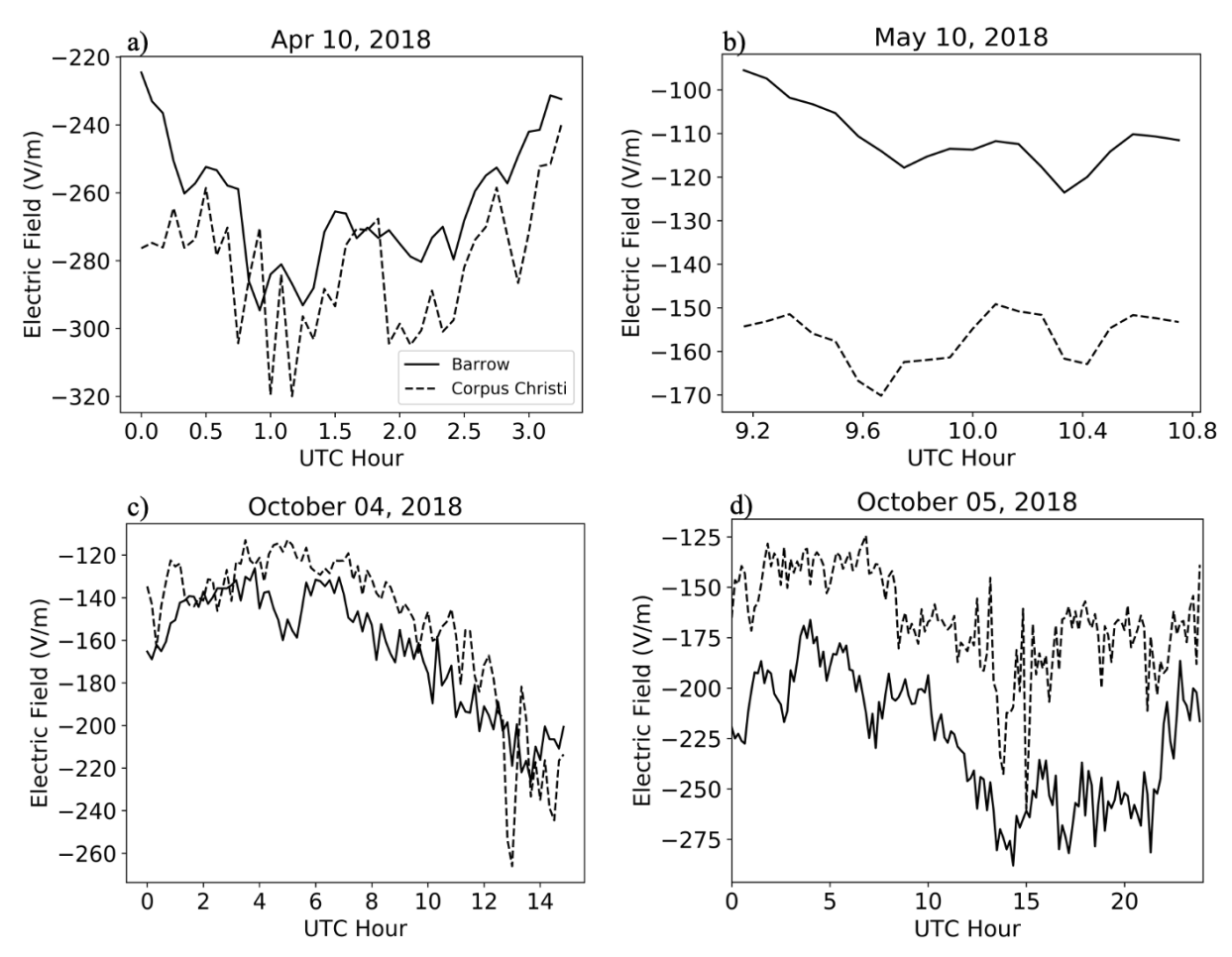


Figure 3.11: Comparison of simultaneous mathematically selected fair-weather from Corpus Christi (dashed) and Barrow (solid). All panels use a 5-minute averaged electric field. All data from Barrow is displayed using the top instrument (CS110-2).

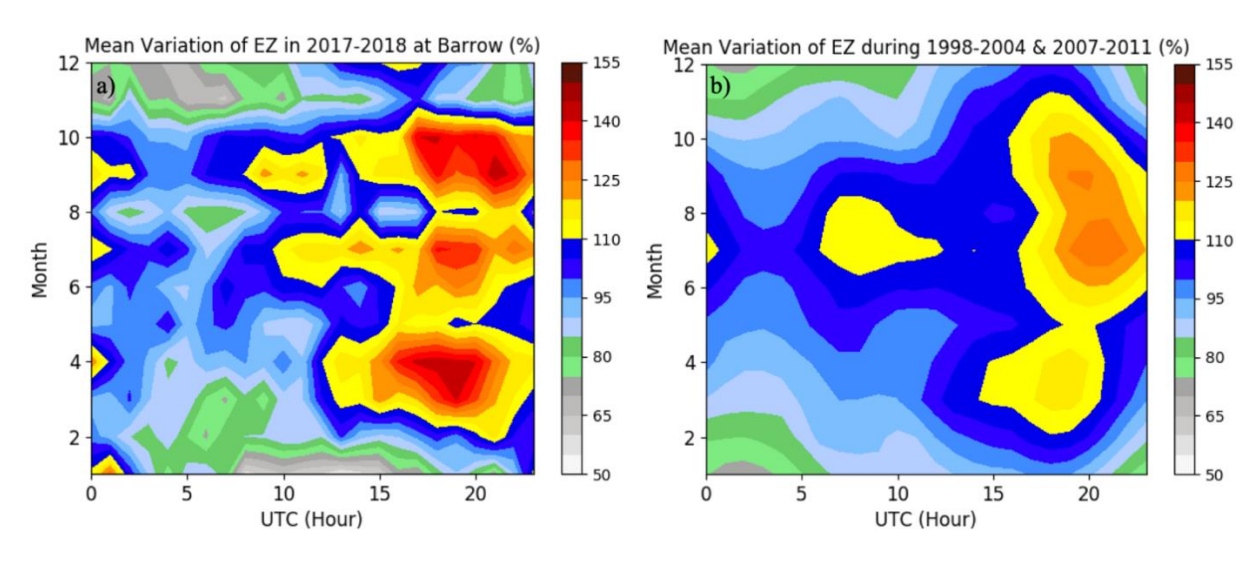


Figure 3.12: Joint diurnal and seasonal histograms of the mathematically selected fair-weather electric field in a) Barrow and b) Vostok Station Antarctica. All data is collected at a sampling rate of 1 Hz and binned into 1-hourly and 1-monthly bins.

CHAPTER IV: RELATIONSHIPS AMONG DIURNAL VARIATIONS OF POLAR NIGHT CLOUD, PRECIPITATION, SURFACE TEMPERATURES, AND THE FAIR-WEATHER RETURN CURRENT OF THE GLOBAL ELECTRIC CIRCUIT (GEC)

4.1 Introduction

4.1.1 The Global Electric Circuit (GEC) of the Atmosphere.

The Global Electric Circuit (GEC) of the atmosphere is a naturally occurring phenomenon in which the Earth's atmosphere acts as a leaky capacitor between the Ionosphere and the Earth's surface [Roble, 1986; Markson, 2007; Williams, 2009; Williams & Mareev, 2014]. Primarily due to the constant presence of thunderstorms and electrified clouds around the globe, the leaky capacitor is continually recharged by the upward storm current produced above thunderstorms and electrified clouds [Siingh et al., 2007]. The balance between the fair-weather return current which drains the circuit, and the input from the upward storm current creates the stable Earth's electrical system known as the GEC.

Surface measurements of the vertical electric field (E_z) of the atmosphere have been conducted for more than one hundred years. [Wilson, 1909; Wilson, 1921; Wilson, 1924]. The most notable variability observed in the E_z is the evident diurnal cycle in UTC time observed at multiple locations around the globe in the absence of significant clouds, aerosols, and other local influences [Harrison, 2013; Peterson et al., 2017; Nicoll et al., 2019]. Whipple [1929], was the first to quantitively tie this diurnal variability of the E_z to the diurnal variability of global thunderstorm area in UTC time. Primarily driven by the differing numbers of thunderstorms and electrified clouds occurring globally in UTC time, the diurnal minimum in the E_z at 3:00 UTC, and the maximum at 19:00 UTC has been proven to be very consistent at many sites around the globe measuring fair-weather conditions, and is known as the Carnegie Curve [Harrison, 2013].

With the increased data availability of the satellite era, a clearer understanding of the amount and distribution global precipitation events and lightning activity became possible in comparison to the crude thunderstorm area gathered by ground stations in the early 20th century. In the past several decades, more recent studies have now provided further evidence of the connection between the GEC and thunderstorm and electrified cloud activity on the diurnal [Williams and Heckman, 1993; Williams, 1994; Adlerman and Williams, 1996; Mach et al., 2011; Blakeslee et al., 2014], seasonal [Burns et al., 2012; Blakeslee et al., 2014; Lavigne et al., 2017; Lucas et al., 2017;], interannual [Harrison, 2004; Burns & Frank-Kamenetsky, 2005; Markson, 2007] and even possibly climate [Williams, 2005] timescales. The strongest magnitude GEC time periods have been observed to occur between June and October during the hours of 18-22 UTC, corresponding to the time-period of maximum global flash rates, as well as precipitation from thunderstorms and Electrified Shower Clouds (ESCs) [Liu et al., 2010; Mach et al., 2011; Lavigne et al., 2017]. El Nino Southern Oscillation (ENSO) natural climate variability signals have also been observed in the GEC timeseries, indicating the potential ability of utilizing the variability of the GEC to observe changes in the climate system [Harrison et al., 2011; Lavigne et al., 2017; Slyunyaev et al., 2021].

4.1.2 Possible Impacts of the GEC Fair-Weather Return Current

As a clearer understanding of the battery that drives the GEC system becomes available, an interesting next question is how the system itself may influence the surrounding environment. A breakthrough study conducted by *Harrison and Ambaum* [2013], observed that in both the high latitude regions of the northern and southern hemisphere, a consistent diurnal variability of the cloud base height was present during the polar night time-period at each site. In both regions, persistent layered stratocumulus clouds are present for much of the polar night duration. The

diurnal variability of this cloud base layer is consistent with the diurnal variability of the GEC, with the lowest cloud base heights occurring between 3-6 UTC, and the maximum cloud base heights occurring between 19-20 UTC [Harrison and Ambaum, 2013]. The study also noted an inverse relationship between cloud base height and temperature anomalies with cooler air temperatures during periods with higher cloud base heights.

Nicoll and Harrison [2016], utilized specially instrumented radiosondes to measure the charge density and conductivity of the persistent layered stratocumulus clouds at Reading University in the United Kingdom. Results showed negative space-charge density at the cloud base, and positive space-charge density at the cloud top. The study showed that categorically all persistent layered clouds can be expected to contain charge at their cloud tops and bases due to the fair-weather return current of the GEC. However, it is also likely that a combination of the background electrical condition driven by the GEC, and cloud thermodynamics contribute to the magnitude of the charging of the cloud base and top [Nicoll and Harrison, 2016].

The presence of the fair-weather return current and the subsequent charging of the cloud top and bottom due to the conductivity difference between clear and cloudy air, is thought to potentially influence cloud microphysical processes such as droplet-droplet interactions, aerosoldroplet interactions as well as droplet activation [Khain et al., 2004; Tinsley et al., 2000; Harrison & Ambaum 2008; Harrison, 2015, Nicoll & Harrison, 2016]. The most likely effect is on the size and population of particles inside the charged layered clouds. This has implications for the radiation budget of the clouds, as well as the potential for increased precipitation activation [Harrison et al., 2015].

4.1.3 Multi-Year Electric Field Study-North Slope of Alaska (MYES-NSA) Field Campaign In June 2017, the Multi-Year Electric Field Study-North Slope of Alaska (MYES-NSA) field campaign was established in Barrow, Alaska at the Department of Energy Atmospheric Radiation Measurement (DOE ARM) site. The unique site provides the unprecedented ability to observe cloud, aerosol, and precipitation properties alongside surface E_z measurements [*Lavigne et al.*, 2021]. The field campaign location includes an upward pointing Ka-Band Radar, an upward pointing Micro Pulse Lidar (MPL), a ceilometer, two electric field mills, as well as numerous supplemental meteorological instrumentation

[https://www.arm.gov/capabilities/observatories/nsa]. With the increased information regarding the cloud and aerosol properties of the layered clouds above the electric field meters (within 100m), it is conceivably possible to further understand the effects of the fair-weather return current magnitude on the properties of persistent layered clouds in the Arctic.

This manuscript aims to answer the following questions:

- Can the noteworthy relationship between the diurnal cycle of the fair-weather electric field and the polar night cloud base height, originally reported by *Harrison & Ambaum*, [2013], be replicated in Barrow, AK?
- With the additional data available, are any other cloud or precipitation properties of longlived stratified clouds observed to be modulated on a time scale similar to that of the GEC?
- How do the long-lived stratified clouds influence the diurnal change in surface temperature during the polar night in Barrow, AK?

4.2 Data and Methodology

The DOE ARM site located in the North Slope of Alaska (NSA) (71.2906° N, 156.7886° W) is a fully instrumented government facility which emphasizes on collecting data related to cloud and radiative processes at high latitudes [https://www.arm.gov/]. The NSA location provides a unique opportunity to study the cloud and radiative properties in the Arctic, a location which is difficult to permanently maintain such a suit of instruments.

4.2.1 Ka-Zenith Radar (KAZR)

The site maintains a Ka-Band Zenith Radar (KAZR), which is a zenith pointing doppler radar that operates at the frequency of approximately 35 GHz. The KAZR has been in operation since 2011 and operates with a vertical resolution of 30 m from the near surface to 20 km, sampling every 3.5 seconds. The KAZR radar can measure the three Doppler moments; reflectivity, vertical velocity, and spectral width.

4.2.2 Micro Pulse Lidar (MPL)

The NSA facility also maintains a Micro Pulse Lidar (MPL), which operates at a wavelength of 532 nm and uses the same principle as a radar, measuring the backscattered energy back to the transmitter. The MPL has been in permanent operation at the NSA facility since 1998, and samples every 3 s with a vertical resolution of 30 m from the near surface to 20 km. The primary function of the MPL is to measure the aerosol backscattered radiation, total column backscatter (km⁻¹*sr⁻¹), as well as deriving the cloud base height.

4.2.3 Cloud Ceilometer

A ceilometer is also utilized to determine the cloud base height and has the ability to detect three cloud layers simultaneously. The ceilometer uses near infrared pulses and has a maximum vertical range of 7.7 km. With the ability of detecting the cloud top and bottom, a

simple subtraction is utilized to determine the cloud thickness of the first layer. The backscatter radiation can also be measured with the ceilometer. The ceilometer has been maintained on the NSA since 1997.

4.2.4 Laser Precipitation Monitor (LPM)

The Laser Precipitation monitor is an eye safe Distrometer that measures the drop size spectra and fall velocity of hydrometeors during precipitation events. The laser precipitation monitor measures the hydrometeor size distribution of precipitation events. The instrument can also detect the visibility, reflectivity at the surface, and the surface temperature, and has been in operation at the NSA site since April 2017.

4.2.5 Sky Radiometers on Stand For Downwelling Radiation (SKYRAD)

The Sky Radiometers on Stand For Downwelling Radiation (SKYRAD) is a collection of radiometers at the NSA site that measure longwave and shortwave irradiances. The SKYRAD radiometers collect data continuously and output every one-minute. Data recorded include longwave broadband downwelling irradiance, shortwave broadband diffuse downwelling irradiance, shortwave broadband direct normal irradiance, as well as cloud fraction. The suit of sky rad instruments has been operating at the NSA site since 1999.

4.2.6 Campbell Scientific Electric Field Meter (CS110)

Two Campbell Scientific CS110s have been deployed at the NSA site since 2017 in conjunction with the Multi Year Electric field Study at Northern Slope Alaska (MYES-NSA) field campaign [Lavigne et al. 2021]. The CS110s sample at a rate of 1 Hz, with a maximum measurement range of +/-20,000 V/m. A slight vertical profile is present between the two CS110's, with one instrument mounted at 2 m and the other at 5 m above the surface. Both CS110s have been calibrated to the ground level with the use of a 3rd ground flush upward facing

CS110 [Chmielewski, 2013]. This also calibrates out the bending of the vertical field lines caused by the surrounding metal towers and mounting materials (see Lavigne et al., [2021] for more details). Both CS110s are located less than 100 m from all the other coordinating instrumentation mentioned above. Fair-weather time periods are determined using the method outlined in Lavigne et al. [2021], utilizing 5-minute time periods with an averaged standard deviation of less than 15 V/m, and mean E_Z values between -250 V/m to -50 V/m. This criterion was determined with the help of the MPL and KAZR, and largely excludes time periods with high aerosol concentrations or significant clouds.

4.2.7 Polar Night Time Period, Diurnal Averaging and Binning

The polar night occurs in Barrow, Alaska each year for 66-days between the dates of November 18th and January 22nd. With the absence of incoming solar radiation, the polar night time period acts as a unique laboratory-like setting to observe smaller magnitude diurnal variability not caused by the diurnal solar cycle. Only data from 2017-2022 occurring in the polar night time period in Barrow, Alaska is used in this analysis.

For diurnal comparison, 9 selected variables MPL and ceiliometer derived cloud base height MPL cloud thickness, MPL total column backscatter, LPM precipitation intensity and number of precipitation particles, LPM visibility, surface air temperature, SKYRAD longwave downwelling irradiance, CS110 vertical electric field) are binned in hourly averages. Simple Pearson correlation coefficients are calculated between all variables to determine statistical correlation.

4.3 Results

4.3.1 Cloud Base Height, Cloud Top Height, and Cloud Thickness Verses the Fair-Weather

Vertical Electric Field at the NSA Site

In a past study, the Cloud Base Height (CBH) was compared to the simultaneous magnitude of the fair-weather vertical electric field at high latitude sites in both the Northern (Sodankylä, Finland) and Southern (Hailey, Antarctica) Hemispheres [*Harrison & Ambaum*, 2013]. Results from both locations show a similar relationship between the two variables thousands of kilometers away when measured in the polar night time period. With the addition of another polar site measuring the electric field in Barrow, Alaska, a similar comparison between the CBH and fair-weather E_z is worthwhile to determine the global nature of this phenomena.

Figure 1a shows the diurnal variability of the measured fair-weather electric field in Barrow, Alaska (red), the CBH (solid), the cloud top height (CTH) (dashed), and the cloud thickness (dotted) measured by the MPL located at the NSA site during the polar night time period. Cloud thickness is calculated as the simple subtraction of the cloud top minus cloud base of the first layered cloud in the column measured the MPL. All timeseries are binned to 1-hourly averages and are computed as a percent deviation from the mean value during the sampled period. A similar diurnal pattern is observed in Figure 1a between all four variables, comparable to that observed in Harrison & Ambaum, [2013], with the peak in both the E_z and the CBH occurring between 16 and 19 UTC. A clear statistical positive correlation is present between the CBH and fair-weather E_z, with a Pearson correlation of 0.74 and a p-value of 4.05e⁻⁵. The diurnal magnitude is also comparable between the three cloud properties and the fair-weather E_z during the polar night. However, the cloud properties do observe slightly larger magnitudes of diurnal variation with a minimum occurring at approximately 12-14 UTC and maxima at 17-19 UTC.

Interestingly, a peak is observed in the CBH between 5-9 UTC, which is not displayed in the E_z diurnal cycle. The mismatch during this period deserves further exploration in the future.

Figure 1a also shows that when CBH, CTH, cloud thickness and the fair-weather E_z variables are directly compared, a potential diurnal propagation is observed in the diurnal maxima, with the polar night fair weather E_z peaking first at 16 UTC, the CBH peaking 1-hour later at 17 UTC, followed by the cloud thickness peaking at 17-18 UTC. This propagation could imply that the properties of the long-lived stratified clouds in the polar night may indicate that the influence of the magnitude of the E_z may take several hours to fully influence the clouds. The CBHs and CTHs tend to continue to grow in the column for approximately an hour after the E_z peaks, and the clouds continue to become thicker for approximately 2-hours after the E_z peaks. This finding warrants further investigation in the future.

Figure 1b shows the yearly-averaged diurnal variability of the measured fair-weather electric field in Barrow, Alaska (red), the CBH (solid), the cloud top height (CTH) (dashed), and the cloud thickness (dotted) measured by the ceilometer? located at the NSA site. A clear regime change is observed in comparison to the polar night time period (1a). The yearly-averaged fair-weather electric field is completely out of phase with the CBH, CTH, and thickness, with the peak in GEC occurring at 20 UTC, and the peak in CBH occurring at 5-6 UTC. This peak in CBH corresponds to the minima time-period of the GEC. This result indicates that the CBH, CTH and cloud thickness observe a similar diurnal phase and amplitude only during the polar night in Barrow, AK without the influence of incoming solar shortwave radiation.

With the unprecedented ability to observe the properties of the aerosols and clouds above the measured ground-based electric field, comes the opportunity to explore the relationship between the fair weather E_z and other properties of the long-lived stratified clouds that occur in

the polar night in Barrow, Alaska. Figure 2a shows a two-dimensional histogram of the cloud fraction observed during the polar night in Barrow Alaska by the KAZR radar. A threshold of -30 dBZ is applied to determine cloud verses no-cloud conditions. The threshold value -30 dBZ is used to be consistent with the CloudSat cloud detection sensitivity [Stephens et al., 2002]. The cloud fraction is calculated by dividing the observed number of clouds in each KAZR time and height bin, by the total number of sampled bins for each corresponding time and height. A similar diurnal pattern as previously mentioned is observed in the cloud fraction measured by the KAZR. Clouds heights tend to trend towards lower in the column from 0 UTC to approximately 5 UTC. The clouds then start to trend higher in the column exhibiting a peak around 15 UTC, corresponding to the peak in thunderstorm and electrified clouds from the African convective chimney [Williams & Satori, 2004; Mach et al., 2011] . The clouds then continue to trend higher in the column, peaking between 4-5 km between 19-22 UTC, agreeing with the peak strength period of the fair-weather Ez. Figure 2a also displays that clouds tend to occur with a larger magnitude variation of heights (possibly indicating thickness) during the early UTC hours, and peaking later between 20-22 UTC, corresponding to a similar result shown in Figure 1.

Figure 2b shows a two-dimensional histogram of cloud base counts observed by the laser ceilometer located at the NSA site. Cloud base counts were calculated by taking the cumulative number of CBH heights observed by the ceilometer observed at each time and height throughout the polar night. Results are comparable to Figure 2a and show the majority of the long-lived stratified clouds occur with a cloud base at approximately 2,000 m between 2-10 UTC. Cloud base counts increase to 2,500 to 3,000 m later in the UTC time, peaking during 19-22 UTC. This is consistent with both the diurnal fraction of cloud counts measured by the KAZR, as well as the time of maxima fair-weather E_z. The dashed black line represents the hourly-averaged mean

CBH for the entire sampled period. The corroboration of two cloud monitoring instruments, the KAZR and laser ceilometer, provide stronger evidence that the CBHs and cloud thickness during the polar night are indeed in similar phase and amplitude as the simultaneous magnitude of the fair-weather E_z which is known to be primary driven by global thunderstorm and electrified cloud activity.

Figure 3 shows the two-dimensional diurnal histogram of MPL backscatter (km⁻¹*sr⁻¹) derived aerosol event counts during the polar night in Barrow, Alaska during the years of 2017-2022. A threshold of 100 km⁻¹*sr⁻¹ was applied to determine an aerosol/no aerosol event period. Below 200 m, the aerosol fraction is very high, with a nearly uniform diurnal cycle observing significant aerosol 40% or more of the day. Above 250 m, the aerosol fraction decreases significantly to less than 0.1. Again, no significant diurnal cycle is indicated in the aerosol fraction aloft, indicating that the majority of aerosols occur in the lower 250 m and are uniform throughout the day. This indicates that the concentration of aerosol aloft at the near-surface is not in phase with the GEC, and is primarily driven by other factors, such as surface wind and anthropogenic activity.

4.3.2 Cloud Precipitation and Optical Properties Verses Vertical Fair-Weather Electric Field at the NSA Site

The supplementary suit of instrumentation at the NSA site in Barrow, Alaska, allows for further investigation into the optical and precipitation properties of polar night clouds in Barrow, and how they potentially relate to the fair-weather E_z . Figure 4a shows the diurnal cycle of the fair-weather E_z (solid) and the diurnal cycle of number of falling precipitation particles (dashed) measured at the surface with the laser precipitation distrometer. Both variables are analogous in both phase and amplitude. During periods of maxima fair weather E_z values, there tends to be

more falling precipitation particles. It is important to point out that these two variables are not measured simultaneously and are composites of the entire sampled period. For example, time periods of falling precipitation are very likely removed from the fair-weather E_z definition, therefore the time periods of falling precipitation are compared to the climatology of fair-weather in Barrow, Alaska in the lack of precipitation, clouds, aerosol, etc.

Figure 4b displays a similar diurnal pattern of total column backscatter. The sum backscatter variable (km $^{-1}*sr^{-1}$) is measured as the total accumulation of backscatter in the column observed by the ceilometer. In agreement with the number of precipitation particles, the sum backscatter displays remarkable phase agreement to the diurnal cycle of E_z . However, the sum backscatter does observe a slightly smaller diurnal magnitude.

Figure 4c shows the diurnal variation of the precipitation intensity (dashed) compared to the fair-weather E_z (solid). A much less consistent relationship is observed between the two variables in comparison to number of precipitation particles and sum backscatter to the fair-weather E_z . However, the minima and maxima in precipitation intensity do align within 1-hour with the diurnal E_z . The precipitation intensity diurnal amplitude is twice as large as the fair-weather E_z . A further investigation is needed to verify if the two parameters are indeed physically linked.

4.3.3 Relationship Between the Longwave Downwelling, Fair Weather E_z and Cloud Base Height

Figure 5 explores the relationship between the longwave downwelling irradiance emitted from the polar night clouds, and the fair-weather E_z as well as CBH. Figure 5a displays the scatter plot of the longwave downwelling from the polar night clouds and ambient air, and the fair-weather E_z . A clear statistically significant negative correlation is present with a Pearson

correlation of -0.70. There is an approximate 1 W/m drop in longwave downwelling for every increase in 5 V/m in the fair-weather E_z .

Figure 5b shows the relationship between the CBH and longwave downwelling. Again, the figure displays a robust negative relationship between the two variables. A statistically significant relationship is present with a Pearson correlation of -0.63. As the CBHs form lower in the column, there tends to be less longwave downwelling irradiance measured by the *SKYRAD*. These relationships shown in Figure 5, indicate that the amount of longwave downwelling irradiance measured at the surface is statistically related to the intensity of the fair-weather E_z, due to its effect on the long-lived stratified CBH formation in the column. Since there is no incoming solar shortwave radiation during the polar night, this variability in longwave downwelling irradiance from the clouds is more pronounced, and potentially influential on the radiation budget of the region.

Figure 6a shows the diurnal variation of the measured surface temperature (solid) and the longwave downwelling irradiance (dashed) during the polar night time-period measured during the years of 2017-2022. A striking inter-timestep variability is present between the two variables, with a Pearson correlation of 0.87. This indicates that during the polar night, the largest influence on the diurnal variation of surface temperature in Barrow is the longwave downwelling irradiance emitted from the persistent clouds as well as ambient air. Without the influence of any incoming solar shortwave radiation, there is still a 0.5° C diurnal variability in surface air temperature. As noted in *Harrison & Ambaum*, 2013 as well as supported by Figure 1, the formation of the CBH is directly related to the intensity of fair-weather Ez. This supports the finding that the diurnal variability of surface temperature in Barrow during the polar night could

be driven by the intensity of the GEC. This connects the summation of all global thunderstorm and electrified clouds to the temperature variability in the polar night Arctic.

Figure 6b shows that during the non-polar night time period in Barrow, AK, the surface temperature (solid) is no longer in phase with the longwave downwelling irradiance measured at the surface (dashed). This diurnal phase is also inconsistent with the well-known diurnal GEC such as in the case of the figure 6a. This mismatch indicates that the surface temperature during the non-polar night time periods is not driven by GEC, and rather the obvious incoming radiation from the sun. This drastic diurnal phase change in the surface temperature and longwave downwelling irradiance indicates a clear regime change in the drivers of diurnal temperature variability in the polar-night Arctic. With the diurnal variability of CBH, CTH, cloud thickness, as well as other precipitation properties at the NSA site supporting the findings of *Harrison & Ambaum*, [2013], the GEC theory influencing persistent stratified clouds in the Arctic polar-night deserves more attention as a potential leading candidate for this observed diurnal variability of cloud and precipitation properties during the Arctic polar-night.

4.4 Summary and Discussion:

In the laboratory-like setting during the 66-days of polar night in Barrow, Alaska, the influence of the sun's emitted shortwave radiation on the diurnal cycle of clouds, precipitation, aerosols, and surface temperature is considered minimal-to-none [*Lüpkes et al.*, 2008]. This offers the opportunity to observe smaller magnitude effects that may influence the diurnal variability of these parameters globally, which may go undetected and unrepresented in the understanding of the climate system. Observations during the 5-years of collected E_z, cloud, precipitation, and aerosol data at the NSA site during the polar night, show that the CBH, CTH, cloud thickness, number of precipitating particles, total column backscatter, and surface

temperature are modulated on timescales consistent with the diurnal variation exhibited in the GEC system.

Figure 7 summarizes the correlation matrix between all explored polar night cloud and precipitation variables; cloud thickness, (c. thickness) longwave downwelling (DLWI), fairweather E_z , CBH, sum column backscatter (sum backscatter), number of precipitation particles (particles (#)), precipitation intensity (precip intensity), temperature, and visibility. Warm colors indicate positive linear correlations between the variables, and cool colors indicate negative linear correlations of the hourly averaged diurnal timeseries. The largest positive correlations (r-values >0.75) occur between the surface temperature and longwave downwelling irradiance, as well as the precipitation intensity and the surface reflectivity. Other statistically significant positive correlations (r-value > 0.5 & r-value < 0.75), occur between the sum of the column backscatter and the fair-weather E_z , CBH and the fair-weather E_z , and sum of the column properties show smaller, but still statistically significant (r-value >0.25 & r-value < 0.5) are present between the fair-weather E_z and the cloud thickness, number of precipitating particles, and the visibility.

Figure 7 shows the most negatively correlated parameters (r-values < -0.5) between the fair-weather E_z and the surface temperature, fair-weather E_z and longwave downwelling, and the longwave downwelling and CBH.

Figure 8 summarizes these results in a schematic diagram. Figure 8a and Figure 8b display the mean 5 UTC polar night and 17 UTC scenarios respectively in Barrow, Alaska. Results from this study, building off the works of *Harrison & Ambaum* [2013] among several others, shows that during time periods in the polar night with larger magnitude electric fair-

weather electric fields (GEC return current), the persistent layered clouds in Barrow Alaska tend to have higher CBHs, CTHs, tend to be thicker, precipitate with more numerous particles, have less longwave downwelling irradiance, leading to slightly cooler surface temperatures (approximately 0.5° C colder). The opposite effect on these properties occurs for time periods of relatively small magnitude fair-weather E_z . Figure 8 shows that during 17 UTC, the mean surface E_z is 16.6 V/m greater than the mean E_z at 5 UTC. This also corresponds to mean CBHs that form approximately 230 m higher in the column as well as grow 240 m thicker during the average 17 UTC condition when compared to the average 5 UTC time-period. Precipitation events tend to precipitate approximately 5 particles/second more during 17 UTC in comparison to 5 UTC events. The persistent layered clouds that form closer to the ground during 5 UTC emit 1.62 W/m² more longwave downwelling irradiance, than 17 UTC conditions, leading to a slightly warmer surface temperature (0.4°C) than during average 17 UTC temperatures.

These results indicate that in the lack of incoming solar shortwave radiance during the polar night, these cloud parameters modulate on the GEC diurnal timescale. This leads to the speculation that the totality of thunderstorms and electrified clouds transpiring around the globe, directly influence the diurnal cloud and precipitation properties as well as surface temperature in the high latitude regions of the globe during the polar night. The electrical effect on cloud formation and precipitation modulation remains a large uncertainty in climate models. This GEC effect needs to be included, especially in the polar regions, to model the climate system more accurately.

Major finding from this study include:

• A statistically significant relationship is found between the CBH formation in Barrow, Alaska (>71°N), and the magnitude of the fair-weather E_z (r-value = 0.61)

- during the polar night time periods. This result corroborates the findings in Finland and Antarctica, displaying a similar relationship on the GEC diurnal timescale.
- During the polar night, the fair-weather E_z is also found to be statistically correlated to the CTH, cloud thickness, sum of the column backscatter, the number of precipitation particles at the surface, the longwave downwelling irradiance, and the surface temperature. During periods of larger magnitude fair-weather E_z (more global thunderstorms and electrified clouds), the clouds tend to be taller, thicker, have a larger total column backscattering, and have more numerous precipitating particles at the surface.
- A significant linear relationship is present between the fair-weather E_z and the longwave downwelling irradiance from the persistent clouds in Barrow (r-value = -0.70). An even more correlated relationship between the diurnal longwave downwelling irradiance and the surface temperature (r-value = 0.87) is found in the region. This implies that as the CBHs occur higher in the vertical column during larger magnitude fair-weather E_z time periods, there tends to be less longwave downwelling from the clouds, which leads to colder surface temperatures. This provides evidence that the diurnal surface temperature variability observed during the polar night could be indirectly related to the magnitude of the GEC current driven by global thunderstorms and electrified clouds.

Thirty-to-forty percent of the globe is covered by persistent stratocumulus clouds with liquid particles, a slightly different from to those in ice phase explored in this study [Nicoll & Harrison, 2016]. Although the GEC effect on these clouds in the tropics and subtropics, which never experience the polar night may be much smaller than the effect of the diurnal solar

incoming radiance, it may not be negligible on the cloud physics and precipitation properties of these clouds. Future work is needed to better understand the how the presence of the GEC return current, occurring continually all over the globe, influences the properties of global clouds. This could indeed provide an important piece of the climate system, that is not very well understood presently.

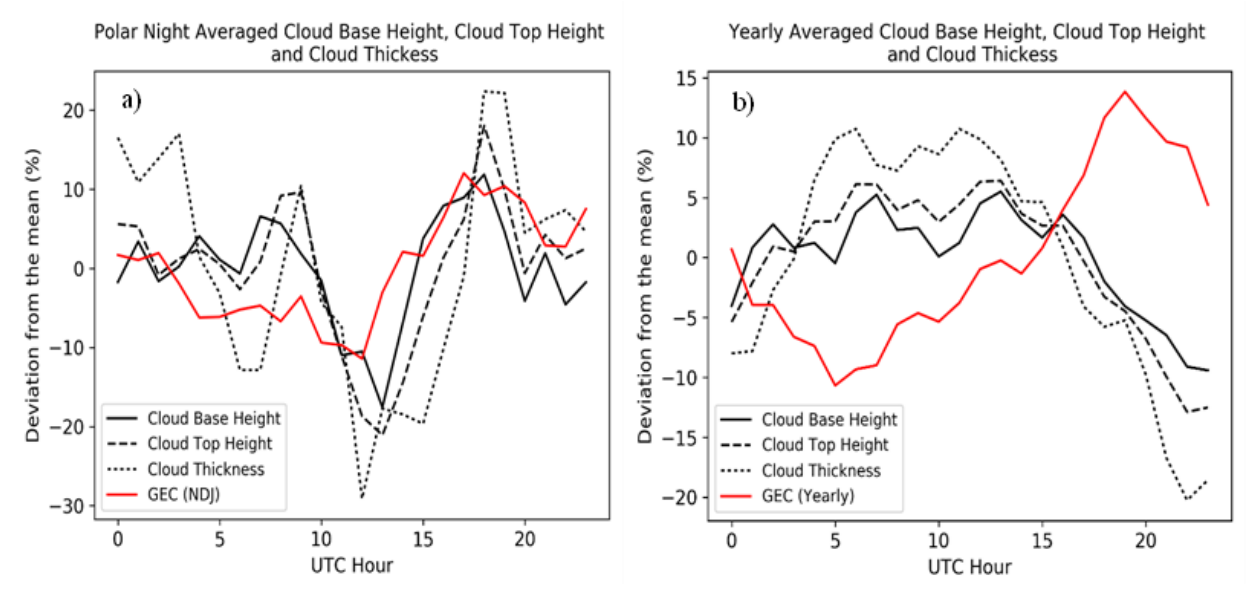


Figure 4.1: Diurnal variations of the a) polar-night and b) yearly averaged fair weather electric field (red), cloud-base height (solid), cloud top height (dashed), and cloud thickness (dotted) measured with the Micro-Pulse Lidar (MPL) in Barrow AK during the years of 2017-2022.

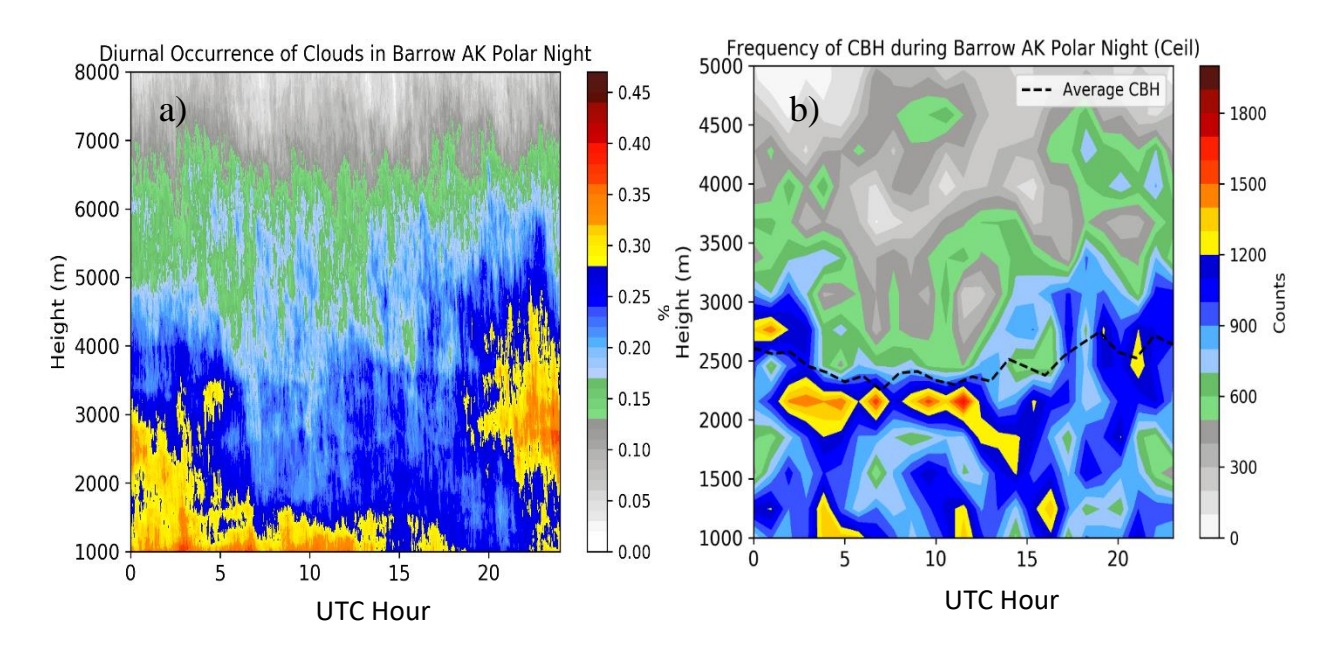


Figure 4.2: a) Two-Dimensional histogram of polar night cloud occurrence (%) in Barrow, Alaska measured by the Ka-Band Zenith Radar (KAZR). A threshold of -30 dBZ was used to determine the presence/absence of a cloud. B) Two-Dimensional histogram of polar night cloud counts in Barrow, Alaska measured by the ceilometer. The dashed black line is the mean cloud base height during the same time-period binned to 1-hour averages.

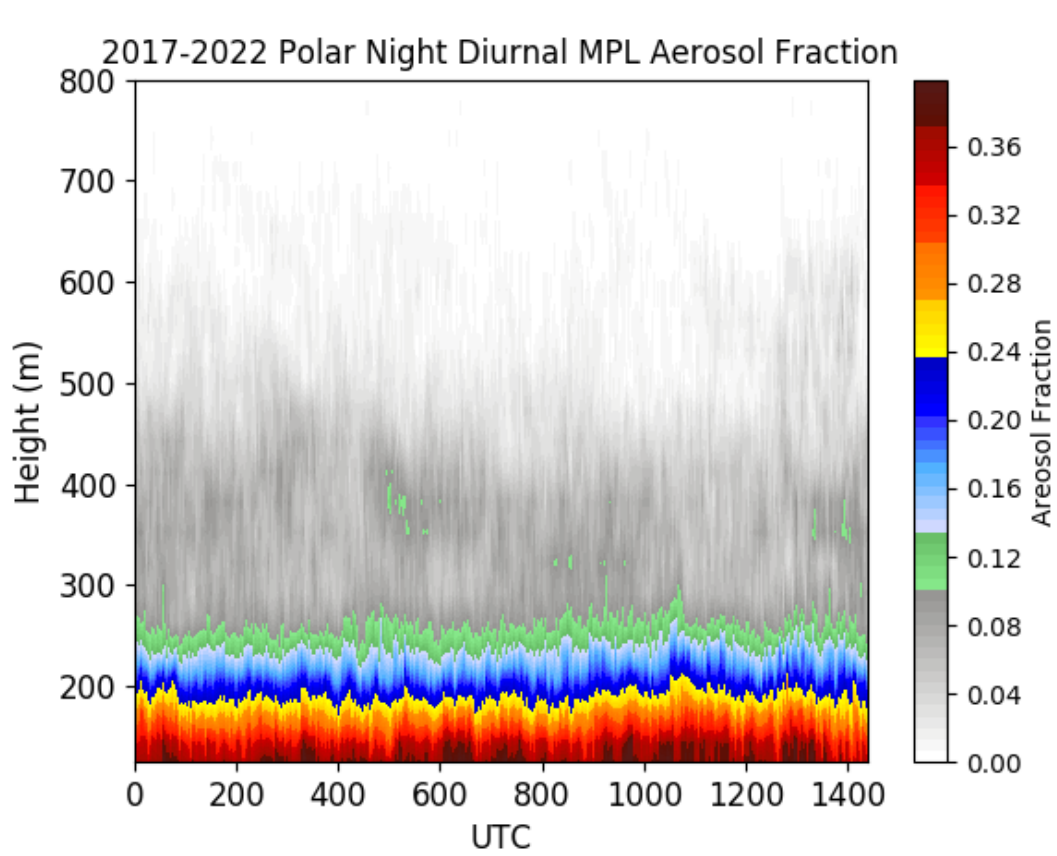


Figure 4.3: Two-Dimensional histogram of polar night aerosol occurrence (%) in Barrow, Alaska measured by the Micro Pulse Lidar (MPL). A threshold of 100 km-¹*sr-¹ was used to determine the presence/absence of an aerosol event.

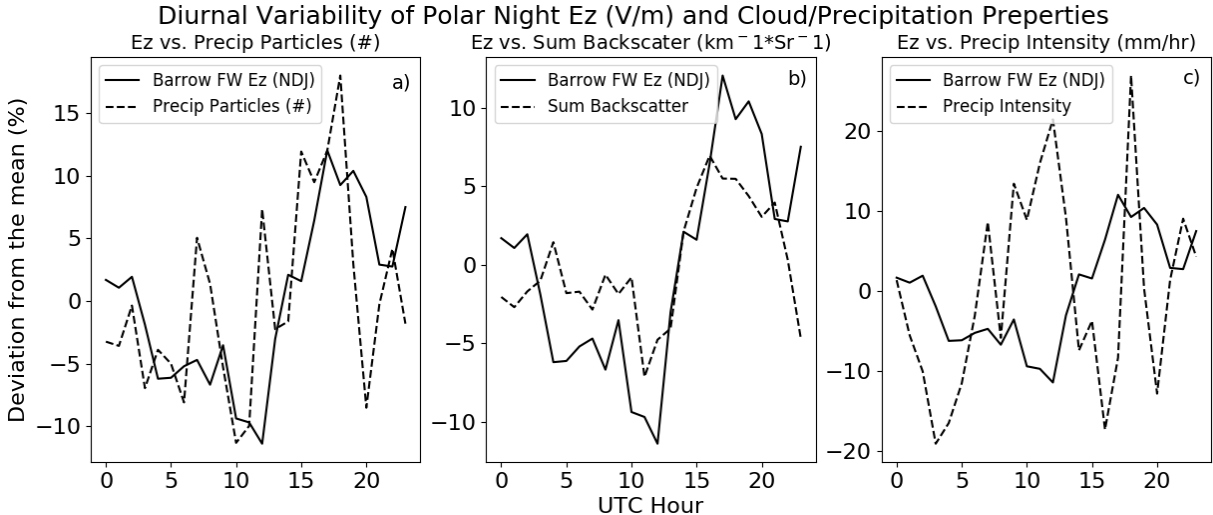


Figure 4.4: a) Diurnal variation of the polar-night averaged fair weather electric field (solid), and polar night cloud precipitation particle counts (dashed) measured with the impact distrometer. b) Diurnal variability of the polar-night averaged fair weather electric field (solid), and polar night cloud sum of vertical column backscatter (dashed) measured with the micro-pulse Lidar. c) Diurnal variability of the polar-night averaged fair weather electric field (solid), and polar night cloud precipitation intensity (dashed) measured with the impact distrometer. All values are normalized as a percent deviation from the mean value during polar night in Barrow AK for the years of 2017-2021.

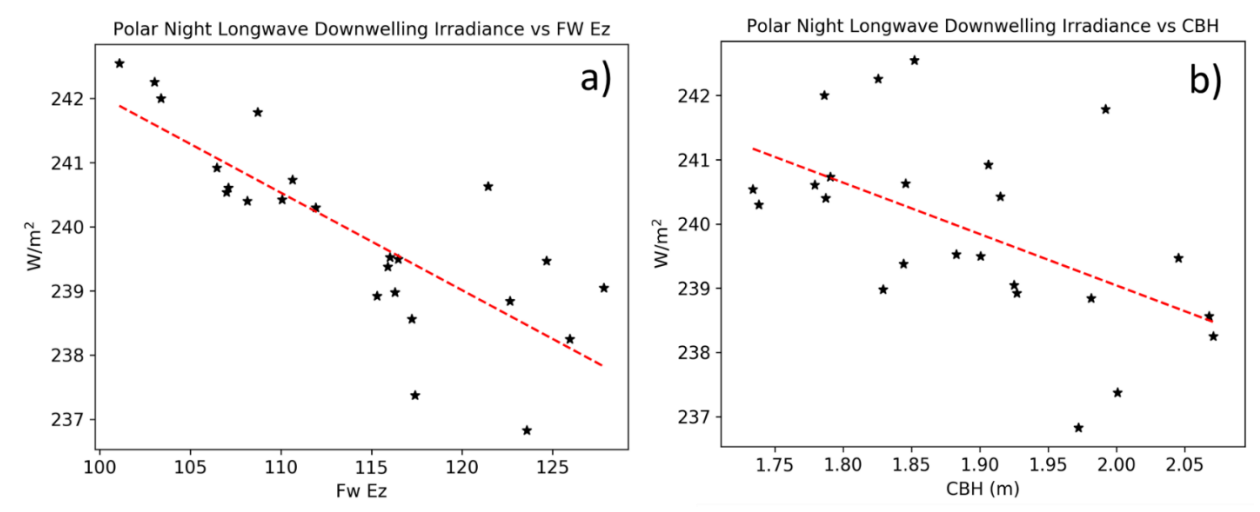


Figure 4.5: a) Scatter plot of hourly average of the polar night fair weather electric field (V/m), verses downwelling longwave irradiance (W/m²). b) Scatter plot of hourly average of the Cloud Base Height (km), verses downwelling longwave irradiance (W/m²). Measurements were made in Barrow AK during the polar night in 2017-2022.

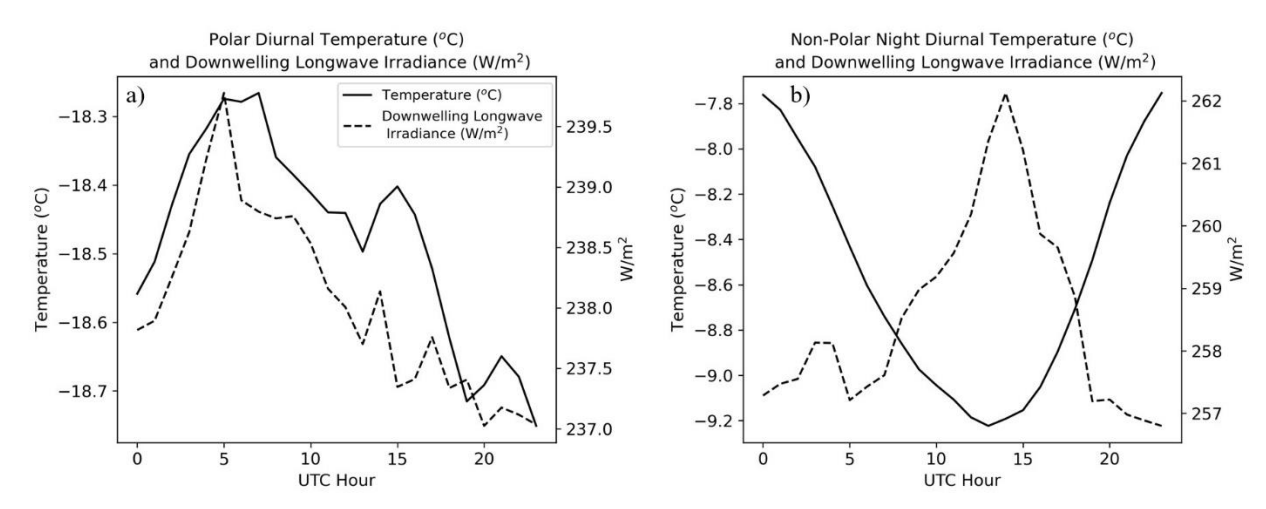


Figure 4.6: Diurnal variation of the polar night (a) and non-polar night (b) surface air temperature (solid) and downwelling longwave irradiance (dashed) measured by the SKYRAD during the years of 2017-2022.

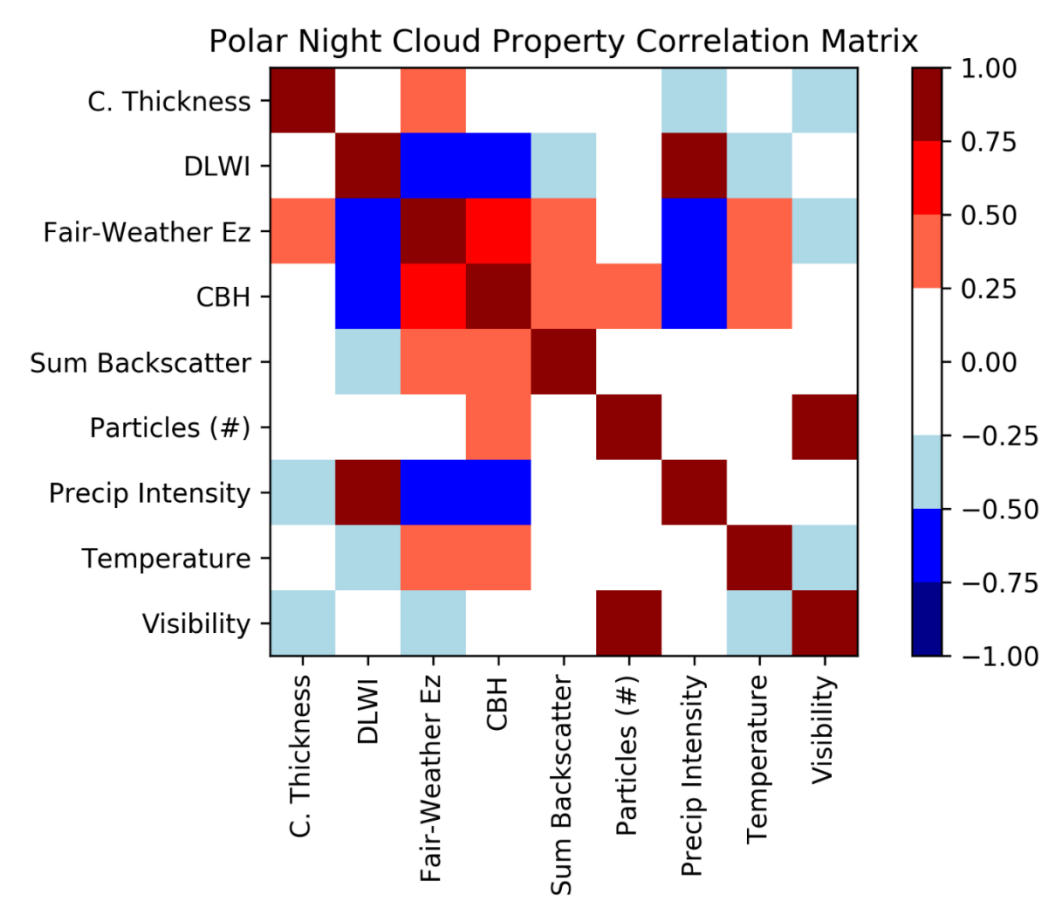


Figure 4.7: Correlation matrix of the diurnal variability of 9-explored polar night properties: cloud thickness (c. thickness), downwelling longwave irradiance (DLWI), fair-weather E_z , cloud base height (CBH), sum of vertical backscatter (sum backscatter), number of precipitation particles (#), precipitation intensity, temperature, and visibility.

Two Scenarios of the Vertical Electric field, Cloud Properties and Surface Temperature during the Polar Night

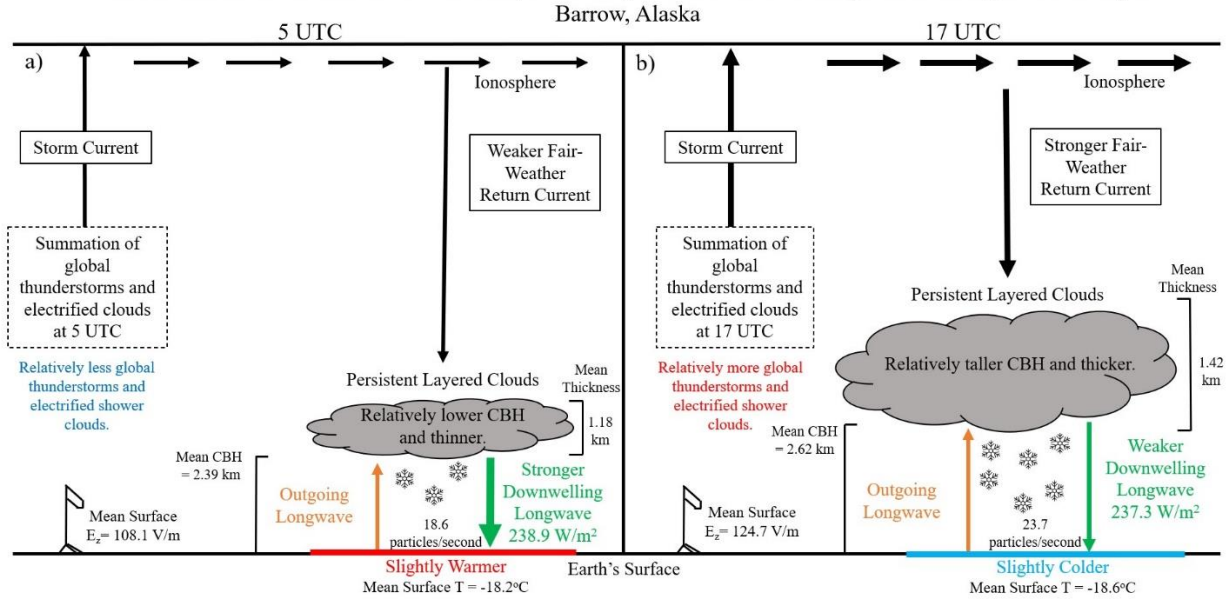


Figure 4.8: Summary schematic of the influence of the GEC on diurnal properties of persistent layered clouds and diurnal variation of surface temperature during the polar night.

CHAPTER V: SUMMARY AND FUTURE WORK

A longstanding important question in the scientific community is how thunderstorms and electrified clouds across the globe have responded to the changing climate in past decades, and what should we expect in the future. Before the advent of satellite-based optical imagers in space in the late 20th century, only crude ground station point-measurements over populated land regions were possible, with measurements such as the thunder-day; a binary occurrence of auditory thunder detected at the station during a 24-hour period by a human observer. While this provided a relatively long-term and stable time series of quasi-global number of thunderstorm days observed at these stations, it was unclear how this variable related to the number of observed lightning flashes, as well as number of individual thunderstorms that are observed at the sites.

The inclusion of the Lightning Imaging Sensor (LIS) onboard the Tropical Rainfall Measuring Mission (TRMM) satellite which operated from 1998-2013, allows for a 16-year overlap of the thunder-day and optical flash data and thunderstorm precipitation features (TPFs) derived from the Ku-band radar also onboard TRMM. Results show a positive linear correlation between the changes of thunder day occurrence and flash density over most regions of the TRMM domain during the 16-year overlap, including the Maritime Continent, China, and Argentina, with all three regions observing a Pearson correlation of greater than 0.8. The relationship between the thunder-day occurrence and number of TPFs show an even more highly correlated global relationship. However, several regions such as West Africa, Central Africa, and India, show poor or even negative relationships between thunder-day occurrence and the flash density. The disagreements are shown to be related to the changes in the number of flashes per thunderstorm, with all explored poorly correlated regions observing a negative correlation

between the thunder-day occurrence and the flash rate per TPF. This emphasizes the regional nature of the thunder-day variable, with no global consensus present between thunder day occurrence and flash density.

A method for determining robust fair-weather time periods of the Global Electric Circuit (GEC) is developed at the Department of Energy (DOE) Atmospheric Radiation Measurement (ARM) facility in the North Slope of Alaska (NSA). The surface vertical electric field is compared to the vertically pointing Micro Pulse Lidar (MPL) backscatter. Results show that during 5-minute averaged time periods of very low MPL reflectance (<100km⁻¹*sr⁻¹), a clear separation of very stable electric fields within the typical fair-weather range is present. The samples satisfying these criteria are found with a 5-minute averaged standard deviation of less than 15 V/m, and surface electric field between -250 V/m to -50 V/m. This leads to a simple definition of the fair weather condition utilizing only the electric field measurements, with no supplemental instrumentation needed. This allows for a direct comparison between multiple electric field measurements at different ground locations utilizing the same fair-weather definition.

Fair-weather time periods meeting the above criteria are analyzed using the same variety of Campbell Scientific (CS110) electric field meters, calibrated consistently in Barrow, Alaska and Corpus Christi, Texas. The two instruments separated by more than 6,000 km show very consistent composite yearly and monthly-averaged diurnal variation in the fair-weather electric field as well as consistent simultaneous minute-to-hourly variation between the two sites observed in several case studies.

Lastly, implications of the impacts from the fair-weather return current on local cloud and precipitation properties are summarized in Barrow, Alaska during the polar night time period.

Results show that during periods of larger magnitude fair-weather electric fields in the polar night, persistent layered cloud-bases tend to be higher in the column, cloud tops are higher, the clouds are thicker, have a larger total column backscatter, and precipitate more numerous particles at the surface. The diurnal variations of fair-weather electric field as well as the cloud base height are found to be statistically negatively correlated to the longwave downwelling irradiance from the clouds and ambient air during the polar night. Lower cloud bases and lower magnitude fair-weather electric fields are found to be associated with larger longwave downwelling irradiance. Furthermore, the diurnal surface temperature is found to be very highly correlated (r = 0.87) to the longwave downwelling irradiance indicating that the slight diurnal surface temperature variation during the polar night is primarily driven by the infrared downwelling from the persistent layered clouds. This leads to the fascinating notion, that the total summation of global thunderstorms and electrified clouds can potentially influence the properties of polar night clouds, which in turn modulate the surface temperature in the Arctic.

Thirty-to-forty percent of the globe is covered by persistent stratocumulus clouds, similar to those explored in this study, except in liquid form instead of mixed phased form. Although the GEC effect on these clouds in the tropics and subtropics, which never experience the polar night may be much smaller than the effect of the diurnal solar incoming radiance, it may not be negligible on the cloud physics and precipitation properties of these clouds.

Future work in this direction includes analyzing the roll of extratropical synoptic systems in the GEC system. In the past, the GEC "battery" theory was developed utilizing data mainly in the TRMM domain of 35°N-35°S. With the inclusion of vertical storm current measurements over extratropical clouds in the ongoing Investigation of Microphysics and Precipitation for

Atlantic Coast-Threatening Snowstorms (IMPACTS) field campaign, a better understanding of the contribution to the GEC system comes from these types of systems may be possible.

As the Arctic continues to warm at a rate faster than the rest of the globe, it is becoming increasingly important to monitor the effect of the warming on the electrification of precipitation events in the region. As a precursor to thunderstorm activity, significantly electrified clouds that do not produce lightning, known as Electrified Shower Clouds (ESCs), are more prevalent than thunderstorms in the Arctic. A future research direction is to analyze the occurrence as well as cloud and environmental properties of ESCs that occur in Barrow, Alaska.

The auroral influence on the local vertical electric field deserves further exploration. A future research direction is to find statistical relationships between the Active Magnetosphere and Planetary Electrodynamics Response Experiment (AMPERE) auroral data and perturbations in the local electric field in Barrow, AK. With the presence of a Ka-band Zenith Radar (KAZR) and Micro Pulse Lidar (MPL), the unique site allows for the ability to isolate time periods with no cloud, aerosol and blowing snow conditions. This could help to isolate the effects of the geomagnetic influence and potentially help to quantify their effects in the region.

REFERENCES

- Adhikari, A., Liu, C., & Kulie, M. S. (2018). Global Distribution of Snow Precipitation Features and Their Properties from 3 Years of GPM Observations. *Journal of Climate*, 31(10), 3731-3754.
- Adlerman, E. J., & Williams, E. R. (1996). Seasonal variation of the global electrical circuit, *Journal of Geophysical Research: Atmospheres*. 101(D23), 29679-29688.
- Adzhiev, A. K., & Adzhieva, A. A. (2009). Spatial and temporal variations of thunderstorm activity in the Northern Caucasus. *Russian Meteorology and Hydrology*, *34*(12), 789-793.
- Aich, V., R. H. Holzworth, S. J. Goodman, Y. Kuleshov, C. Price, and E. R. Williams, 2018: Lightning: A New Essential Climate Variable, Eos, 99
- Albrecht, R. I., S. J. Goodman, W. A. Petersen, D. E. Buechler, E. C. Bruning, R. J. Blakeslee, and H. J. Christian (2011), The 13 years of TRMM Lightning Imaging Sensor: From individual flash characteristics to decadal tendencies, XIV International Conference on Atmospheric Electricity, August 08–12, 2011, Rio de Janeiro, Brazil.
- Albrecht, R. I., Goodman, S. J., Buechler, D. E., Blakeslee, R. J., & Christian, H. J. (2016).

 Where are the lightning hotspots on Earth?. *Bulletin of the American Meteorological Society*, 97(11), 2051-2068.
- Anderson, C. J., C. K. Wikle, Q. Zhou, and J. A. Royle (2007), Population influences on tornado reports in the United States, Wea. Forecasting, 22, 571–579.
- Araghi, A., Adamowski, J., & Jaghargh, M. R. (2016). Detection of trends in days with thunderstorms in Iran over the past five decades. *Atmospheric Research*, *172*, 174-185.

- G. Baumgaertner, A. J., Thayer, J. P., Neely III, R. R., & Lucas, G. (2013). Toward a comprehensive global electric circuit model: Atmospheric conductivity and its variability in CESM1 (WACCM) model simulations. *Journal of Geophysical Research:* Atmospheres, 118(16), 9221-9232.
- Baumgaertner, A. J. G., Lucas, G. M., Thayer, J. P., & Mallios, S. A. (2014). On the role of clouds in the fair weather part of the global electric circuit. *Atmospheric Chemistry & Physics*, *14*(16).
- Blakeslee, R. J., Christian, H. J., Stewart, M. F., Mach, D. M., Bateman, M., Walker, T. D., ... & Colley, E. C. (2014a). Lightning Imaging Sensor (LIS) for the International Space Station (ISS): mission description and science goals.
- Blakeslee, R. J., Mach, D. M., Bateman, M. G., & Bailey, J. C. (2014b). Seasonal variations in the lightning diurnal cycle and implications for the global electric circuit. *Atmospheric research*, *135*, 228-243.
- Brooks, C.E.P., The distribution of thunderstorms over the globe, Geophys. Mem. London, 24, 147-164, 1925.
- Brooks, H. E., J. W. Lee, and J. P. Craven (2003), The spatial distribution of severe thunderstorm and tornado environments from global reanalysis data, *Atmos. Res.*, **67–68**, 73–94.
- Burns, G. B., Frank-Kamenetsky, A. V., Troshichev, O. A., Bering, E. A., & Reddell, B. D. (2005). Interannual consistency of bi-monthly differences in diurnal variations of the ground-level, vertical electric field. *Journal of Geophysical Research:**Atmospheres, 110(D10).

- Burns, G. B., Tinsley, B. A., Frank-Kamenetsky, A. V., & Bering, E. A. (2007). Interplanetary magnetic field and atmospheric electric circuit influences on ground-level pressure at Vostok. *Journal of Geophysical Research: Atmospheres*, 112(D4).
- Burns, G. B., Tinsley, B. A., Frank-Kamenetsky, A. V., Troshichev, O. A., French, W. J. R., & Klekociuk, A. R. (2012). Monthly diurnal global atmospheric circuit estimates derived from Vostok electric field measurements adjusted for local meteorological and solar wind influences. *Journal of the atmospheric sciences*, 69(6), 2061-2082.
- Cecil, D. J., Goodman, S. J., Boccippio, D. J., Zipser, E. J., & Nesbitt, S. W. (2005). Three years of TRMM precipitation features. Part I: Radar, radiometric, and lightning characteristics. *Monthly Weather Review*, 133(3), 543-566.
- Cecil, D. J., Buechler, D. E., & Blakeslee, R. J. (2014). Gridded lightning climatology from TRMM-LIS and OTD: Dataset description. *Atmospheric Research*, *135*, 404-414.
- Cecil, D. J., Buechler, D. E., & Blakeslee, R. J. (2015). TRMM LIS climatology of thunderstorm occurrence and conditional lightning flash rates. *Journal of Climate*, 28(16), 6536-6547.
- Changnon Jr., S. A., and C. F. Hsu (1984), *Temporal distributions of global thunder days, Final Report NSF ATM-81-14724*, Illinois State Water Survey Champaign, Illinois, 79p.
- Changnon, S. A. (1985). Secular variations in thunder-day frequencies in the twentieth century. *Journal of Geophysical Research: Atmospheres*, 90(D4), 6181-6194.
- Changnon, S. A., & Changnon, D. (2001a). Long-term fluctuations in thunderstorm activity in the United States. *Climatic Change*, *50*(4), 489-503.
- Changnon, S. A. (2001b). Assessment of the quality of thunderstorm data at first-order stations. *Journal of applied meteorology*, 40(4), 783-794.

- Chen, S. M., Y. Du, and L. M. Fan (2004), Lightning data observed with lightning location system in Guang-dong province, China, *IEEE Trans. Power Delivery*, **19**(3), 1148–1153.
- Chmielewski, V. C. (2013). Variations of the vertical electric field and wind speed on days with airborne dust in Lubbock, Texas (Doctoral dissertation).
- Christian, H. J., et al. (1999), The Lightning Imaging Sensor, in *Proceedings of the 11th International Conference on Atmospheric Electricity Held in Guntersville, Alabama, June 7–11, 1999*, NASA Conf. Publ., **209261**, 746–749.
- Christian, H. J., et al. (2003), Global frequency and distribution of lightning as observed from space by the Optical Transient Detector, *J. Geophys. Res.*, **108**(D1), 4005, doi:10.1029/2002JD002347.
- Chronis, T. G., S. J. Goodman, D. Cecil, D. Buechler, F. J. Robertson, J. Pittman, and R. J. Blakeslee (2008), Global lightning activity from the ENSO perspective, *Geophys. Res. Lett.*, **35**, L19804, doi:10.1029/2008GL034321.
- Corney, R. C., G. B. Burns, K. Michael, A. V. Frank-Kamenetsky, O. A. Troshichev, E. A. Bering, V. O. Papitashvili, A. M. Breed, and M. L. Duldig (2003), The influence of polar-cap convection on the geoelectric field at Vostok, Antarctica, J. Atmos. Sol. Terr. Phys., 65(3), 345-354, doi:10.1016/S1364-6826(02)00225-0
- Enno, S.E., Post P., Briede A., Stankunaite I. (2014) Long-term changes in the frequency of thunder days in the Baltic countries. *Boreal Environ. Res.*, 19 (2014), pp. 452-466
- Fleagle, R. G., 1949: The audibility of thunder. J. Acoust. Soc. Amer., 21, 411.
- Goodman, S. J., and D. R. MacGorman. Cloud-to-ground lightning activity in mesoscale convective complexes, Mon. Wea. Rev., **114**, 2320-2328, 1986.

- Goodman, S., D. Buechler, K. Knupp, K. Driscoll, and E. McCaul (2000), The 1997–98 El Nino event and related wintertime lightning variations in the southeastern United States, *Geophys. Res. Lett.*, **27**(4), 541–544, doi:10.1029/1999GL010808.
- Goodman, S. J., et al. (2013), The GOES-R Geostationary Lightning Mapper (GLM), *Atmos. Res.*, **124–125**, 34–49.
- Gorbatenko, V., and A. A. Dulzon (2001), Variations of thunderstorm, Biology and Ecology, Korus.
- Gordon, M., & Taylor, P. A. (2009). The electric field during blowing snow events. *Boundary-layer meteorology*, 130(1), 97-115.
- Grazulis, T. P. (1983). Significant tornadoes 1680-1991, Environmental Films, 1326 pp., and Robert-F. Abbey, Jr, 103, 124-127
- Hamid, E. Y., Kawasaki, Z. I., & Mardiana, R. (2001). Impact of the 1997–98 El Niño event on lightning activity over Indonesia. *Geophysical research letters*, 28(1), 147-150.
- Harrison, R. G. (2004). Long-range correlations in measurements of the global atmospheric electric circuit. Journal of atmospheric and solar-terrestrial physics, 66(13-14), 1127-1133.
- Harrison, R. G. (2013). The carnegie curve. Surveys in Geophysics, 34(2), 209-232.
- Harrison, R. G., & Ambaum, M. H. (2008). Enhancement of cloud formation by droplet charging. Proceedings of the Royal Society A: Mathematical, Physical and Engineering Sciences, 464(2098), 2561-2573.
- Harrison, R. G., Joshi, M., & Pascoe, K. (2011). Inferring convective responses to El Niño with atmospheric electricity measurements at Shetland. Environmental Research Letters, 6(4), 044028.

- Harrison, R. G., & Ambaum, M. H. (2013). Electrical signature in polar night cloud base variations. Environmental Research Letters, 8(1), 015027.
- Harrison, R. G., Nicoll, K. A., & Ambaum, M. H. P. (2015). On the microphysical effects of observed cloud edge charging. Quarterly Journal of the Royal Meteorological Society, 141(692), 2690-2699.
- Khain A, Arkhipov V, Pinsky M, Feldman Y, Ryabov Y. 2004. Rain enhancement and fog elimination by seeding with charged droplets. Part I: Theory and numerical simulations.
 J. Appl. Meteorol.43: 1513 1529.
- Kitagawa, N. (1989). Long-term variations in thunder-day frequencies in Japan. *Journal of Geophysical Research: Atmospheres*, 94(D11), 13183-13189.
- Kunz, M., J. Sander, and C. Kottmeier (2009), Recent trends of thunderstorm and hailstorm frequency and their relation to atmospheric characteristics in southwest Germany, *Int. J. Climatol.*, **29**, 2283–2297.
- Lavigne, T., Liu, C., Deierling, W., & Mach, D. (2017). Relationship between the global electric circuit and electrified cloud parameters at diurnal, seasonal, and interannual timescales. *Journal of Geophysical Research: Atmospheres*, 122(16), 8525-8542.
- Lavigne, T., Liu, C., & Liu, N. (2019). How Does the Trend in Thunder Days Relate to the Variation of Lightning Flash Density?. *Journal of Geophysical Research:*Atmospheres, 124(9), 4955-4974.
- Lavigne, T., Liu, C., Hill, J., & Bruning, E. (2021). Observations from the one year electric field Study-North Slope of Alaska (OYES-NSA) field campaign, and their implications for observing the distribution of global electrified cloud activity. Journal of Atmospheric and Solar-Terrestrial Physics, 214, 105528.

- Lin-Lin, Z., Jian-Hua, S., & Jie, W. (2010). Thunder events in China: 1980-2008. *Atmospheric and Oceanic Science Letters*, 3(4), 181-188.
- Liu, C., & Zipser, E. J. (2008). Diurnal cycles of precipitation, clouds, and lightning in the tropics from 9 years of TRMM observations. *Geophysical Research Letters*, 35(4).
- Liu, C., Williams, E. R., Zipser, E. J., & Burns, G. (2010). Diurnal variations of global thunderstorms and electrified shower clouds and their contribution to the global electrical circuit. *Journal of the atmospheric sciences*, 67(2), 309-323.
- Liu, C., Cecil, D. J., Zipser, E. J., Kronfeld, K., & Robertson, R. (2012). Relationships between lightning flash rates and radar reflectivity vertical structures in thunderstorms over the tropics and subtropics. *Journal of Geophysical Research: Atmospheres*, 117(D6).
- Liu, C., & Zipser, E. J. (2015). The global distribution of largest, deepest, and most intense precipitation systems. *Geophysical Research Letters*, 42(9), 3591-3595.
- Liu, N., & Liu, C. (2016). Global distribution of deep convection reaching tropopause in 1 year GPM observations. *Journal of Geophysical Research: Atmospheres*, 121(8), 3824-3842.
- Mackerras, D., M. Darveniza, R. E. Orville, E. R. Williams, and S. J. Goodman (1998), Global lightning: Total, cloud and ground flash estimates, *J. Geophys. Res.*, **103**(D16), 19,791–19,809, doi:10.1029/98JD01461.
- Lucas, G. M., Baumgaertner, A. J. G., & Thayer, J. P. (2015). A global electric circuit model within a community climate model. *Journal of Geophysical Research:*Atmospheres, 120(23), 12-054.
- Lucas, G. M. (2017). Investigating the physical mechanisms that impact electric fields in the atmosphere.

- Lucas, G. M., Thayer, J. P., & Deierling, W. (2017). Statistical analysis of spatial and temporal variations in atmospheric electric fields from a regional array of field mills. Journal of Geophysical Research: Atmospheres, 122(2), 1158-1174.
- Lüpkes, C., Vihma, T., Birnbaum, G., & Wacker, U. (2008). Influence of leads in sea ice on the temperature of the atmospheric boundary layer during polar night. Geophysical Research Letters, 35(3).
- MacGorman, D. R., MacGorman, R., Rust, W. D., & Rust, W. D. (1998). *The electrical nature of storms*. Oxford University Press on Demand.
- Mach, D. M., R. J. Blakeslee, M. G. Bateman, and J. C. Bailey, (2009). Electric fields, conductivity, and estimated currents from aircraft overflights of electrified clouds. *J. Geophys. Res.*, **114**, D10204, https://doi.org/10.1029/2008JD011495.
- Mach, D. M., Blakeslee, R. J., Bateman, M. G., & Bailey, J. C. (2010). Comparisons of total currents based on storm location, polarity, and flash rates derived from high-altitude aircraft overflights. *Journal of Geophysical Research: Atmospheres*, 115(D3).
- Mach, D. M., Blakeslee, R. J., & Bateman, M. G. (2011). Global electric circuit implications of combined aircraft storm electric current measurements and satellite-based diurnal lightning statistics. *Journal of Geophysical Research: Atmospheres*, 116(D5).
- Markson, R. (1986). Tropical convection, ionospheric potentials and global circuit variation. Nature, 320(6063), 588-594.
- Markson, R. (2007). The global circuit intensity: Its measurement and variation over the last 50 years. Bulletin of the American Meteorological Society, 88(2), 223-242.

- Marshall, T. C., Rust, W. D., Stolzenburg, M., Roeder, W. P., & Krehbiel, P. R. (1999). A study of enhanced fair-weather electric fields occurring soon after sunrise. Journal of Geophysical Research: Atmospheres, 104(D20), 24455-24469.
- Merenti-Välimäki, H. L., Lönnqvist, J., & Laininen, P. (2001). Present weather: comparing human observations and one type of automated sensor. *Meteorological Applications*, **8**(4), 491-496.
- Negri, A.J., T.L. Bell, and L. Xu, (2002). Sampling of the Diurnal Cycle of Precipitation Using TRMM. *J. Atmos. Oceanic Technol.*, **19**, 1333–1344.
- Ni, X., Zhang, Q., Liu, C., Li, X., Zou, T., Lin, J., ... & Ren, Z. (2017). Decreased hail size in China since 1980. *Scientific reports*, 7(1), 10913.
- Nicoll, K. A., & Harrison, R. G. (2016). Stratiform cloud electrification: comparison of theory with multiple in-cloud measurements. Quarterly Journal of the Royal Meteorological Society, 142(700), 2679-2691.
- Nicoll, K. A., Harrison, R. G., Barta, V., Bor, J., Brugge, R., Chillingarian, A., ... & Kubicki, M. (2019). A global atmospheric electricity monitoring network for climate and geophysical research. Journal of Atmospheric and Solar-Terrestrial Physics, 184, 18-29.
- Olson, D. E. (1971). The evidence for auroral effects on atmospheric electricity. *pure and applied geophysics*, 84(1), 118-138.
- Peterson, M., W. Deierling, C. Liu, D. Mach, C. Kalb, 2018: A TRMM/GPM assessment of the composition of Generator Current that supplies the Global Electric Circuit, *J. Geophys. Res.*, **122**, 10,025–10,049, doi:10.1002/2016JD026336.

- Pinto, O., Pinto, I. R. C. A., & Ferro, M. A. S. (2013). A study of the long-term variability of thunderstorm days in southeast Brazil. *Journal of Geophysical Research:*Atmospheres, 118(11), 5231-5246.
- Pinto, O. (2015). Thunderstorm climatology of Brazil: ENSO and Tropical Atlantic connections. *International Journal of Climatology*, **35**(6), 871-878.
- Price, C., & Rind, D. (1994). Possible implications of global climate change on global lightning distributions and frequencies. *Journal of Geophysical Research: Atmospheres*, 99(D5), 10823-10831.
- Price, C. G. (2013), Lightning applications in weather and climate research, *Surv*. *Geophys.*, **34**(6), 755–767, doi:10.1007/s10712-012-9218-7.
- Reddell, B. D., Benbrook, J. R., Bering, E. A., Cleary, E. N., & Few, A. A. (2004). Seasonal variations of atmospheric electricity measured at Amundsen-Scott South Pole Station.

 Journal of Geophysical Research: Space Physics, 109(A9).
- Reeve, N., & Toumi, R. (1999). Lightning activity as an indicator of climate change. *Quarterly Journal of the Royal Meteorological Society*, 125(555), 893-903.
- Roble, R. G. (1986). The global atmospheric-electrical circuit. The Earth's electrical environment, 206-231.
- Rodger, C. J., Werner, S., Brundell, J. B., Lay, E. H., Thomson, N. R., Holzworth, R. H., & Dowden, R. L. (2006). Detection efficiency of the VLF World-Wide Lightning Location Network (WWLLN): initial case study.
- Rudlosky, S. D., S. J. Goodman, K. S. Virts, and E. C. Bruning, 2018: Initial Geostationary Lightning Mapper Observations, *Geophys. Res. Lett.*, DOI:10.1029/2018GL081052.

- Rycroft, M. J., Israelsson, S., & Price, C. (2000). The global atmospheric electric circuit, solar activity and climate change. *Journal of Atmospheric and Solar-Terrestrial Physics*, 62(17-18), 1563-1576.
- Rycroft, M. J., Odzimek, A., Arnold, N. F., Füllekrug, M., Kułak, A., & Neubert, T. (2007). New model simulations of the global atmospheric electric circuit driven by thunderstorms and electrified shower clouds: The roles of lightning and sprites. *Journal of Atmospheric and Solar-Terrestrial Physics*, 69(17-18), 2485-2509.
- Rycroft, M. J., Harrison, R. G., Nicoll, K. A., & Mareev, E. A. (2008). An overview of Earth's global electric circuit and atmospheric conductivity. In *Planetary Atmospheric Electricity* (pp. 83-105). Springer, New York, NY.
- Sátori, G., Williams, E., & Lemperger, I. (2009). Variability of global lightning activity on the ENSO time scale. *Atmospheric Research*, *91*(2-4), 500-507.
- Schaefer, J. T., and J. G. Galway, 1982: Population biases in tornado climatology. Preprints, 12th

 Conf. on Severe Local Storms, San Antonio, TX, *Amer. Meteor. Soc.*, 51–54.
- Schmidt, D. S., Schmidt, R. A., & Dent, J. D. (1999). Electrostatic force in blowing snow.

 Boundary-Layer Meteorology, 93(1), 29-45
- Seto, S., Iguchi, T., & Oki, T. (2013). The basic performance of a precipitation retrieval algorithm for the global precipitation measurement mission's single/dual-frequency radar measurements. *IEEE Transactions on Geoscience and Remote Sensing*, *51*(12), 5239-5251.
- Siingh, D., Gopalakrishnan, V., Singh, R. P., Kamra, A. K., Singh, S., Pant, V., ... & Singh, A. K. (2007). The atmospheric global electric circuit: an overview. Atmospheric Research, 84(2), 91-110.

- Slyunyaev, N. N., Ilin, N. V., Mareev, E. A., & Price, C. G. (2021). The global electric circuit land—ocean response to the El Niño—Southern Oscillation. Atmospheric Research, 260, 105626.
- Sonnadara, U. (2016). Spatial and temporal variations of thunderstorm activities over Sri Lanka. *Theoretical and applied climatology*, 124(3-4), 621-628.
- Stephens, G. L., Vane, D. G., Boain, R. J., Mace, G. G., Sassen, K., Wang, Z., ... & Mitrescu, C. (2002). The CloudSat mission and the A-Train: A new dimension of space-based observations of clouds and precipitation. Bulletin of the American Meteorological Society, 83(12), 1771-1790.
- Tinsley, B. A. (2000). Influence of solar wind on the global electric circuit, and inferred effects on cloud microphysics, temperature, and dynamics in the troposphere. Space Science Reviews, 94(1-2),231-258.
- Toracinta, E. R., Cecil, D. J., Zipser, E. J., & Nesbitt, S. W. (2002). Radar, passive microwave, and lightning characteristics of precipitating systems in the tropics. *Monthly Weather Review*, 130(4), 802-824.
- Tuomi, T. J., and A. Mäkelä (2008), Thunderstorm climate of Finland 1998–2007, Geophysica, 44, 29–42.
- Whipple, F. J. W. (1929). On the association of the diurnal variation of electric potential gradient in fine weather with the distribution of thunderstorms over the globe. Quarterly Journal of the Royal Meteorological Society, 55(229), 1-18.
- Williams, E. R. (1992). The Schumann resonance: A global tropical thermometer. *Science*, *256*(5060), 1184-1187.

- Williams, E. R., & Heckman, S. J. (1993). The local diurnal variation of cloud electrification and the global diurnal variation of negative charge on the Earth. *Journal of Geophysical Research: Atmospheres*, 98(D3), 5221-5234.
- Williams, E. R. (1994). Global circuit response to seasonal variations in global surface air temperature. *Monthly Weather Review*, 122(8), 1917-1929.
- Williams, E.R., Global circuit response to temperature on distinct time scales: A status report, in Atmospheric and Ionospheric Phenomena Associated with Earthquakes, Ed., M. Hayakawa), Terra Scientific Publishing (Tokyo), 1999.
- Williams, E., K. Rothkin, D. Stevenson, and D. Boccippio, Global lightning variations caused by changes in thunderstorm flash rate and by changes in the number of thunderstorms, *J. Appl. Meteorol.*, **39**, 2223–2230, 2000.
- Williams, E., & Stanfill, S. (2002). The physical origin of the land-ocean contrast in lightning activity. Comptes Rendus Physique, 3(10), 1277-1292
- Williams, E. R., & Sátori, G. (2004). Lightning, thermodynamic and hydrological comparison of the two tropical continental chimneys. Journal of Atmospheric and Solar-Terrestrial Physics, 66(13-14), 1213-1231.
- Williams, E. (2005), Lightning and climate: A review, Atmos. Res., 76, 272–287.
- Williams, E. R. (2009). The global electrical circuit: A review. *Atmospheric Research*, 91(2-4), 140-152.
- Williams, E.R., 2012. Franklin Lecture: Lightning and Climate

 (http://fallmeeting.agu.org/2012/events/franklinlecture-ae31a-lightning-and-climate-video-on-demand/.

- Williams, E., & Mareev, E. (2014). Recent progress on the global electrical circuit. Atmospheric Research, 135, 208-227.
- Wilson, C. T. R. (1909). LVI. On thunderstorm electricity. The London, Edinburgh, and Dublin Philosophical Magazine and Journal of Science, 17(100), 634-641.
- Wilson, C. T. R. (1921). III. Investigations on lighting discharges and on the electric field of thunderstorms. Philosophical Transactions of the Royal Society of London. Series A, Containing Papers of a Mathematical or Physical Character, 221(582-593), 73-115.
- Wilson, C. T. R. (1924). The electric field of a thundercloud and some of its effects. Proceedings of the Physical Society of London (1874-1925), 37(1), 32D
- World Meteorological Organization (1953), World distribution of thunderstorm days. Part 1: Tables, WMO Publ. 21, TP 6, Geneva, Switzerland.
- Ye, H., Fetzer, E. J., Wong, S., Lambrigtsen, B. H., Wang, T., Chen, L., & Dang, V. (2017).

 More frequent showers and thunderstorm days under a warming climate: evidence observed over Northern Eurasia from 1966 to 2000. *Climate Dynamics*, 49(5-6), 1933-1944.
- Yoshida, S., T. Morimoto, T. Ushio, and Z. Kawasaki (2007), ENSO and convective activities in Southeast Asia and western Pacific, Geophys. Res. Lett., 34, L21806, doi:10.1029/2007GL030758.
- Zipser, E. J., Cecil, D. J., Liu, C., Nesbitt, S. W., & Yorty, D. P. (2006). Where are the most intense thunderstorms on Earth? *Bulletin of the American Meteorological Society*, 87(8), 1057-1072.
- Zhang, Q., Ni, X., & Zhang, F. (2017). Decreasing trend in severe weather occurrence over China during the past 50 years. *Scientific Reports*, 7, 42310.

ProQuest Number: 29994308

INFORMATION TO ALL USERS

The quality and completeness of this reproduction is dependent on the quality and completeness of the copy made available to ProQuest.



Distributed by ProQuest LLC (2023). Copyright of the Dissertation is held by the Author unless otherwise noted.

This work may be used in accordance with the terms of the Creative Commons license or other rights statement, as indicated in the copyright statement or in the metadata associated with this work. Unless otherwise specified in the copyright statement or the metadata, all rights are reserved by the copyright holder.

This work is protected against unauthorized copying under Title 17, United States Code and other applicable copyright laws.

Microform Edition where available © ProQuest LLC. No reproduction or digitization of the Microform Edition is authorized without permission of ProQuest LLC.

ProQuest LLC 789 East Eisenhower Parkway P.O. Box 1346 Ann Arbor, MI 48106 - 1346 USA